Online Battery Monitoring for State-of-Charge and Power Capability Prediction

by

Larry W. Juang

A thesis submitted in partial fulfillment of
requirements for the degree of

Master of Science
(Electrical Engineering)

at the

University of Wisconsin – Madison

2010

Online Battery Monitoring for State-of-Charge and Power Capability Prediction

by

Larry W. Juang

Under the supervision of Professor Thomas M. Jahns and Robert D. Lorenz

at the University of Wisconsin – Madison

Approved by _____

Thomas M. Jahns

Approved by _____

Robert D. Lorenz

Date _____

Abstract

This document presents an investigation of a proposed methodology that uses system identification techniques to implement a monitoring system for lead-acid batteries in an electric vehicle. Specifically, the information that the proposed methodology provides can help estimate the energy remained in the battery bank (State-of-Charge (SOC)) and the power capability of the battery bank (State-of-Function (SOF)). A combination of analytical and experimental techniques has been devised to construct an equivalent circuit model that includes a diffusion voltage term for the OPTIMA D34M battery used in the WEMPEC Corbin Sparrow vehicle. In addition, the document analyzes a set of actual road trip data from the WEMPEC Corbin Sparrow to demonstrate the proposed model's potential use for diagnosing the relative state-of-health (SOH) of individual batteries. Detailed discussions of the limitations and assumptions associated with the model, as well as other possible alternatives, are included in the document. The performance capabilities of the proposed method for estimating battery SOC and SOF are evaluated against experimental data with an emphasis on electric vehicle (EV) operations.

Acknowledgement

The author would like to gratefully acknowledge the funding and support provided by the Wisconsin Electric Machines and Power Electronics Consortium (WEMPEC) at the University of Wisconsin at Madison. Many knowledgeable individuals have provided their insights and expertises to help make this project possible. Profs. Jahns and Lorenz of WEMPEC and Prof. Setheras of the Electric and Computer Engineering (ECE) Department were generous with their time to provide necessary guidance, both research direction wise and technology wise. The author's labortory partners, Phillip Kollmeyer, Adam Anders, and Adam Shea, have always been patient with the author's shortcomings and eager to share their know-how, especially on the hands-on matters. Micah Erickson, along with many of the author's colleagues in WEMPEC, has offered much valued opnions on the subject. Finally, the author thanks his parents for their unconditional support for his education and everything else in life.

Table of Contents

List of Figures

List of Tables

Nomenclature

Abbreviations and Acronym

AGM	Absorbed Glass Mat
Ah	Amp-Hours
EC	Ethylene Carbon
EV	Electric Vehicle
HEV	Hybrid Electric Vehicle
Li-Ion	Lithium-ion
LPF	Low Pass Filter
NiCd	Nickel-Metal Cadmium
NiMH	Nickel-Metal Hydride
OCV	Open Circuit Voltage
PUCF	Pole Update Correction Factor
SOC	State-of-Charge
SOH	State-of-Health
UPS	Uninterruptible Power Supplies
$\frac{W}{l}$	Watts per Liter
$\frac{Wh}{l}$	Watt-Hours per Liter
$\frac{Wh}{Miles}$	Watt-Hours per Miles

Introduction

Background

As the transportation industry strives to electrify their vehicles, the onboard power source remains a weak link. Fuel cells and secondary batteries are often considered major candidates for providing the primary motive power or serving as load-leveling devices. Due to the relative maturity of the secondary batteries, much effort by academia and industry is devoted to making batteries reliable and affordable for the electrification of vehicles.

In addition to the development of new batteries with better capacity and power capability, an advanced battery management system is also required to better utilize the capacity of the batteries and to provide diagnostic information for the benefit of the driver. Unfortunately, the internal battery states such as energy remaining are not readily available for direct monitoring. The development of a battery monitoring system that accurately estimates the internal states from available external measurements such as voltage and current is thus important.

Thesis Objectives

The internal states of major interest for a battery management system (BMS) are state-of-charge (SOC), state-of-health (SOH), and state-of-function (SOF) [18].

The SOC refers to the available charge inside the battery. The concept is similar to fuel gauge in an internal combustion engine vehicle. However, whereas the

internal combustion engine vehicle maintains the same power capability until the fuel depletes, the battery power capability constantly changes throughout its discharge cycle. The change in power capability comes from both the drop in internal voltage and rise in impedance as the SOC decreases [17, 18].

The most common method for estimating SOC is Coulomb counting. This method has the benefit of being easy to implement, but has the disadvantage of being prone to integrated current sensor error. Another common method is to infer the SOC through the online estimation of open circuit voltage (OCV) [10]. This methodology has been adopted for this research program. However, such methods need to take into account the diffusion effect of the battery, which tends to cause a biased OCV estimation. The thesis provides a methodology to account for the diffusion effect associated with an electric vehicle driving cycle.

The SOH is responsible for determining the wear and aging of the battery [9, 11]. The conventional standard for SOH calls for the replacement of battery once the capacity is reduced to 80% of the original, determined by an arbitrary cut-off voltage. This criterion, while simple, is somewhat arbitrary. The 80% capacity is only valid for a given current profile, usually a constant current discharge; with other discharge profiles, the capacity may very well be different. Another SOH method is to compare the relative impedance between the original and present battery; this is the method adopted in this research program.

The SOF determines the power capability of the battery [18, 45]. Usually framed as a Yes/No answer, the SOF predicts whether the battery can provide the necessary power to complete a task. The criterion is usually a minimum terminal

voltage that the BMS monitors as the threshold for acceptable performance. One method is to find the impedance and OCV of the battery and determine the lowest voltage under the expected current load profile *before* the actual application of the current load. This research program adopts this method. In addition, this thesis looks into the nonlinear nature of the battery impedance and the influence of the nonlinearity on SOF prediction.

The goals of this document are to investigate the state-of-the-art in battery internal states estimation, propose an on-line estimation method for an electric vehicle application, and experimentally verify the proposed method in a laboratory set up and in a test electric vehicle. The estimation method uses on-line system identification techniques to recursively solve for the equivalent circuit parameters. The method relies only on the natural dynamics of the driving cycle load without the injection of additional excitation. Through these on-line adapted parameters and the equivalent circuit, estimated SOC, SOH, and SOF can be provided to the BMS.

The thesis also discusses potential pitfalls for the estimation techniques and the practical issues associated with the implementation of the proposed method in an electric vehicle. For example, the idea of dual observing and its potential issues are discussed in detail in Chapter Three. The thesis seeks to provide the reader with a clear picture of the proposed technique's advantages as well as its limitations. The objective is give the reader the necessary information to implement the methodology based on the thesis discussion and the software code found in the Appendix.

Thesis Organization

The document is organized into four chapters and three appendices. The first chapter provides an extensive state-of-the-art review for battery internal state estimation techniques and the application of these techniques. The second chapter details the structure of the proposed method, its caveats, and also its performance compared with that of the baseline datasheet-based coulomb counting method for state-of-charge estimation.

Chapter Three demonstrates the use of the proposed method as well as its limitations for power capability prediction. A competing variant of the method is also examined in Chapter Three. In addition, Chapter Three analyzes the actual road trip data from the WEMPEC electric vehicle (a Corbin Sparrow) to demonstrate the proposed system's use in diagnosing relative state-of-health.

The last chapter concludes the document with a summary of the major technical contributions of the document, as well as a discussion of proposed future work. The appendices cover the derivation of the EPA driving cycle used in the experiment, the hardware experimental configuration, and the Matlab code used to process the data in accordance with the proposed method.

Chapter 1
The State-of-the-Art Review

1.1 Battery Overview

Batteries in general fall into two categories. Primary batteries are non-rechargeable and are commonly found in consumer electronic products. Common primary batteries include zinc-carbon, zinc-alkaline-MnO_2, zinc-air, and lithium batteries. Secondary batteries are distinguished by their ability to recharge. Examples include lead-acid, Nickel-Cadmium (NiCd), Nickel-Metal Hydride (NiMH), and Lithium-ion (Li-ion) batteries. For vehicular applications, secondary batteries are the preferred candidates for power source or load-leveling devices. Other possible options include fuel cells and ultra capacitors. The energy density and power density provided by the different secondary battery chemistries as well as their cost are important factors for determining their suitability for a particular application [1].

Many commercial secondary batteries are manufactured with a series of cells packaged in a container [2]. A cell is defined as the basic electrochemical unit, while a battery is defined as two or more cells connected in series or parallel configurations to achieve specified operating voltage or current ratings. For example, the BP5-12 battery has a nominal voltage of 12 volts, consisting of 6 cells connecting in series. Since this configuration does not provide access to the internal anode and cathode terminals of each cell in the series string, it is difficult to determine much about the electrochemical status of individual cells from the available battery terminal measurements of voltage and current.

An electrochemical cell most likely contains the following basic components: anode, cathode, electrolyte, and separator [1]. In electrochemical processes, an anode is the electrode where the oxidation reaction occurs, meaning that it releases electrons to the external circuit. A cathode is correspondingly the location where the reduction occurs, collecting the electrons from the anode through the external circuit. For a battery cell, the positive electrode is a cathode during discharge and an anode during charge, while the negative electrode is an anode during discharge and a cathode during charge. In the common literature, however, the convention is to adopt the terminal name designations that are appropriate during discharge operation. The electrolyte is the medium that conducts the ions between the cathode and anode of a cell. The separator is a non-conductive layer that is permeable to ions, yet capable of preventing a galvanic short circuit between the cathode and anode terminals.

In general, a battery manufacturer provides the rated capacity of the battery in their datasheet. The rated capacity, expressed in Ahs (Amp-Hours), is specified for discharging under a stated set of operating conditions. A common discharging condition is to discharge at the rate $\frac{C}{20}$ A, where C is the rated capacity in Ahs until the specified cut-off voltage is reached [2]. Meanwhile, the energy density of a battery is often expressed in Watt-hours per liter $\frac{Wh}{l}$ and the power density in Watts per liter $\frac{W}{l}$ [1].

The physical design of the batteries heavily influences their performance capabilities. In addition to the components for the electrochemical processes, non-reactive components such as the current collectors, separator, and electrolyte are needed

to comprise a functional cell. These components add to the weight of the battery without adding to the energy density.

Most secondary batteries have thin, cylindrical strips for their electrodes. The cylindrical strips are rolled with a separator between the electrode strips and then placed in a cylindrical can. This design tends to achieve a higher electrode surface area that increases the battery power density while lowering the energy capacity due to the increased size of current collector needed to support the electrode [1].

1.1.1 Battery Chemistries

Lead-Acid Batteries

The lead-acid batteries' electrochemical reactions are the following (left to right for discharging) [3]:

Cathode: $PbO_2 + HSO4^- + 3H^+ + e^- \leftrightarrow PbSO_4 + 2\ H_2O$

Anode: $Pb + HSO_4^- \leftrightarrow PbSO_4 + H^+ + 2e^-$

Lead-acid batteries are based on a relatively old technology invented in the 19th century by the French physicist Gaston Plante [4]. The flooded, or wet, cells are very common for industrial use. Since the batteries are usually not sealed, the user can replenish the electrolyte that is depleted during charging through venting [5].

In addition to the flooded type, two common variants exist for the sealed lead-acid batteries. Gel cells immobilize the electrolyte with a thickening agent such as fumed silica. The absorbed glass mat (AGM) batteries use a fiberglass-like separator to hold the electrolyte in place. The advantage of sealing is that the cells are more impact resistance

and can function even with the container has been damaged. But the inability to replenish electrolyte means that overcharging can cause permanent damage to the cells.

The lead-acid battery technology generally suffers little or no memory effect [1]. Memory effect refers to the restricted capacity that some batteries exhibit when they have been subjected to a particular limited range of capacity use. The lack of memory effect makes this technology a strong candidate for back-up power applications. Lead-acid batteries, however, suffer from a relatively low energy density and irreversible capacity loss during deep discharge.

Nickel-Cadmium Batteries

One version of the NiCd batteries' electrochemical reactions is the following (left to right for discharge) [6]:

Cathode: $NiOOH + H_2O + e^{1-} \leftrightarrow Ni(OH)_2 + OH^{1-}$

Anode: $Cd + 2OH^{1-} \leftrightarrow Cd(OH)_2 + 2e^{1-}$

The NiCd battery has a reputation for being robust and low cost. Due to its robustness, NiCd batteries can be charged at a higher rate and thus in a shorter time. However, NiCd batteries suffer from the memory effect. With a few complete charge/discharge cycles, the memory effect can be overcome. Another drawback to NiCd batteries is that they have relatively low energy density [1].

Nickel-Metal Hydride Batteries

The electrochemical reaction can be the following (left to right for discharge) [6]:

Cathode: $NiOOH + H_2O + e^{1-} \leftrightarrow Ni(OH)_2 + OH^{1-}$

Anode: $Alloy[H] + OH^{1-} \leftrightarrow Alloy + H_2O + e^{1-}$

NiMH batteries represent an improvement over NiCd batteries in terms of energy density. They still suffer the memory effect despite the fact that some manufacturers claim otherwise. A drawback of the NiMH batteries is that it has a greater self-discharge rate compared with NiCd batteries. Also, since NiCd batteries absorb heat during charging while NiMH batteries generate heat during charging, NiMH batteries need to be more carefully regulated thermally during rapid charging [1].

Lithium-ion batteries

One possibility for the Li-ion battery reaction, depending on the electrodes, is the following [7]:

Cathode: $Li_{1-x}CoO_2 + xLi^+ + xe^{1-} \leftrightarrow LiCoO_2$

Anode: $Li_xC_6 \leftrightarrow xLi^+ + xe^{1-} + 6C$

A common anode material for Li-ion batteries is graphite, while the cathode material has many options of Li-based oxide. The electrolyte used in Li-ion batteries is an organic solvent, commonly ethlyene carbon (EC). The EC reduction with Li^+ forms a protective layer on the graphite anode surface that regulates the intercalaction of Li^+ and graphite during charging and increases the battery life [8]. One advantage of the Li-ion

batteries is that they have a considerably higher energy density than the preceding battery types. However, overcharging Li-ion batteries may lead in some cases to high dangerous conditions including explosions. As a result, careful control of the battery operating conditions must be implemented by the battery monitoring system [1].

1.1.2 Chemical Processes

Thermodynamics and Nernst's Equation

When the battery is at rest, the electrode potentials and the resulting cell potential are functions of the concentration of the reduction and oxidation species. The cathode equilibrium potential of each electrode can be described by Nernst's Equation as follows [1][9]:

$$E^{+}_{eq} = E^{0}_{+} + \frac{RT}{nF} \ln \frac{(a_{ox+})^{B}}{(a_{red+})^{A}} \tag{1.1}$$

while the anode equilibrium potential is:

$$E^{-}_{eq} = E^{0}_{-} + \frac{RT}{nF} \ln \frac{(a_{ox-})^{B}}{(a_{red-})^{A}} \tag{1.2}$$

where E^0 is the standard redox potential of the electrode, R is the gas constant (8.314 $\frac{J}{mol.K}$), T is the temperature (in deg K), F is Faraday's constant (96485 $\frac{C}{mol}$), n is the number of electrons involved in the charge transfer reactions, and a is the concentration of a particular species identified by the associated subscript. Given (1.1) and (1.2), the electrochemical potential of a cell in equilibrium is then:

$$E^{bat}_{eq} = E^{+}_{eq} - E^{-}_{eq} = E^{0}_{+} - E^{0}_{-} + \frac{RT}{nF} \ln \frac{(a_{ox+})^{B} (a_{red-})^{D}}{(a_{red+})^{A} (a_{ox-})^{C}} \tag{1.3}$$

This potential E^{bat}_{eq} is also known as the open-circuit voltage (OCV), serving as an indicator of the chemical energy reservoir in the cell.

Electrode Kinetic Overpotential and the Butler-Volmer Equation

When an electrochemical cell is connected to an external circuit, the voltage across the cell is not simply described by (1.3). With a current flow, one of the voltage drops in the cell that makes the terminal voltage different from the open-circuit voltage is the electrode kinetic overpotential [9]. The Butler-Volmer equation describes the relationship between the current and the electrode overpotential [1].

$$I = I_o - I_{red} = I_0 \{\exp(\alpha \frac{nF}{RT}\eta) - \exp(-(1-\alpha) \frac{nF}{RT}\eta)\} \tag{1.4}$$

where I_o is the oxidation current, I_{red} is the reduction current [A], I_0 is the exchange current constant [A], α is the charge transfer coefficient [unitless], and η is the overpotential across the electrode/electrolyte interface [V]. When α equals 0.5, the electrode has a symmetrical charge transfer function for both charging and discharging, which is not the case for most electrochemical cells. For a large value of η, either I_o or I_{red} in (1.4) will dominate. At a given operating condition, one of the electrodes will limit the charge transfer current. In some literature, the Tafel relation is used to simplify the Butler-Volmer equation in (1.4) by assuming a dominant current direction.

$$\eta = \frac{RT}{\alpha nF} \ln(\frac{I}{I_0}) \tag{1.5}$$

Notice that the parameters α and I_0 could change throughout the operating range. The assumption that they are fixed values can simplify the equations but increases the error for the model prediction [9].

Diffusion Effect

When current is flowing, the concentration profile of the reaction species is not uniform throughout the electrolyte. The overpotential driving the charge transfer reaction is thus not the only voltage drop affecting the cell terminal voltage. The additional overpotential caused by the diffusion effect of the species in charge transfer reaction is described as:

$$\eta^d = \frac{RT}{nF} \ln\left(\frac{C^s}{C^b}\right) \tag{1.6}$$

where C^s is the concentration of the species on the electrode surface [moles] and C^b is the concentration of the species in the electrolyte bulk [moles]. Since in real applications the diffusion process is not stationary, it becomes very difficult to solve the diffusion equations analytically. However, models exist to iteratively solve for these conditions with certain assumptions about the boundary conditions [1].

Mass Transport Limit

When the current through the cell becomes extreme, the limiting factor in the rate of reaction becomes the transport rate of the reactant from electrolyte to electrode [9]. The availability of reactant species in the area adjacent to the electrodes determines how easily this limit is reached. As a result, an increase in the electrode area can help to alleviate this issue.

Fast Dynamic Element

In a practical cell, there are electrical phenomena that are fast reacting, such as the resistance through the separator, electrolyte, etc. This resistance contributes another voltage drop that makes the terminal voltage different from the open-circuit voltage [9]. This lumped resistance can be dependent on the amount of energy remained in the electrolyte, surface condition of the electrode, and temperature.

1.2 Battery Applications and Monitoring System

A battery monitoring system is responsible for determining the suitability of the battery in question for an application. Battery applications can be roughly divided into several categories. Accordingly these applications require the battery monitoring system to provide information such as state-of-charge (SOC), state-of-health (SOH), and state-of-function (SOF), as in Fig. 1-1. The following discussion will focus on the descriptions of the SOC, SOH, and SOF and state-of-the-art monitoring techniques. Several of these techniques are also listed and categorized in Fig. 1-1 as a reference to how the system identification of equivalent circuit parameters, the methodology pursued in this document, fits into the overall landscape of the battery monitoring system research.

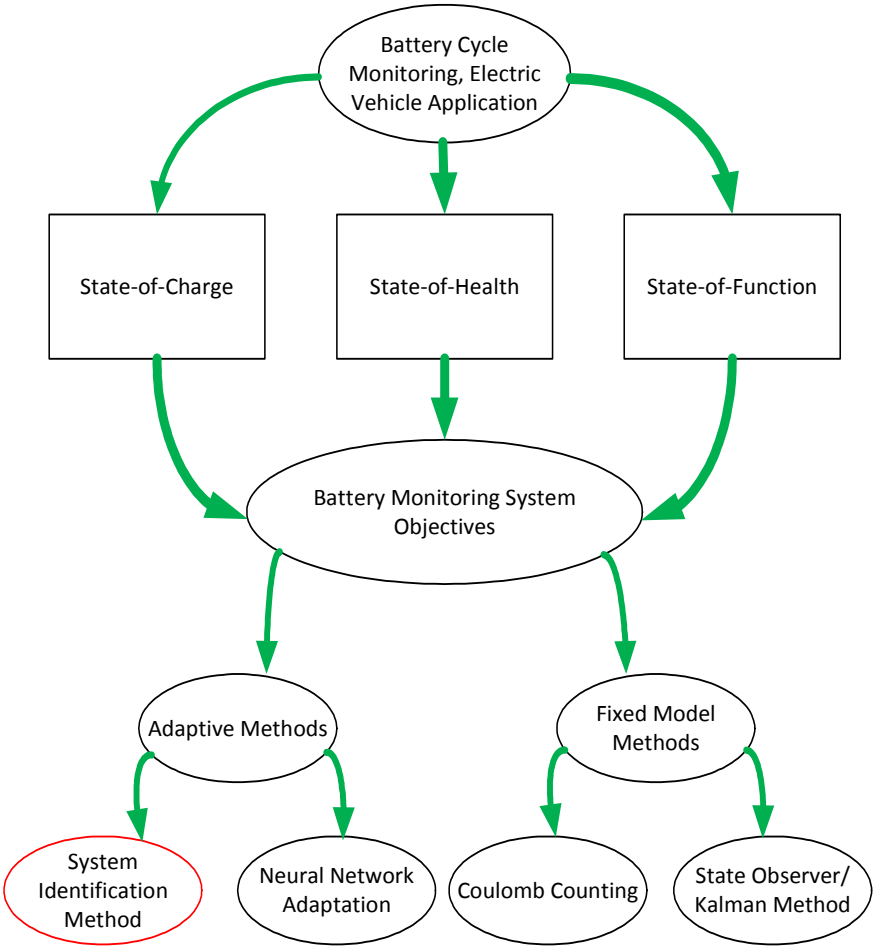

Fig. 1-1 Summary Diagram for Research Approach Relative to Current State of the Arts

One of these battery applications is the use of battery as the main power source. In this case, the tasks of the battery monitoring system are mainly to estimate the remaining service time for the application restrained by the currently available energy in the battery and also to determine the approximate calendar service life of the battery. This category includes applications such as uninterruptible power supplies (UPS) and electric vehicles (EVs). However, the frequency of battery use in different applications will require different functions for the battery monitoring system.

In the literature, the remaining service time for the application restrained by the available energy is usually referred to as the state-of-charge (SOC), with the implicit

assumption that the terminal voltage of the battery is relatively constant throughout the operation. Under this constant-voltage assumption, the electric charge, i.e., the integral of the current, suffices to quantify the energy content of the battery [10]. In addition, the literature also refers to the battery remaining service calendar life as the state-of-health (SOH), reflecting the impact of battery aging mechanisms [11].

Another battery application is to serve as a load-leveling device in a system where multiple power sources, including batteries, are present. In this case, the battery monitoring system needs not only to provide information on the SOC, but also the capability of the battery to provide the needed power for the load [9]. Notice that this capability to meet the load power request is not necessarily the same as the SOC. Although batteries at low SOC tend to have a degraded instantaneous power capability, having sufficient energy in the battery may not be enough to satisfy the load application. This category includes batteries in hybrid electric vehicles (HEVs) and semi-independent power systems known as microgrids.

One other battery application is to provide the required power for starting the load. The most common example of this application category is the starter battery for automobiles. The starter battery is responsible for providing the high current needed to start the vehicle. In this case, the battery monitoring system needs to determine the cranking capability of the battery as a Yes or No function. This is an example of the state-of-function (SOF) monitoring capability being critical to the application.

1.3 State-of-Charge

For the SOC estimation, one thing worth noting is that due to the diffusion effect, the concentration of the reaction species in the area adjacent to the electrodes is not

necessarily the same as that of the bulk electrolyte [9]. As a result, even with energy remaining in the cell, it might not be possible to extract the energy at the power rate required by the application. In other words, having sufficient SOC may not mean that the battery is capable of meeting the performance requirements for the application.

In general the SOC is simply defined by Coulomb counting, as discussed in the following subsection. However, since the collapse of a battery's terminal voltage is strongly discouraged for maintaining battery health, the definition of SOC can be further elaborated as the charge available for extraction before the terminal voltage reaches a pre-defined cut-off voltage. Most battery manufacturers provide information on the discharge time vs. terminal voltage for various discharge current rates. A source for potential inconsistency with using only one discharge current vs. terminal voltage curve for SOC to describe the state of the battery is that different discharge current rates will result in differences in the battery energy available for extraction. This phenomenon was first formulated by Peukert's Law [12]:

$$K I^{n-1} = \text{const.}, n > 1 \tag{1.7}$$

where K is the available battery energy capacity [Ah] as a function of discharge current I, and n is determined by the characteristics of the battery. When n = 1, the battery is ideal and its capacity is not affected by the discharge current. Typical values for n fall in the range from 1.2 to 1.5 [12].

In addition, the battery capacity is also affected by temperature and cut-off voltage limit. The temperature at which the battery operates is directly related to its thermodynamics, which determine the battery OCV. Intuitively, this additional variable will influence the battery discharge capacity defined by a cut-off voltage limit.

Given the discussion above, it can be stated that having the same SOC value as defined by the Peukert's law does not necessarily mean that the battery is in the same condition. In addition, the batteries may have varying internal impedances, thus causing the battery power capability to differ despite the same SOC condition, whether defined in the pure Coulomb counting method or in the Peukert modification method.

1.3.1 Coulomb Counting

The most basic way to estimate SOC online is by coulomb counting. Given a fixed amount of total coulombs available Q_{total} when SOC = 1 (in normalized per unit), the current SOC can be found by:

$$SOC = \frac{Q_{total}-Q_{out}}{Q_{total}} \times 100\% \tag{1.8}$$

In a quasi-stationary load scenario where the battery current is constant at a certain value for a significant amount of time before switching to another value, it is possible to normalize the current output's effect on SOC using the discharge curve for different discharge currents provided by the battery manufacturer. This provides a means of taking into account the capacity variation described by Peukert.

Many other variants of the coulomb counting method, often with Peukert modifications, exist in the literature [13], [14], [15].

The coulomb counting SOC estimation method is highly susceptible to current measurement errors which cause an integrated error for coulomb counting that is aggravated over time. If the application allows periodic full recharging, the SOC estimation can be reset in order to overcome this limitation, assuming the recharging algorithm is consistent.

Another problem with the coulomb counting method is that during charging, not all of the energy is absorbed by the main battery chemical process [16]. The internal impedance of a cell and thus efficiency coefficient is related to the SOC, temperature, current magnitude, etc. As a result, the inability to measure this efficiency coefficient makes the coulomb counting method less reliable for SOC estimation in applications where regenerative braking supplies energy back into the monitored batteries.

1.3.2 Voltage-Based Methods

Another method to determine the SOC is by its terminal voltage, either in open circuit or connected to an external load. The open-circuit terminal voltage is a fairly accurate indicator of SOC as discussed 1.1.2. However, the open-circuit terminal voltage measurement needs to be taken after a rest period in order for the diffusion process inside the battery to be completes. This rest period requirement significantly reduces the opportunities for using this technique to accurately predict SOC in an online battery monitoring application. The terminal voltage with an external load can be measured online, but it is not an ideal indicator of SOC due to voltage fluctuations caused by load current variations and the diffusion process dynamics. In addition, battery manufacturers strive to maintain relative terminal voltage stability even as the battery is being discharged.

1.3.3 Impedance-Based Methods

For various types of batteries, impedance-based methods have been proposed to estimate SOC. The basic idea is to measure the impedance spectra at different SOCs in an effort to correlate the measurements with the change in SOC. Several parameters are

proposed as the possible candidates for SOC indicators, including high frequency resistance, resonant frequency, and voltage relaxation time constant [17], [18], [19], [20].

A common method in the literature to obtain battery impedance information is impedance spectroscopy. A small excitation signal, normally a sine wave, is injected into the battery and the response is measured to calculate the impedance. In galvanostatic mode, the DC part of the current signal is controlled either at zero or some fixed value, while a small current sine wave is injected. The magnitude of the voltage response needs to be smaller than 10 mV to avoid exciting the nonlinearity of the battery [21]. A complication of this method for measuring battery impedance is that the results can be heavily influenced by the physical wiring connection, e.g. pressure on the connector [12], [21].

Two methods exist to apply impedance spectroscopy to compare the difference in cell impedance for different SOCs. One is to discharge to the desired SOC and then apply impedance spectroscopy, and the other is to perform impedance spectroscopy while charging or discharging with a DC current. The advantage of the latter is to be more realistically mimicking a real-time application, but the disadvantage lies in the fact that the SOC is continuously changing when the impedance measurement is being taken [21]. By analyzing the impedance information for different frequencies, an electrical equivalent circuit can be constructed. Interpretations for the components of the equivalent circuit are common-place in the literature.

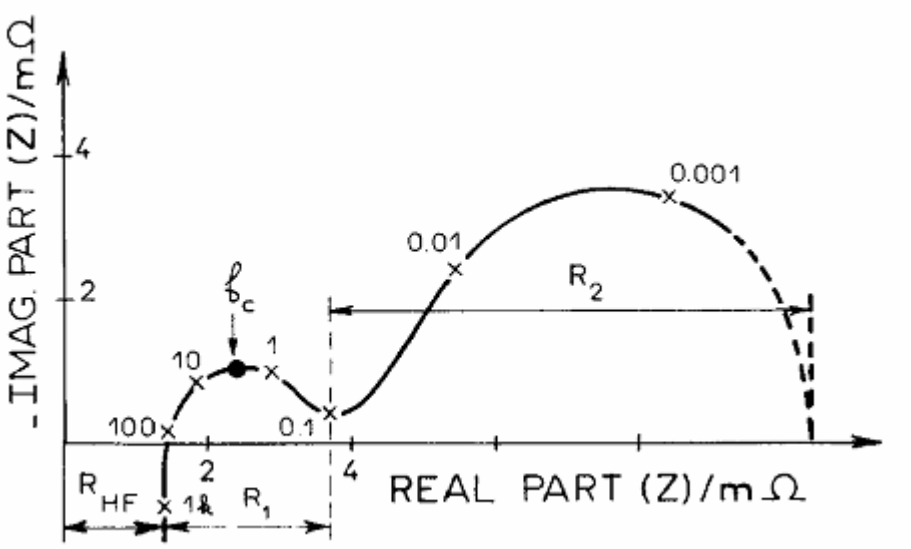

Fig. 1-2 Impedance Spectroscopy Nyquist Plot Example [21]

For lead-acid batteries, Huet et al proposed to measure the high-frequency resistance of a 1200 Ah cell and found it to have a nonlinear relationship to the SOC [17]. In addition, they found that the high-frequency resistance for SOC = 0 varies based on the discharge current rates. The authors explain the change in the high-frequency resistance by the blocking effect of $PbSO_4$ crystals, instead of the electrolyte [17].

In a later study, Huet et al monitored the change of battery high frequency resistance during cycling at rates between C/100 and C/10. The results show that at high discharge rate, the high-frequency resistance increases gradually as SOC decreases. At low discharge rate, the high-frequency resistance stays constant and only increases sharply at low SOCs. Since the high-frequency resistance provides information on the $PbSO_4$ layer structure, it depends on the history of the previous cycling of the cell. For different discharge rates, different SOC values may correspond to the same value of high-frequency resistance [22].

For lead-acid batteries, Blanke et al proposed that through impedance spectroscopy, the frequency at which the battery impedance turns from capacitive to inductive, i.e. the resonant frequency, can be determined and used as an indicator for SOC. However, this particular method is susceptible to errors induced by temperature variations. Despite the successful experimental results, it has not been demonstrated that a pure impedance-based method is sufficient in real-life applications. Self-learning mechanisms have been proposed to help calibrate the system based on resonant frequency measurements [18]. In another paper, Ni-MH and Ni-Cd batteries are examined and it was found that their resonant frequencies are also correlated to SOC [19]. These studies use coulomb counting as their yardstick for SOC comparison. The effect of a dynamic load on the short-term power capability at lower SOC is not considered.

For a fully-sealed, 25 Ah lead-acid battery, Hughes et al use a simplified (one electrode) Randles battery equivalent circuit and find its "charge-transfer" resistance and "double-layer" capacitance through impedance spectroscopy. They suggest using the product of the "charge-transfer" resistance and "double-layer" capacitance as the battery's time constant and an indicator of the SOC [20]. This result is consistent with the discussion in Section 1.1.2., where the Bulter-Volmer equation's constants are said to be changing with operating points, e.g. SOC.

Coleman et al report a method for determining SOC-based on the high-frequency impedance (1 kHz) and the estimation of open-circuit voltage. The high-frequency impedance is measured with an injected carrier frequency. In essence, the method substitutes the impedance spectroscopy method with a single frequency to achieve the speed required for online application. Based on the high-frequency impedance, the total

impedance is estimated in a per unit fashion. The impedance information, along with some observation laws, deduces the open-circuit voltage obtained through KVL. The claim is made that the internal resistance is not a reliable indicator of the state-of-charge, having only little change for SOC > 50% and this approach helps mitigate that limitation [23].

1.3.4 Online Estimation Methods

Various methods have been proposed to estimate SOC, i.e., stored energy (not available energy), online through schemes such as Kalman filter and impedance parameter estimations. Plett wrote a series of summary papers on the Kalman filter and extended Kalman filter technique for estimating internal battery states, including SOC [24], [25], [26].

To use a Kalman filter to estimate SOC, relationships between SOC and some other measurable quantities, e.g. voltage and current, must first be established. Several known relationships between terminal voltage and SOC are used to form a model. The long-term diffusion RC time constant is modeled as a 'hysteresis' phenomenon between the charging and discharging operating regions for the same SOC. The short-term RC time constant describing the charge transfer and double-layer processes is modeled as a linearly filtered voltage as a function of the input current that converges to zero when the current is constant.

To capture the system parameters offline for the online estimator, least square method can be used for linear models, while an extended Kalman filter can be used for nonlinear models and the parameters are treated as constants with perturbations. Overall, these filter approaches assume the system parameters to be constant and that the process

white noise part of the filter equation handles the change of the system parameters over time.

Other Kalman filter-based techniques exist in the literature, but the only differences are in how the models are obtained and the assumptions that are made in the process of deriving the models [27], [28], [29], [30].

Another genre of methods that has been proposed to estimate online the internal states of a battery for hybrid electric vehicle applications uses recursive system identification technique to estimate the impedance of a cell. The open-circuit voltage can then be estimated using KVL and terminal voltage measurements, yielding estimates of the SOC [9], [31]. This genre of approaches will be a starting point for the method proposed in this document.

1.3.5 Neural Network and Fuzzy Logic Methods

As a testament to the importance as well as elusiveness of SOC online estimation, many other methods have been proposed. Genres of these approaches include neural network [32] and fuzzy logic [33]. These methods are based on observation laws. One can think of them as mathematically advanced Peukert modification methods for dynamic load conditions. Notwithstanding the lack of physical/chemical modeling, these methods can have good performance for their designed applications. It's worthwhile to note that this kind of approach implicitly take the power capability into account through the learning process, thus providing an online estimation of SOC.

1.4 State-of-Health

SOH serves as a relative indicator for battery aging. It has been claimed that the aging process comes from the effect of previous battery history [34], [35]. For lithium-ion batteries, the storage time, storage temperature, and SOC during its storage are also shown to be related to capacity loss [36]. Additionally, temperature during operation has been identified as a major aging accelerator for batteries due to the facilitation of irreversible reactions [36], [37].

Aging can be detected through a comparison between two discharge cycles. As discussed above, most battery manufacturers provide discharge time vs. terminal voltage for different discharge current rates. A fresh battery would ideally follow these curves when discharging while an aged battery tends to suffer drops in its terminal voltage more quickly due to increased internal impedance. If the SOC is evaluated as the total charge available for discharge until the cut-off terminal voltage is reached, then an aged battery tends to have a lower capacity.

Since the voltage deviation between batteries of different ages can be pronounced for partially-discharged conditions, e.g. SOC = 70%, it is possible to detect SOH by only partially charging or discharging the battery using the coulomb counting method in order to determine the SOC. This method allows for the detection of major cell failures but is not a reliable method to estimate actual capacity [12].

Several SOH estimation methods based on impedance measurements are also proposed in the literature [11], [18], [38].

Overall two major contributing factors exist to influence the SOH. One is the loss of active material in the battery, causing a loss of capacity. The other is the increase in

impedance for various reasons, contributing to an early termination of charging and discharging events.

1.4.1 Observations Between Cycles

As discussed above, a common method to detect the relative health of a battery is to observe what the capacity is for the same discharge cut-off voltage. This method is commonly used by chemical engineers studying battery aging effects [39], [40]. An obvious prerequisite for this method is to keep the charging and discharging conditions constant, including temperature, current, and cut-off voltages.

1.4.2 Impedance-Based Method

For lithium-ion batteries, Blanke et al applied the impedance spectroscopy method to cells subjected to accelerated aging by storing the cells at elevated temperatures. They report an increase in high-frequency resistance. With the help of the reference node inserted in the tested batteries, both positive and negative electrodes are subjected to impedance spectroscopy. It is found that, while the negative electrode impedance does not change during the accelerated aging test, the positive electrode contributes much of the increase in impedance. The increase in impedance is attributed to the increase in the resistance of the contact area between the electrical current collector and the positive active mass [18].

Also for lithium-ion batteries, Tröltzch et al reported that the real part of the impedance at 1 kHz (high-frequency resistance) is relatively constant between charged and discharged state (i.e. within one cycle) but increased approx. 58% above its original value over 230 cycles while the battery exhibited a 14% decrease in capacity [38].

Osaka et al conducted a study on lithium-ion batteries aging using impedance spectroscopy. By fitting the results from impedance spectroscopy to their equivalent circuit model, it was determined that the aging process in mainly due to an increase in cathode impedance and anode capacity loss [41]. This result corresponds to the study of Blanke et al on the cathode impedance increase.

Coleman et al presented a two-pulse load aging test for a VRLA battery. This method determines the SOH by measuring the change in battery terminal voltage during the second pulse which is claimed to be correlated to the capacity of the battery and thus SOH. They found that the change in voltage is more pronounced for batteries that have aged. The reasoning is that with a decreased capacity, the same current load would have a more significant impact on the aged battery [11]. Notice that this method mostly measures the response of the charge transfer function described by the Butler-Volmer equation. Perhaps a loss of electrolyte and/or its reaction species affects the charge transfer response.

1.4.3 Computational Modeling for Aging Prediction

A summary paper by Sauer et al describes three approaches to predicting aging of a battery during its operating lifetime [42]. The three methods are: physical-chemical processes model, Amp-hour counting model with weighting to emphasize aging during severe operation, and a special event-oriented concept that utilizes pattern recognition to identify severe operating conditions.

The physical-chemical processes model has the advantage of being detailed, including many parameters such as SOC, species concentration, etc. The model also self-adjusts to parameters changes due to aging. However, the process of constructing the

model, determining the parameters, and computing the model require considerable analysis, experiments, or computational power. The other two methods are less complex and faster in execution, but require expert knowledge to relate the measured data to the aging process.

Other sources in the literature discussed methods for predicting the aging process, but the ideas are mostly similar to those covered by Sauer et al [34], [43], [44].

1.5 State-of-Function

The term state-of-function (SOF) is used to describe the cranking capability of a battery. The concern in this case is the short-term power capability, which is dependent on the energy remained in the battery, temperature, and health. A key point is that the presence of energy remaining in the battery does not mean that the energy is accessible to the particular application [9]. SOF can normally be evaluated using the terminal voltage during a specified current profile. If the terminal voltage is stable and doe not collapse during the load current profile, it means the battery has successfully transferred the required energy for the application.

Despite the fact that the SOF of a cell is highly dependent on SOC, SOH, and temperature, a given set of SOC, SOH, and temperature conditions still does not necessarily define the SOF [45]. For example, after rest the internal impedance of a battery may decrease. As a result, despite the same given operating conditions, the transient behavior of the battery can be quite different before and after rest.

1.5.1 Impedance-Based Method

Multiple impedance/electric circuit model approaches have been proposed in the literature to predict the SOF. Some of these methods are commercialized or patented. Most of these methods seek to predict the lowest terminal voltage for a battery model exposed to the expected current load profile.

In [9], Wiegman exercised his online-estimated models based on system identification techniques to predict the short-term voltage behavior of the battery under test. Different modeling complexities are compared for prediction performance. Different operating regions for current are also investigated for the model. In general, the prediction errors were reduced by an increase in modeling complexity.

A similar approach proposed by van Bree et al involved a related equivalent circuit [45]. The approach used during this study is similar to the one taken by Wiegman. The method to populate the equivalent circuit, however, was different. Van Bree et al chose to gather a batch of current and voltage data, and then perform an offline, nonlinear parameter estimation technique to populate the equivalent circuit parameters. In addition, the nonlinear characteristics of the battery investigated were considered in the model by modeling the Butler-Volmer equation in its original form instead of linearizing it as a resistor. The results seemed promising as the agreement of the model prediction and the measurement data is strong. However, it should be noted that this method is only valid for the special case where the battery remains at a constant SOC.

The Japanese company Hitachi has introduced a new smart car battery named “CYBOX” [46]. The idea is to measure, memorize, and compare terminal voltages during cold cranking operation, while the open-circuit voltage is tracked for SOC

indication. By pre-setting the criteria for recharging and replacing the batteries, the user will receive a SOF recommendation based on the performance of recent battery cold cranking events. A major selling point of this product is that it requires no current measurement for the algorithm. This simplification is based on the assumption that the power demand is relatively repeatable for a given cranking application. In essence, the impedance information is given by the transient response of the battery voltage during cranking, which keeps track of SOH. The SOC developed from the terminal voltage measurements is combined with the SOH information to provide an indicator of the SOF.

A patent awarded to Bramwell discloses an invention that provides car battery SOF diagnostics [47]. The invention consists of a current source, voltmeter, temperature sensor, and control unit. The voltmeter monitors the battery voltage response during an artificially created current pulse to determine internal impedance. The open-circuit voltage, impedance, and the temperature information are then combined to provide information for the control unit to determine the SOF.

1.5.2 Nonlinear Modeling

While the equivalent circuit approach can predict the terminal voltage with certain accuracy at certain specified operating conditions, it needs to be pointed out again that the fast RC dynamic response is nonlinear. The charge-transfer behavior can be modeled as in (1.4) or its Tafel simplification form (1.5). Perhaps it would be possible to improve the prediction accuracy by invoking the nonlinear equation instead of relying on the linearized RC structure. In [48], Buller et al compare the results from nonlinear circuit modeling based on impedance spectroscopy data and its RC linear modeling simplification, and found that certain aspects of the battery time-domain response can be

better approximated using nonlinear modeling based on frequency-domain data than the simplistic RC model.

1.6 System Identification Techniques

System identification is a digital control technique that adjusts the model parameters using measured data. This can be achieved either offline using a batch of recorded data or, alternatively, it can be accomplished recursively online. The recursive method will be the focus of this section, but the offline method is also used for parameter initialization in this document. A prerequisite to this method is an understanding of the order as well as the structure of the physical system to be modeled. With a given physical model and its corresponding discrete-time equivalent, the technique can be used to estimate the parameters of the discrete-time transfer function that best fits the data.

Variants of the online parameter estimation exist; for example, Wiegman used the output error algorithm for his battery state estimation [9]. The approach used in this document will, instead, use the equation error algorithm, and it will be the focus for the remainder of the section. The differences between the output error and equation error approaches will also be discussed in the following subsection.

1.6.1 Equation Error Algorithm

The following transfer function can be considered to be a generic representation of a digital system, where z^{-1} is one time sample delay.

$$\frac{b_0 + b_1 z^{-1} + b_2 z^{-2} + \ldots}{1 + a_1 z^{-1} + a_2 z^{-2} + \ldots} \tag{1.9}$$

Using Eq. (1.9) as the model, the output prediction $\hat{y}$ can be written as a function of the input u as follows:

$$\hat{y}(k) = \frac{b_0 + b_1 z^{-1} + b_2 z^{-2} + \ldots}{1 + a_1 z^{-1} + a_2 z^{-2} + \ldots} u(k) \tag{1.10}$$

Equation (1.10) can be algebraically expanded and the resulting difference equation is then:

$$\hat{y}(k) = b_0 u(k) + b_1 u(k-1) + \ldots + b_{nb} u(k-n_b) - a_1 y(k-1) - \ldots a_{na} y(k-n_a) \tag{1.11}$$

where the y's are the measured quantities instead of predicted output quantities $\hat{y}$'s. The appearance of the measured output values on the right side of the equation is the difference between the formulation of the equation error method that uses measured y's and the output error method that uses predicted $\hat{y}$'s. The value n denotes the system order. Based on (1.10) and (1.11), (1.10) can be rewritten as:

$$\hat{y}(k) = \Phi \ \theta \tag{1.12}$$

where θ is the array of parameters $[b0, b1, \ldots, a1, a2, \ldots]^T$ and Φ is the regression vector:

$$\Phi (k, \theta) = [u(k), \ldots, u(k-n_b), -y(k-1, \theta), \ldots, -y(k-n_a, \theta)] \tag{1.13}$$

The mechanism for updating parameters based on the prediction output and measured output can now be described. First select a cost function which should be minimized. An obvious candidate would be the square of the prediction error, $(y(k) - \hat{y}(k))^2$. If the least square error as a function of the parameters is desired, the derivative of the squared error with respect to the parameters should be tuned to zero. Specifically,

$$\frac{d[y(k) - \hat{y}(k)]^2}{d\hat{\theta}} = -2(y(k) - \hat{y}(k))\Phi(K) \tag{1.14}$$

$$\hat{\theta}(k) = \hat{\theta}(k-1) + c\Phi^T(k)[y(k) - \hat{y}(k)] \tag{1.15}$$

where c is an estimator gain that incorporates the -2 in (1.14). Reexamiing (1.14), the math is based on (1.12) and the chain rule derivative. Notice that since the measurement is not a function of the parameter estimation, the derivative of y with respect to $\hat{\theta}$ is zero.

Based on (1.15), it can be seen that if the prediction is perfect, i.e. $y(k) = \hat{y}(k)$, then the parameters are not updated and the estimation system has converged. The value of c cannot be too big because of stability issues. But if it is too small, the convergence speed will suffer. In addition, the value of c can be gradually increased as a function of time to provide a forgetting factor that weights the later estimates more heavily.

1.6.2 Discrete Equivalents to Continuous Transfer Functions

Methods exist for mapping the continuous domain transfer functions into the discrete domain. The details can be found in references such as Franklin and Powell's book [49]. The zero-hold equivalent is the following:

$$H(z) = (1 - z^{-1})\, Z\{\frac{H(s)}{s}\} \tag{1.16}$$

where H(s) is the S-domain transfer function. This method converts an impulse function in the continuous domain to a latched pulse with duration of the sampling period in the digital domain. Other integration-based methods include the forward rule, backward rule, and bilinear rule that are summarized in Table 1-1.

Table 1-1 Integration-Based Discrete Equivalent to Continuous Domain Methods

Method	Approximation
Forward Rule	$S \leftarrow \frac{z-1}{T}$
Backward Rule	$S \leftarrow \frac{z-1}{zT}$
Bilinear Rule	$S \leftarrow \frac{2}{T}\frac{z-1}{z+1}$

In this document, the forward rule will be used for this continuous-to-discrete transformation because of its simplicity.

1.7 Summary

From the review of the state-of-the-art presented in this chapter, it is apparent that many researchers are working to estimate the internal states of the battery either online during battery operation or offline between two operating periods. The information obtained in general can advise the user on the remaining battery energy (SOC), health of the battery (SOH), and the cranking capability of the battery (SOF).

Many of the online estimation techniques developed have been explored for use in battery management system. The effectiveness of these techniques depends on, among other things, the reliability of the battery dynamic models that they utilize. Both observational laws such as estimated open-circuit voltage as a function of Amp-hour outflows or electrical equivalent circuits estimated from measured voltage and current data can be used for online estimation to predict SOC. However, as far as the power capability prediction is concerned, the equivalent circuit approach seems most suitable since it can predict the terminal voltage based on the current load profile required, despite the nonlinear nature of the battery.

Much work on the online estimation of SOF is based on the impedance information obtained from recent voltage and current measurements. The assumption is that if the impedance can be known and the OCV can be treated as a constant for a short term period, the power capability of the battery can be predicted. Improving the online SOC prediction might be achieved if the prediction of the remaining energy is augmented with information on power capability that is embedded in the battery impedance.

The Peukert modification approach attempts to estimate useful energy, thus taking into account SOF, for static operating conditions. The fuzzy logic approach also takes the SOF into account indirectly for more dynamic operations. But an equivalent circuit-based model can provide information on both power capability and remaining energy while the SOH information may be inferred from impedance and cycle data. Thus, the equivalent circuit-based model provides a versatile approach for BMS.

The system identification technique appears to be a promising method for populating the model parameters online based on measurement and model prediction differences. The key to success is to find equivalent circuit models that are consistent with the underlying physical/chemical processes such that the parameter updater has a good chance of catching up with the ever-changing battery status.

Another approach, typically implemented with the Kalman filter, is to use the discrepancy between prediction and measurement to update the states in the model instead of the parameters. This approach has the drawback of not being able to keep up with the changing battery conditions that affect the parameter values.

In [9], Wiegman proposed a system identification-based method for online monitoring the battery characteristics for the HEV application. The driving cycles

investigated in [9] were in the hundreds-of-seconds range. The system identification method employed thus only needed to remain stable in this time range. The utilization of the information obtained in the model is also limited to this same time range.

As illustrated in Fig. 1-1, the emphasis of this work is to establish an adaptive methodology for electric fvehicle battery monitoring system. One of the distinguishing features of this research from Wiegman's earlier work is that the objective of this new work is to develop a battery model that can be used for electric vehicle batteries that undergo deep discharge cycles in contrast to the batteries in hybrid vehicles that are operated in charge-sustaining modes with much smaller state-of-charge excursions. This work proposes to implement the system identification based method on the EV driving cycle, investigate the implementation issues of the estimation system, and present the results of the system in the context of the EV cycle.

Chapter 2

Lead-Acid Battery Equivalent Circuit Model and State-of-Charge Estimation Methodology

This chapter will develop the lead-acid battery equivalent circuit model corresponding to the chemical processes presented in Section 1.1.2. The model will be discussed in detail and the methodology to populate the model parameters will be shown. The chapter then focuses on the comparison between SOC estimation derived from this methodology and from the coulomb counting method.

2.1 Statistical RC Model for Lead-Acid Battery

The Randles equivalent circuit model is commonly seen in the literature. While the chemical processes are significantly higher-order than most of the models presented in the literature, good results have been obtained using the reduced-order, lumped model. Wiegman discussed the reduction of the Randles model to a lower order and its ramifications in [9]. For example, as there is not a reference electrode available to differentiate the behavior between cathode and anode, their individual RC structures related to their current rate as a function of overpotential can only be observed together. In addition, most commercially-available batteries consist of individual cells connected in series. These individual cells cannot be differentiated by information at the terminals.

2.1.1 Model Formation

Fig. 2-1 shows the Randles equivalent circuit model for a lead-acid battery [9]. The resistor R_0 is the element responsible for any fast dynamic voltage response to a current change. It is usually a combination of effects associated with the separator and the impedance contributed by the electrodes.

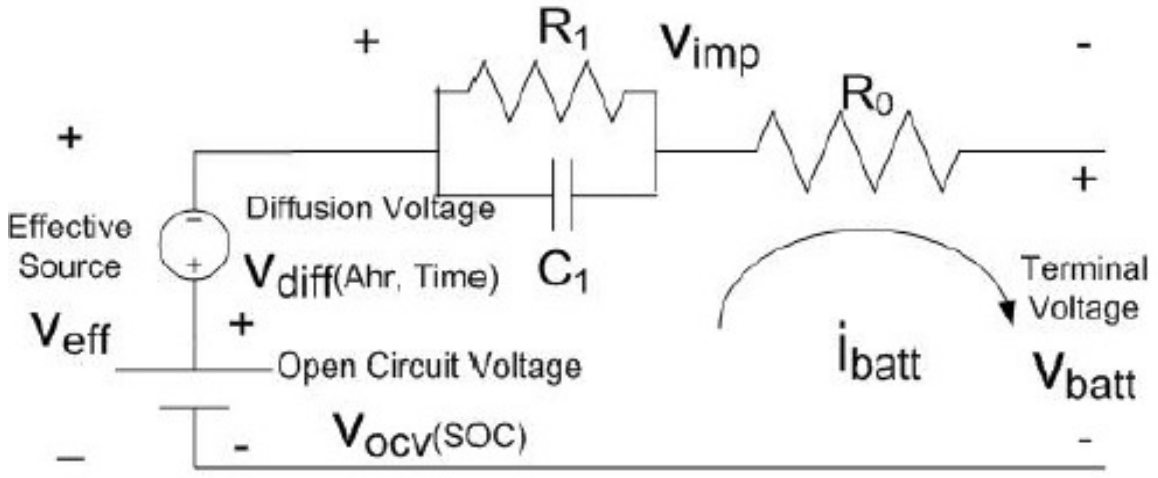

Fig. 2-1 The Randles Equivalent Circuit of a Secondary Battery

The charge transfer resistance R_1 and double-layer capacitance C_1 are an attempt to linearly represent the reactions nearby the electrodes, as discussed in Section 1.1.2. The voltage across the double-layer capacitance is considered to be the overpotential that determines the current rate. The charge transfer resistance is then a varying resistance that represents the local Butler-Volmer electrode voltage/current relationship. The double-layer capacitance is also not a perfectly linear element, which is sometimes modeled as a constant phase element (CPE) in the literature.

The diffusion RC structure is somewhat inaccurate in the sense that an RC structure really does not describe the diffusion phenomenon. This diffusion process could be modeled as a series string of many RC structures that together approximate the

nonlinear behavior. The task of obtaining equivalent circuit parameters would become tedious as the number of RC structures increases.

A CPE in place of the capacitor is also sometimes found in the literature as a means to describe the diffusion process. But due to the nonlinearity of the CPE, it will be difficult to find its value utilizing linear algebraic techniques. Another possibility is to develop a table of voltage attributed to the diffusion process as a function of current, SOC, time, and temperature. This approach is more limited in the sense that the table is likely to either only work under certain circumstances, or becomes too complicated without any guarantee to work once the aging process starts to manifest itself.

If an RC circuit with a fixed, predetermined order is selected for the equivalent circuit model, the task is to fit the most suitable parameter values as determined by the input (current) and output (RC element voltage) information using the system identification technique. Notice that a difficulty in applying this technique during operation is that there is no direct measurement of the voltage across the RC element since there is no way to measure the open-circuit voltage, v_{ocv}. One way to obtain the open-circuit voltage information is through coulomb counting and a predetermined relationship between v_{ocv} and the Ah remained in the battery. This method depends on information obtained offline and may not be accurate over time as the battery ages. In addition, the thermodynamic nature of the electrochemical process dictates that v_{ocv} is also a function of temperature.

For the battery that is the particular focus in this research, the OPTIMA D34M and its related deep-cycle battery products, the manufacturer provides a graph of the OCV as a function of SOC, as shown in Fig. 2-2.

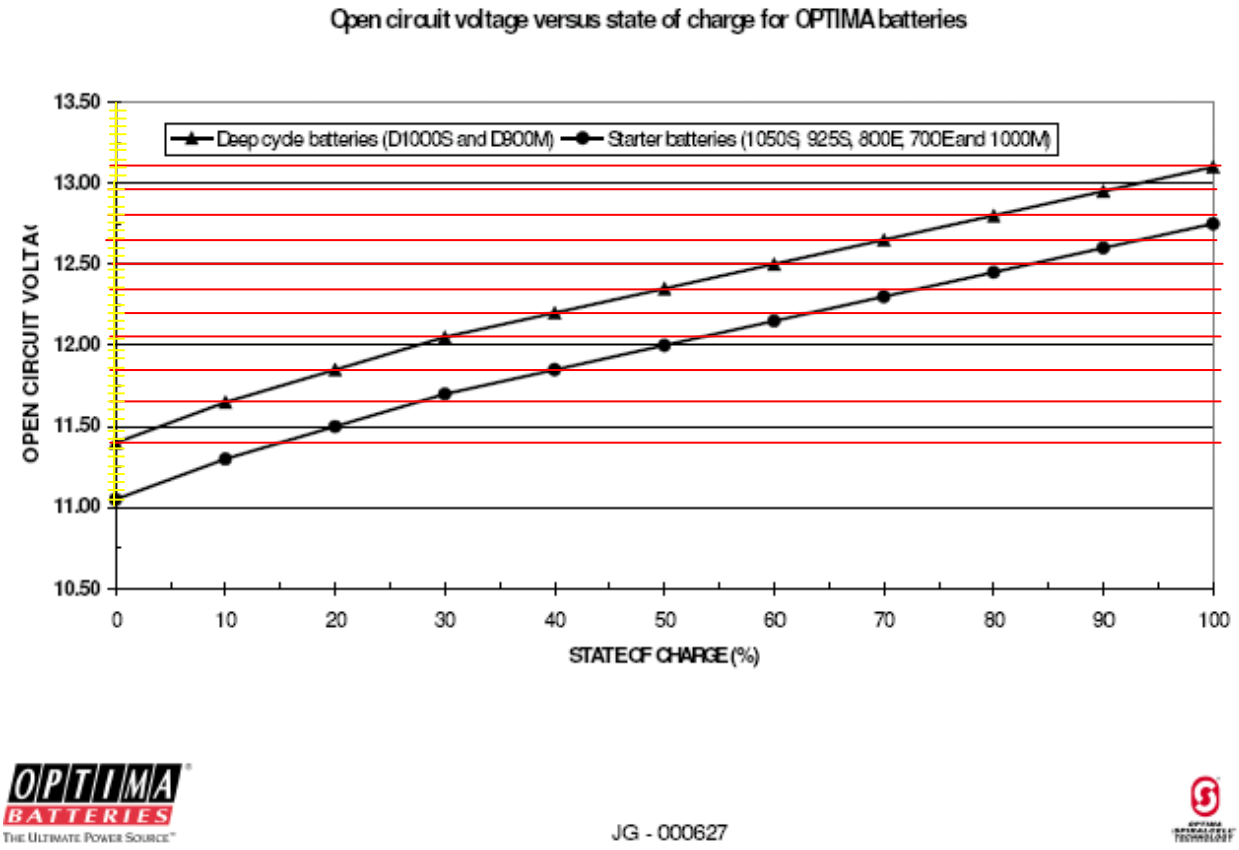

Fig. 2-2 OPTIMA Datasheet for OCV as a Function of SOC for Deep Cycle Batteries

The other method to decouple v_{ocv} from the voltage across the impedance is to use KVL and a low-pass filter to estimate the value of v_{ocv}. More specifically,

$$v_{imp}(k) = \hat{v}_{ocv}(k-1) - v_{batt}(k) \tag{2.1}$$

$$\hat{v}_{ocv}(k) = \text{LPF}\{v_{batt}(k) + \hat{v}_{imp}(k)\} \tag{2.2}$$

In (2.1) and (2.2), v_{imp} is the KVL-deduced impedance voltage ("measurement") across the RC elements and $\hat{v}_{imp}$ is the model-predicted impedance voltage based on measurements of the battery impedance and terminal current. The quantity $\hat{v}_{ocv}$ is the estimated open circuit voltage, and v_{batt} is the measured terminal voltage. The low-pass

filter that determines $\hat{v}_{ocv}$ in (2.2) ensures this quantity does not change much between each time sample, thus validating (2.1) which uses $\hat{v}_{ocv}(k-1)$ for obtaining v_{imp} through KVL.

With the quantities v_{imp}, $\hat{v}_{imp}$ and the battery current, i_{batt}, the system identification technique can now be applied. Essentially, the challenge here is the difficulty of separating the internal voltage components when only terminal information is available. Two methods are suggested that represent two different approaches to v_{ocv} modeling: one is based on coulomb counting and the other is based on low-pass filtered voltage decoupling. The low-pass filter voltage decoupling method has the complication that its cut-off frequency may need to be a function of the current since the average current determines the rate at which v_{ocv} evolves. The two methods do not solve the fundamental challenge of separating the internal voltage components, but they help provide a useful separation between the battery voltage components that make up the terminal voltage.

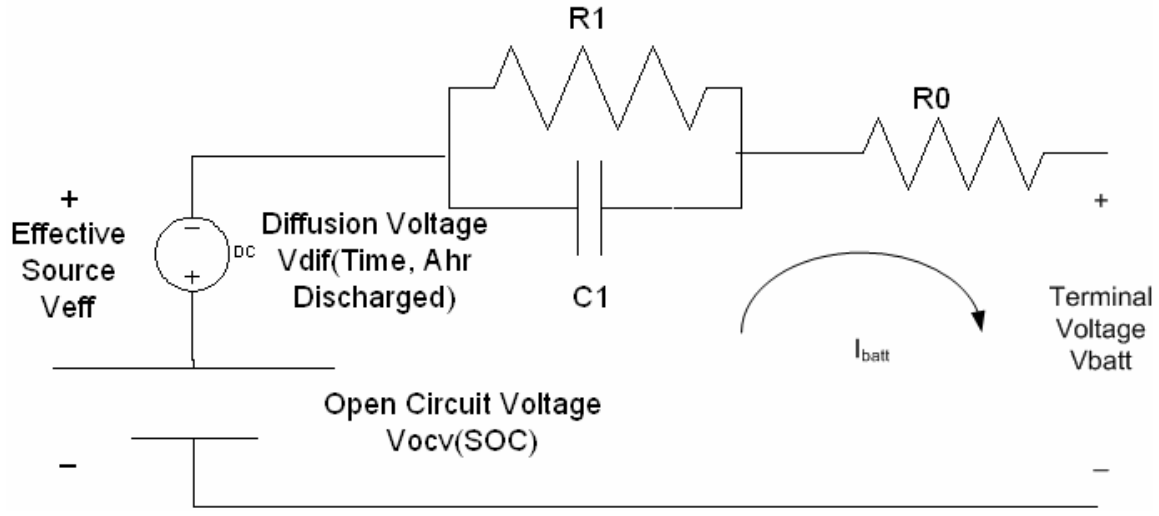

Fig. 2-3 Randles Equivalent Circuit with Diffusion Modeled as a Dependent Voltage Source

In the case of using a stored voltage table to model the diffusion process, the equivalent circuit can be modified as shown in Fig. 2-3. In this figure, the RC structure modeling the diffusion process has been replaced with a look-up table that is obtained offline. In addition, when considering the transient response of the battery, it is possible to lump together the two slowly evolving voltage components, v_{ocv} and v_{dif}, to form an effective voltage source, v_{eff}.

In the following analysis, the diffusion voltage expressed as a function of different variables will be obtained by means of terminal voltage measurements collected two minutes after the current stops, decoupling the effect from the RC structure's time constant. To find the voltage table used for modeling the diffusion process, it was decided to first examine which parameters have the most noticeable effect on the diffusion voltage during EV operation. For EV operation, it is assumed that the operation will start from a full charge state and end at a much depleted state after the trip. Since it is definitely possible that the diffusion effect from the charging process is activated at the time when the user initiates the EV operation, this research proposes to separate the estimated diffusion voltage into two components associated with charging and discharging, respectively. More specifically,

$$\hat{v}_{dif} = \hat{v}_{dif\_discharge} - \hat{v}_{dif\_charge} \tag{2.3}$$

To first demonstrate that it is indeed possible to consider the diffusion voltage as a combination of effects from the two segments of previous output history, the following voltage response graph, Fig. 2-4, was measured experimentally for a lead-acid battery

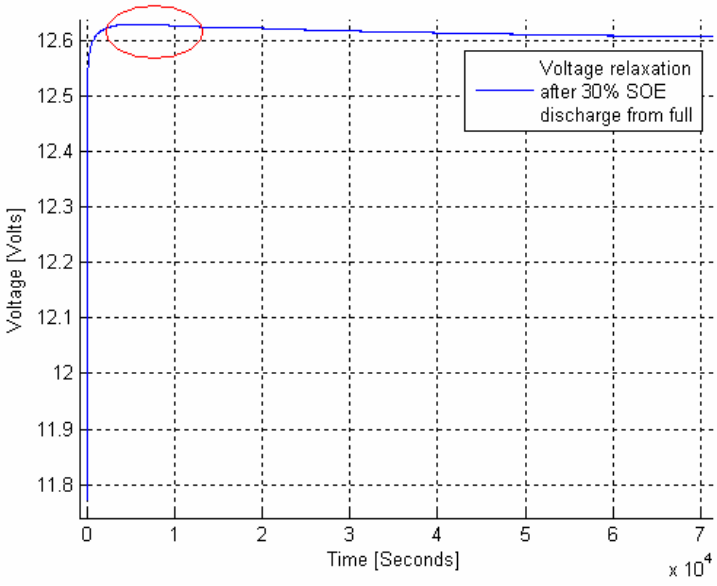

Fig. 2-4 Voltage Relaxation Response Preceded by a 30% SOC discharge from Full Charge State

Powersonic PSH-1280FR during the relaxation period preceded by a 30% discharge from the full charge state.

As seen from the figure, the relaxation from the discharge initially causes the terminal voltage to increase, as expected. However, by approx. three hours, or 10,000 seconds, the effect of the previous full charge manifests itself and causes the terminal voltage to decrease. Thus, the effects of previous battery output history can be considered as accumulative, roughly similar to the superposition principle in linear analysis.

Consider first the diffusion effect from the charging process during EV operation. Since it is likely that the charging algorithm is consistent and all discharge cycles start from the fully charge state, $\hat{v}_{dif\_charge}$ can be considered only as a function of time, starting from the end of charge. Analyzing relaxation voltage two minutes after charge, responses from multiple cycles are plotted and curve-fitted into a function that decreases

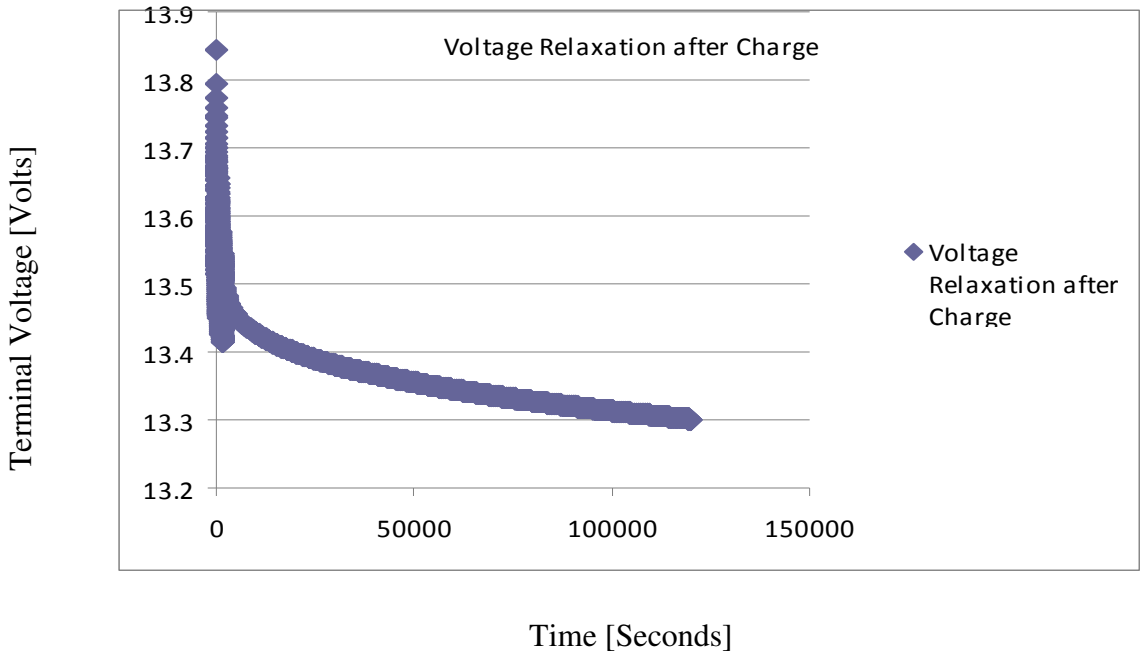

Fig. 2-5 Voltage Relaxation Response After Charge from Multiple Cycles

over time. The battery used is the OPTIMA D34M blue top deep-cycle battery, exactly the same type installed in the WEMPEC Corbin Sparrow as of December 2009.

After curve fitting, the diffusion voltage from the charging process is found to be:

$$\hat{v}_{dif\_charge} = K(-v_{ocv\_charged} - 0.0405 \ln(t) + 13.785) \quad (2.4)$$

where $v_{ocv\_charged}$ is the open-circuit voltage for the charged state from Fig. 2-2 and K is the term that compensates for the discrepancy between each charge process. For $v_{ocv\_charged}$, the value is obtained from a datasheet graph that shows the open-circuit voltage as a function of SOC. The limitations of this approach will be discussed in the next subsection (2.1.2).

Since the assumption is made that the time-decaying property of $\hat{v}_{dif\_charge}$ remains the same despite any observed discrepancy, the value K is used to adjust the difference in the "original charged voltage." The concept is not unlike decays for different initial voltages for the same RC circuit.

For the diffusion voltage from the discharging current, $\hat{v}_{dif\_discharge}$, experiments have shown that the diffusion voltage is largely a function of aggregate amp-hours removed instead of the current profiles. For battery OPTIMA D34M, the following graph (Fig. 2-6) shows the terminal voltage 2 minutes after rest as a function of coulombs removed from the full charged state, for both a constant discharge current 24.6 amps and a discharge EPA driving cycle with the same average current. Please Appendix A for a discussion of the EPA driving cycle.

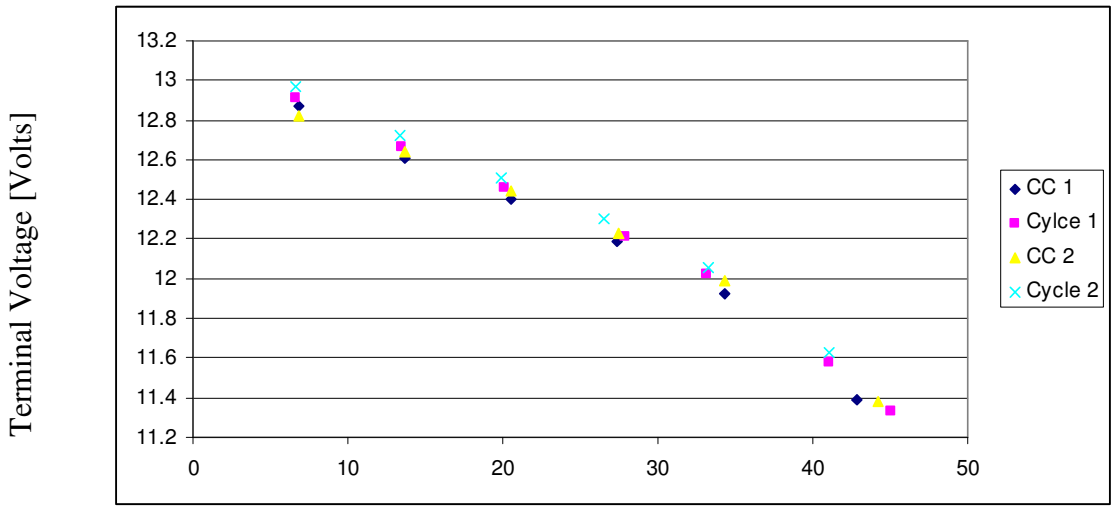

Fig. 2-6 Terminal Voltage after 2 Minutes Rest as a Function of Amp Hours Removed for Both Constant Current Discharge and Current Profile Discharge.

As observed in Fig. 2-6, the terminal rest voltage obtained through constant current is similar to that obtained through a dynamic current profile, with the maximum discrepancy being approx. 150 mV, corresponding to approx. 8% of the difference between 100% and 0% OCV from Fig. 2-2. With the assumption that the two minutes rest period is sufficient to remove all the residual voltage in the electrode/electrolyte

double-layer region while short enough to maintain the bulk diffusion voltage, the voltages observed in Fig. 2-6 are the sum of the diffusion voltage components and v_{ocv}.

Since the maximum battery capacity at the 20 hour rate measured in the lab is 54 Ah, similar to the 55 Ah rating claimed by the datasheet, it is possible to deduce the open-circuit voltage using Fig. 2-2 for each data point in Fig. 2-6 assuming the temperature condition is stable and consistent with the datasheet specifications. From (2.3), data points from Fig. 2-6, and $\hat{v}_{dif\_charge}$ from (2.4) with K=1, the estimated discharge diffusion voltage $\hat{v}_{dif\_discharge}$ as a function of Ah removed can be plotted as:

$$\hat{v}_{dif\_discharge} = v_{ocv} - v_{2min} + \hat{v}_{dif\_charge}(t) \tag{2.5}$$

where v_{ocv} is the open-circuit voltage obtained through coulomb counting from Fig. 2-2 and v_{2min} is obtained from Fig. 2-6. From (2.5) the $\hat{v}_{dif\_discharge}$ can be plotted as:

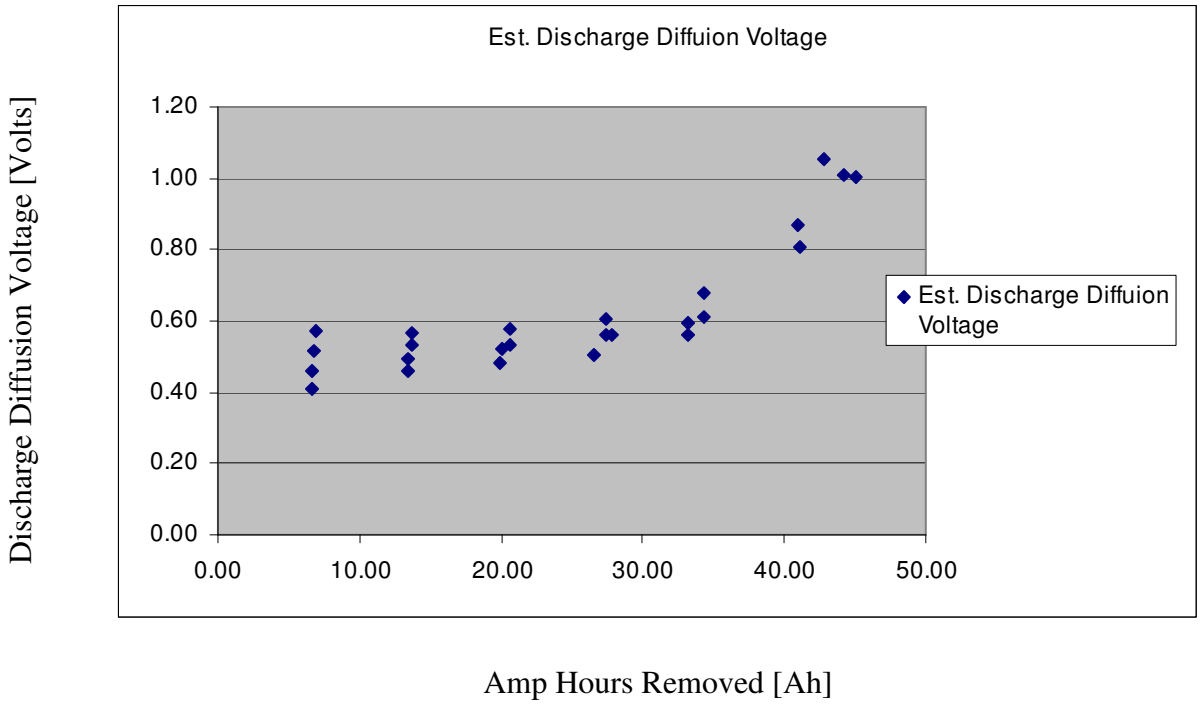

Fig. 2-7 The Estimated Discharge Diffusion Voltage as a Function of Amp Hours Removed

Since it is assumed that before any amp hours are removed $\hat{v}_{dif\_discharge}$ is zero, the curve-fitted function sets the intercept at zero.

$$\hat{V}_{diff\_discharge}(Ah) = -1.576e\text{-}6\ Ah^4 + 1.920e\text{-}4\ Ah^3 - 7.372e\text{-}3\ Ah^2 + 1.095e\text{-}1\ Ah \tag{2.6}$$

2.1.2 Model Theory Discussion

The previous subsection has discussed the formulation of the model and the methodology to populate the model parameters. Here the discussion will focus on the important caveats to the methodology.

The first observation is that the system identification technique requires an appropriate excitation of the components to be identified. The current through the battery needs to have frequency content in the vicinity of the cut-off frequency of the RC structure that we wish to estimate. This means that, if one were to implement the same technique to estimate the battery internal states when charging with a stock charger, an additional carrier signal that excites a broad frequency spectrum might be necessary.

The sampling frequency of the system also plays an important role in the system identification technique. The sampling frequency directly determines the system's pole locations in the discrete domain. As an example, consider the following continuous time domain system:

$$\frac{\text{output}}{\text{input}} = \frac{1}{s^2 + 6s + 5} \tag{2.7}$$

The system can be transformed into the discrete domain for any arbitrary sampling time. Two values have been chosen for comparison, 0.5 seconds and 0.005 seconds, and the results are plotted in Fig. 2-8.

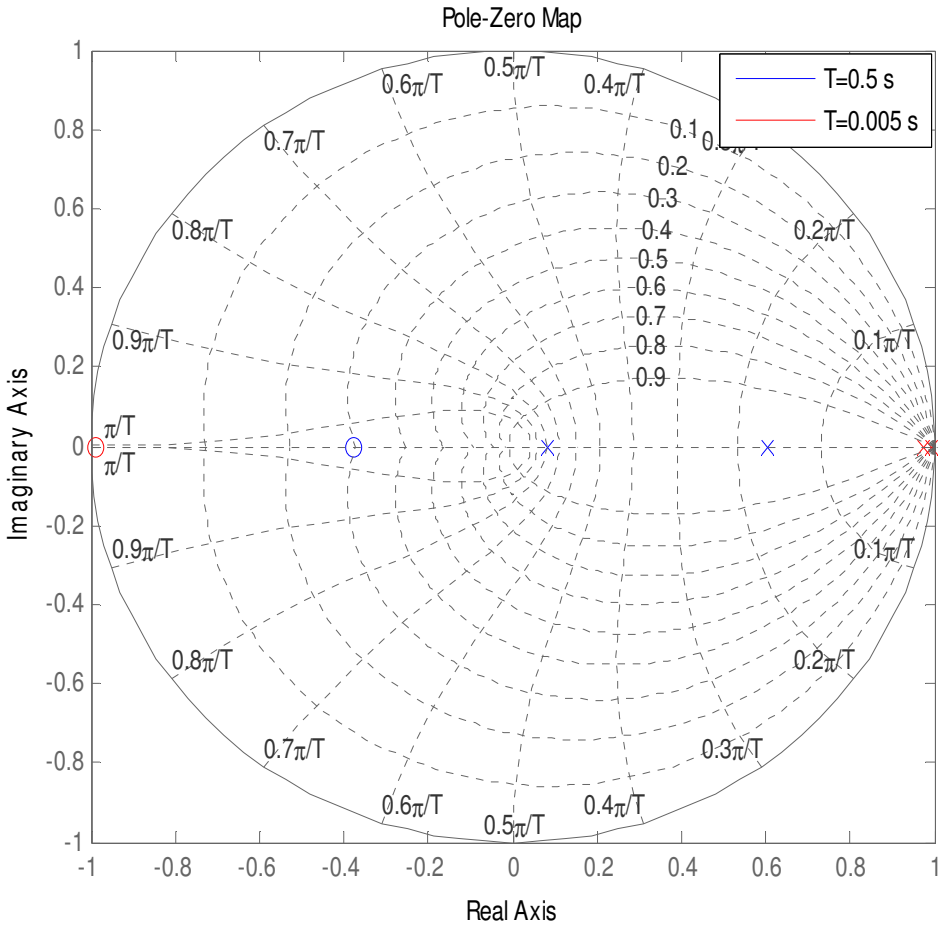

Fig. 2-8 The Pole Zero Map for the System $\frac{1}{s^2 + 6s + 5}$ for Two Sampling Times, 0.5 and 0.005 Seconds

As seen in Fig. 2-8, the fast sampling rate has the tendency to cluster the system poles in the vicnity of the (1,0) point. This tendency is due to the fact that these poles are too slow to appear significantly different from each other to the fast-sampling discrete system. The implication of this constraint is that the sampling time of the system identification model needs to be appropriately chosen for each pole.

Unfortunately, the diffusion process has a much larger time constant compared with the charge transfer/double layer RC. If one were to estimate the diffusion process as an RC structure using the system identification technique, it would be necessary to subsample the signals. However, the subsampling might result in inadequate steps for system identification to converge during one discharge operation, thus making it necessary to provide close initial guess parameters. Adequate steps for convergence do not constitute a problem for a continuously running system such as the HEV application. However, for an application that requires a reset, each cycle may not have the necessary step number to achieve the desired estimation.

When using the KVL deduction method to find the estimated open-circuit voltage $\hat{v}_{ocv}$, the initial parameters picked to start the system identification can influence the solution using the system identification technique. Specifically, reexamination of equations (2.1) and (2.2) will show that the first time (2.2) is executed, the solution to $\hat{v}_{ocv}$ is directly dependent on $\hat{v}_{imp}$, which is a function of initial parameter guesses and the current. This $\hat{v}_{ocv}$ will then influence the KVL-deduced v_{imp} value when (2.1) is executed at the next time sample. Essentially, the system identification technique used here will not have a unique solution but will depend on the initial parameter estimates for the impedance structure and $\hat{v}_{ocv}$. Fortunately, the system is still bound by the voltage and current measurements. Although the algorithm is not mathematically robust, empirical results show that the system will tend to converge to the same solution after some time despite differences in the initial guesses. Fig. 2-9 shows a state block diagram of the online parameter updater.

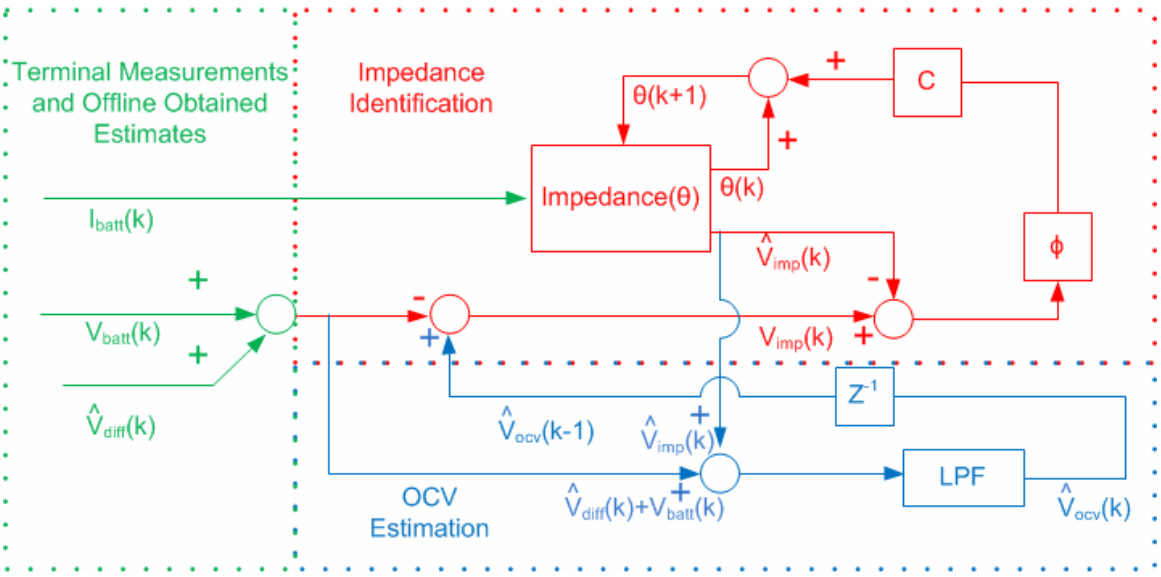

Fig. 2-9 State Block Diagram for the Battery System Identification Parameter Updater

Since the terminal voltage equals the sum of the voltage components in the system model, the proposed method has the following property. If one voltage component, e.g. diffusion voltage v_{dif}, is not estimated correctly, the deviation will influence the other components including v_{imp} and $\hat{v}_{ocv}$. While this linkage property could affect the performance of the SOC estimation based on $\hat{v}_{ocv}$, it does ensure the continuation of estimation despite errors caused by factors such as erroneous initial parameter guesses or a sudden change in operating point. The system can still provide pertinent information based on the relative values of the parameters as they evolve during battery operation.

The charging algorithm used in these experiments is based on the charging algorithm used in the Corbin Sparrow stock charger and the recommended guidelines for the OPTIMA batteries.

Table 2-1 Charging Algorithm Used in Experiments

Mode	Details
Constant Current	25 Amps until 14.7 Volts is reached
Constant Voltage	Maintain at 14.7 Volts until Current Drops below 1 Amp.
Pulse Charge	1.5 Amps for 2 Seconds and 0 Amps for 5 Seconds for 4 Hours. The Pulsed Charging Current is Regulated Such that the Terminal Voltage Never Exceeds 15.7 volts

The charging algorithm listed in Table 2-1 can be inconsistent between cycles in the sense that it is possible to charge a different amount of coulombs to the battery every time. Over a long period of time, it was observed that the Optima battery is charged more fully. Although it was never observed that the 20 hour rate discharge resulted in more amp hours than the datasheet claimed (55 Ah), the experiments did show the battery capacity rose from approx. 46 Ah to 53.9 Ah. One would have to suspect that the charging algorithm is in fact overcharging the battery and possibly causing damage. Even if the aging effect could be ignored, the inconsistency itself means the reference to Fig. 2-2, or any OCV vs. SOC data, is questionable, especially for the offline diffusion voltage estimation. As a result of this overcharge effect, the value of the open-circuit voltage after charging in (2.4) will not be exactly the same for each data set. The charging algorithm inconsistency also makes the initial value estimation for $\hat{v}_{ocv}$ in Fig. 2-9 more challenging, with ramifications discussed above. In this document, however, the open-circuit voltage after charge will be fixed at 13.1 volts as in Fig. 2-2.

Extending the discussion on the consistency of the charging algorithm, the real issue here is the need to look for a reference point at which the monitoring algorithm can reset. This reset point is particularly important for an EV-like application that has a "start" and an "end." In order to get relevant information by comparing monitored data

between different cycles, the ”start” point needs to be consistent. For the traditional coulomb counting method, it is particularly important that the reset point at the start of discharge should be the same. If the full charge state is quite different from one cycle to another, the coulomb counting method naturally fails.

The SOC estimation method proposed in this thesis is less vulnerable to inconsistency of the reset points due to the utilization of the terminal voltage measurements which directly affect the estimated OCV, $\hat{v}_{ocv}$, through KVL. For an application like the HEV, the issue is much less severe since the battery is never fully charged or discharge. As such, the need for a precise reference point does not exist under normal HEV operating condition, as in Wiegman’s studies [9].

Compared with the lack of consistency in the relaxed open circuit-voltage state after charge (200 mV discrepancy after 30 minutes relaxation were often observed), the constant current discharge that is terminated by a set lower voltage limit seems to bring the battery to a more consistent relaxed open-circuit voltage state for every cycle. For most of the experiments that discharge the battery at a fixed current (24.6 amps) and cut off at a fixed voltage (10.5 volts), it was observed that the terminal voltage reaches approx. 11.6 voltage after 30 minute rest, with a distribution in the vicinity of 50 mV.

2.1.3 Parameters Initialization

In order for the system identification method employed in battery online monitoring to maintain consistency, the initial guesses of the parameters need to be obtained from a defined methodology. Since all the current profiles are discharging from the fully charged state, it makes sense to find the approximate battery impedance values in this initial region. A deterministic, least square system identification approach is

suitable for this application. Specifically, consider the first-order impedance structure used to identify the battery impedance:

$$\frac{\hat{v}(z)}{i(z)} = \frac{b_0 + b_1 z^{-1}}{1 + a_1 z^{-1}} \tag{2.8}$$

The difference equation form for (2.8) is thus:

$$\hat{v}(k) = b_0 i(k) + b_1 i(k-1) - a_1 \hat{v}(k-1) \tag{2.9}$$

If we were to write out for the first n terms of the estimated data, (2.9) can be written in the matrix form, replacing $\hat{v}$ with the actual measured data v in the matrix A of (2.10):

$$\begin{vmatrix} \hat{v}(0) \\ \hat{v}(1) \\ . \\ \hat{v}(k) \end{vmatrix} = \begin{vmatrix} i(0) & i(-1) & v(-1) \\ i(1) & i(0) & v(0) \\ . & . & . \\ i(k) & i(k-1) & v(k-1) \end{vmatrix} * \begin{vmatrix} b_0 \\ b_1 \\ a_1 \end{vmatrix} = \hat{v} = Mb \tag{2.10}$$

An error vector can then be formulated as the difference between measured voltage data v and $\hat{v}$. Performing the pseudoinverse on M, the solution for b is then the following:

$$b = (M^T M)^{-1} M^T v \tag{2.11}$$

In (2.11), $(M^T M)$ is invertible as long as the columns of M are linearly independent, which is true for most of the conceivable experimental data. The b vector can be considered as the best fit given M and v for the least square error criterion. Thus if a suitable amount of initial data is used, the impedance of a battery can be estimated using this batch estimation solution.

Due to the lack of battery internal information, it is not possible to perfectly segregate the v_{ocv} and v_{dif} voltage components from each other. One idea is to combine

the two of them as an effective source, v_{eff}. Since the initial range investigated is likely to be limited, it is tolerable to use a constant v_{eff} for the purpose of estimating the initial guesses for R_0, R_1, and C_1. One possible candidate for v_{eff} is the average of the terminal voltage before a load current is applied and the terminal voltage measured at the last time sample within the investigated initial range when no load current is applied. Another likely choice could be the terminal voltage before the load current is applied.

2.2 Experimental Comparison between Coulomb Counting Method and Internal EMF Estimation

With the battery model constructed, the battery model internal EMF estimation is compared with the coulomb counting method based on the data from Fig. 2-2. For the battery model, the case that considers the diffusion voltage and the case that does not will both be investigated. Actual experimental data for the OPTIMA D34M lead-acid batteries is used to perform these model verification tests.

2.2.1 Internal EMF Estimation without the Diffusion Voltage and Coulomb Counting Method

The model without the diffusion voltage essentially combines the v_{ocv} and v_{dif} components in Fig. 2-3 to form an effective voltage source, v_{eff}.

For the coulomb counting method, the points on Fig. 2-2 are curve-fitted in a polynomial to find the datasheet open circuit voltage as a function of SOC.

$$\hat{v}_{ocv\_data} = 0.8703\ SOC^3 - 1.7417\ SOC^2 + 2.5774\ SOC + 11.4 \tag{2.12}$$

The SOC in (2.12) varies from 0 to 1. If the total capacity in the battery can be assumed to be 55 Ah as claimed in the datasheet, the datasheet open-circuit voltage $\hat{v}_{ocv\_data}$ can be estimated using coulomb counting. To determine the validity of the modeling, a comparison between measured and predicted voltage is presented below with a discussion of the calculation of the model voltage prediction.

With the estimated effective voltage $\hat{v}_{eff}(k)$ and internal impedance in the forms of $b_0(k)$, $b_1(k)$, and $a_1(k)$, the model tracking voltage at any sample k can be found along with the measured input current data at k and k-1. This model tracking voltage is more representative of how the model is really performing than using the equation error predicted voltage discussed in 1.6.1. The equation error predicted voltage would have been always close to the measured output by virtue of utilizing previously measured output voltage in its derivation. Table 2-2 documents the parameters used in the model.

Table 2-2 Parameter Values for the Model without Diffusion Component

Initial R_0	0.0038 [Ohms]
Initial R_1	0.0068 [Ohms]
Initial C_1	1097 [Farads]
Initial $\hat{v}_{eff}$	v_{batt} = 13.47 [V] at t = 0
$\hat{v}_{eff}$ LPF Cut Off Frequency	0.1 [Hz]
Updater Gain c	1e-5 [/]
Forgetting Factor	$\frac{1}{0.99998}$ [per sample]
Pole Update Correction Factor	100 [/]
Rejection Factor	10% [/]
Minimum Update Threshold	2 [A]

Several items in Table 2-2 require explanations before the results can be presented. The initial parameters R_0, R_1, and C_1 are obtained by means of an offline estimation discussed in Section 2.1.3 with the data for the initial 200 seconds. For the

model without diffusion component, the initial value for $\hat{v}_{eff}$ is chosen to be the terminal voltage v_{batt} when the profile starts with the current still at zero. The $\hat{v}_{eff}$ LPF cut-off frequency is chosen to be 0.1 Hz; as discussed in 2.1.1, this value effectively forms a model that rejects any voltage change above 0.1 Hz as being unassociated with $\hat{v}_{eff}$. The forgetting factor is multiplied by the updater gain c each sample time, thereby giving the later information more weight based on the expectation of parameter evolution, as discussed in Section 1.6.1. The pole update correction factor is meant to force a quicker update of the pole in the impedance structure. Instead of strictly following Eq. (2.13) as in Section 1.6.1, the gain in the parameter a_1 is increased by the pole update correction factor (PUCF) as in Eq. (2.15). The reason for this need of a faster speed is that the electrode voltage vs. current relationship is not linear. The performance of the model will thus improve if the pole, i.e. the electrode RC model, updates more quickly.

$$\hat{\theta}(k) = \hat{\theta}(k-1) + c\Phi^{T}(k)[\, v_{imp}(k) - \hat{v}_{imp}(k)] \tag{2.14}$$

$$\begin{bmatrix} \hat{b}_0(k) \\ \hat{b}_1(k) \\ \hat{a}_1(k) \end{bmatrix} = \begin{bmatrix} \hat{b}_0(k-1) \\ \hat{b}_1(k-1) \\ \hat{a}_1(k-1) \end{bmatrix} + \begin{bmatrix} c & 0 & 0 \\ 0 & c & 0 \\ 0 & 0 & PUCF \times c \end{bmatrix} \phi^{T}(k)[v_{imp}(k) - \hat{v}_{imp}(k)] \tag{2.15}$$

The rejection factor has to do with the fact that Eq. (2.15) is not guaranteed to generate a sensible solution once the parameters in b_0, b_1, a_1 are converted back to R_0, R_1, and C_1. The adopted approach to ensure this stability is to verify that the estimated value of R_1 is always within a certain percentage, rejection factor [%], of its previous value. If the criterion is violated, the newly obtained parameters are dropped and the previous sample parameters are retained.

Lastly, the minimum update threshold of 2 A ensures that the system only updates the parameters when an excitation is active, with the assumption that the driving cycle will not see a constant load when the load current is higher than the minimum update threshold.

With the parameter settings explained, the results can now be presented. Fig. 2-10 shows measured voltage vs. model estimated voltage without the diffusion component for one EPA driving cycle sampled at 10 Hz. The test battery is the Optima D34M, rated at 12 V and 55 Ah; the test was performed at room temperature in the WEMPEC laboratory using an electronic load to emulate the EPA driving cycle. More information about the experimental equipment used to collect this data is presented in Appendix B of this thesis. Fig. 2-11 is a zoomed-in plot for Fig. 2-10. Fig. 2-12 shows the model prediction errors.

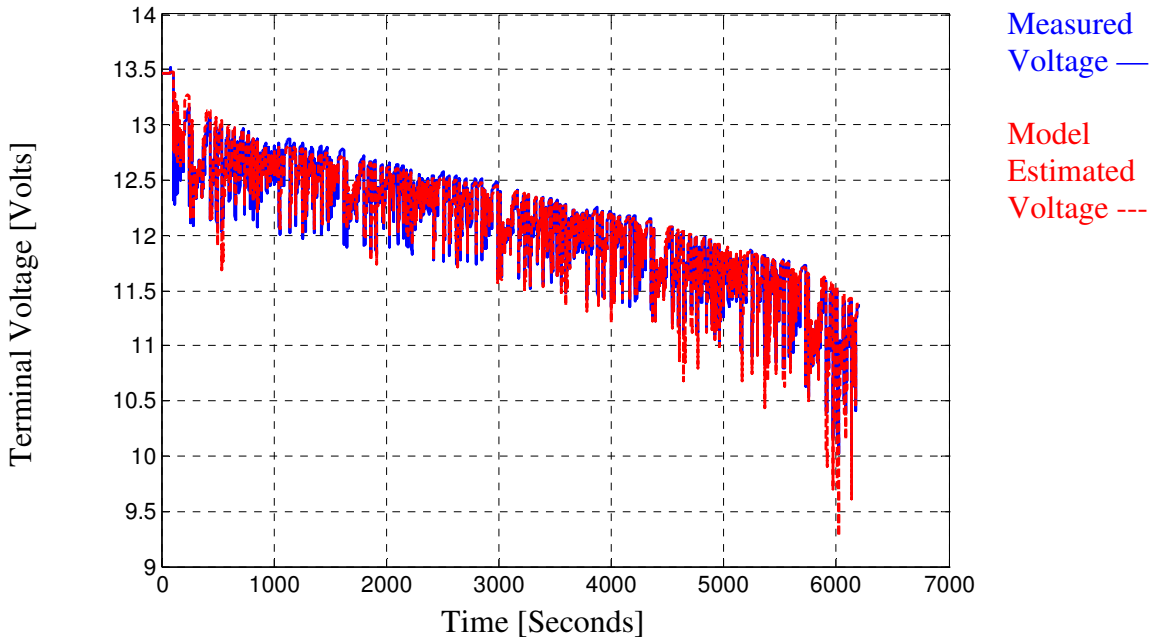

Fig. 2-10 Measured Voltage vs. Model Estimated Voltage without Diffusion Component for EPA Cycle

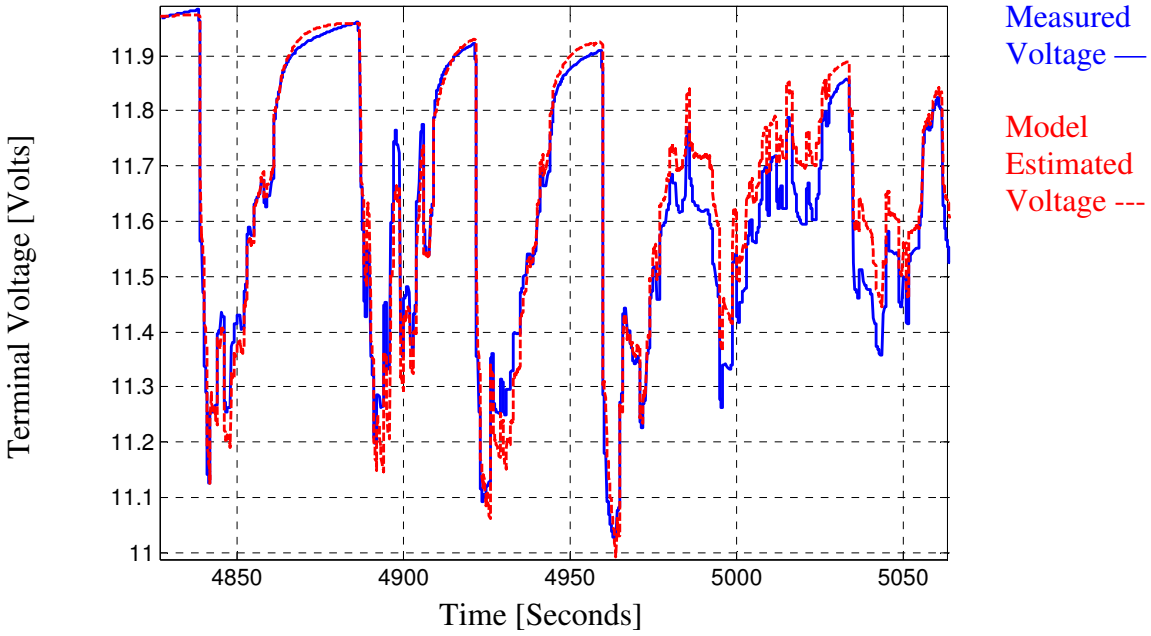

Fig. 2-11 Zoomed in Measured Voltage vs. Model Estimated Voltage without Diffusion Component for EPA Cycle

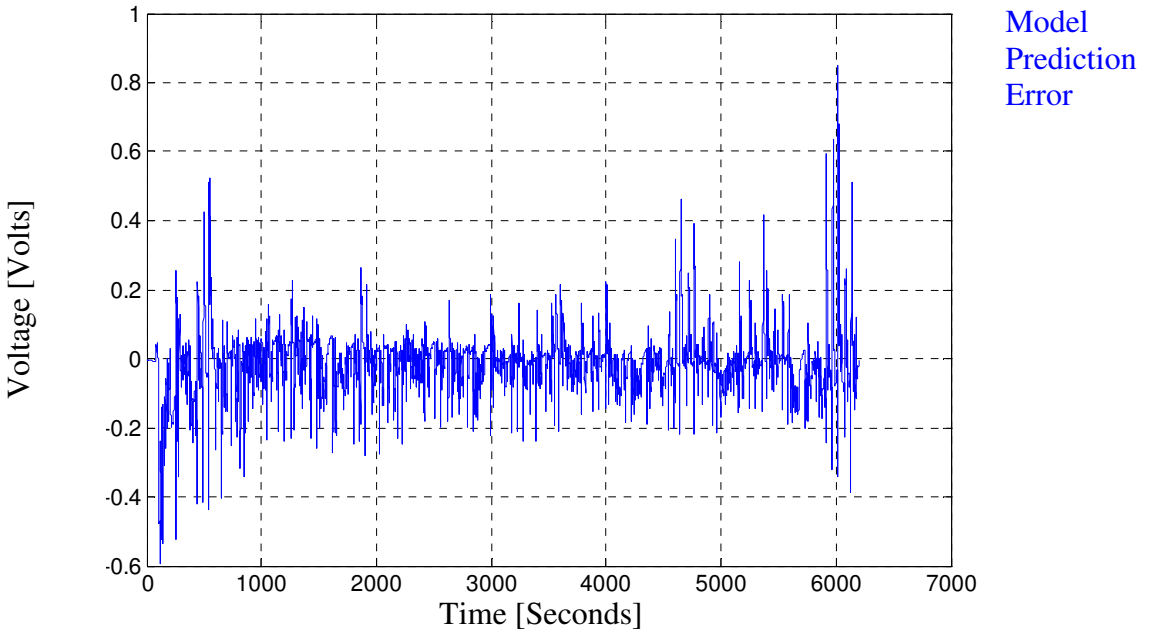

Fig. 2-12 Model Prediction Error for the Model without Diffusion Component for EPA Cycle

In terms of the terminal voltage tracking performance, the average voltage error in each time sample is 0.0837 volts, or about 5 percent of the range between 100% and 0%

SOC in Fig. 2-2. It can also be observed in Fig. 2-12 that the error is continuously reducing throughout the estimation process, as expected given the recursive nature of the updater. From Fig. 2-11, it can be seen that the model captures much of the dynamics experienced by the battery. However, certain nonlinear transient effects are definitely still missing from the model. One feature worth noting is that the error increases at the end of the discharge cycle in Fig. 2-12. This is due to the accelerated increase of the fast dynamic impedance R_0 at the end of discharge cycle.

For the EPA driving cycle sampled at 10 Hz, the following graph in Fig. 2-13 is the comparison between datasheet $\hat{v}_{ocv}$ based on (2.12) and the model estimated $\hat{v}_{eff}$.

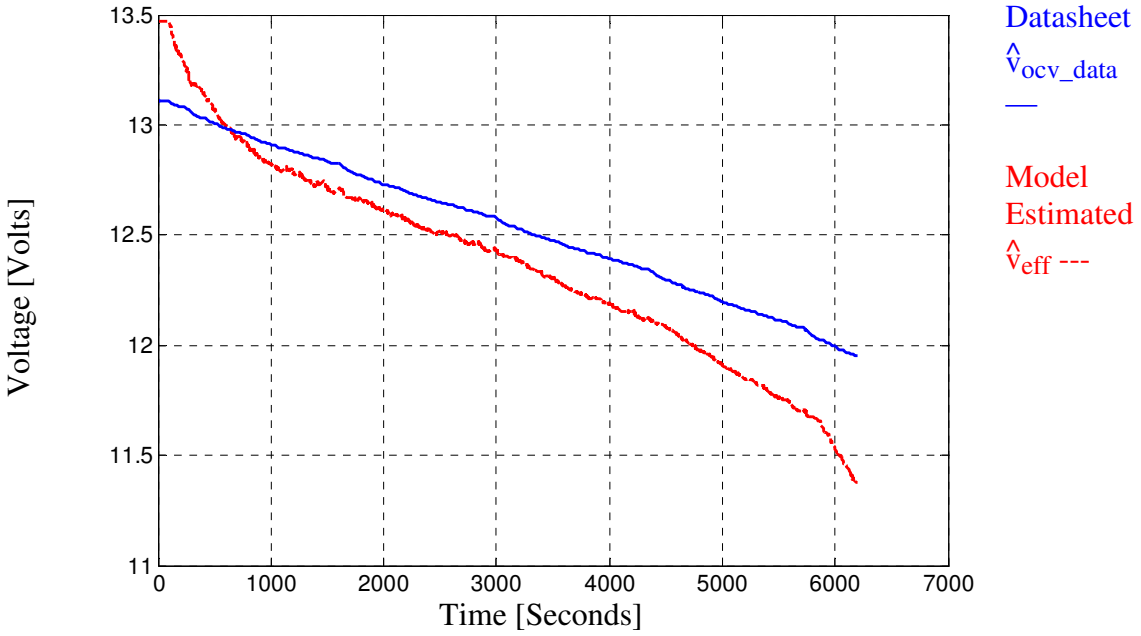

Fig. 2-13 Datasheet-based $\hat{v}_{ocv\_data}$ vs. Model Estimated $\hat{v}_{eff}$ for EPA Cycle

From Fig. 2-13, it can be observed that $\hat{v}_{eff}$ is higher than $\hat{v}_{ocv\_data}$ initially but drops below 1000 seconds after the discharge starts. This phenomenon is expected because $\hat{v}_{eff}$ is an estimate of the combination of v_{ocv} and v_{dif}.

$$v_{eff} = v_{ocv} + (v_{dif\_charge} - v_{dif\_discharge}) \quad (2.16)$$

As the effect of $v_{dif\_discharge}$ gradually dominates that of v_{dif_charge} during the discharge cycle, it influences v_{eff} by making v_{eff} lower than corresponding value of v_{ocv}.

While Fig. 2-13 demonstrates the possibility of using this estimated effective voltage $\hat{v}_{eff}$ as an indicator of SOC, a few issues remain. For example, this indicator would probably overestimate the SOC in the beginning and underestimate it at the end. The behavior of the indicator, especially in the beginning of discharge, would also be hard to compare between cycles since the charging algorithm is not always consistent. However, if one were to only require a rough SOC indicator that automatically takes the terminal voltage into account in order to reduce its vulnerability to the lack of reset point that is characteristic of the pure coulomb counting method, this estimated effective voltage $\hat{v}_{eff}$ will likely do a reasonable job.

Before the discussion moves on to the model with diffusion voltage component, the performance of the model without the diffusion voltage component will be examined for a 0.1 Hz square wave current discharge with the same average current as the EPA driving cycle. The model parameter settings are exactly the same as in Table 2-2, but the initial parameter estimates are as adjusted to be $R_0 = 0.0059$ Ohms, $R_1 = 0.0123$ Ohms, and $C_1 = 724$ Farads using the same initial parameter estimation algorithm as before. The results of this modeling exercise are plotted in Figs. 2-14 to 2-16.

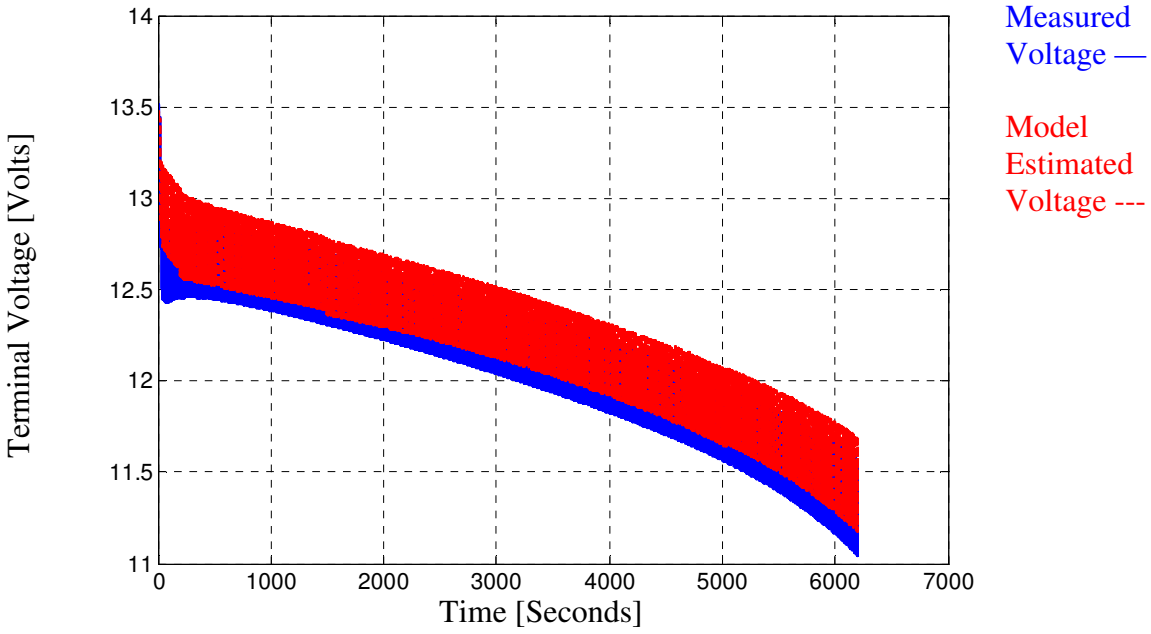

Fig. 2-14 Measured Voltage vs. Model Estimated Voltage without Diffusion Component for Square Wave Discharge

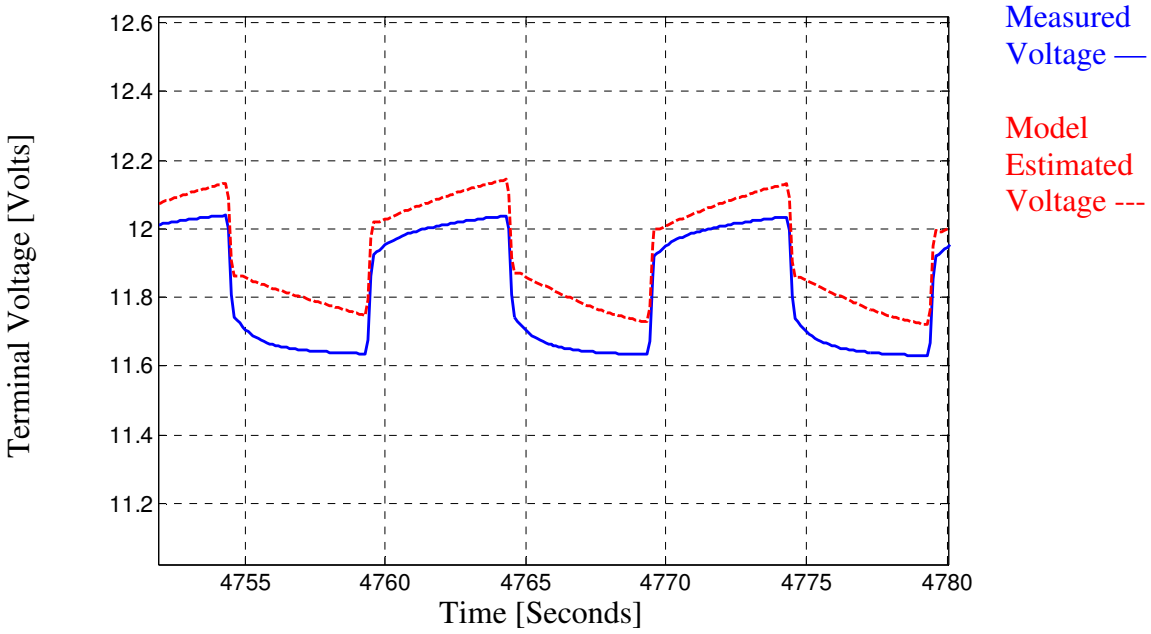

Fig. 2-15 Zoomed in Measured Voltage vs. Model Estimated Voltage without Diffusion Component for Square Wave Discharge

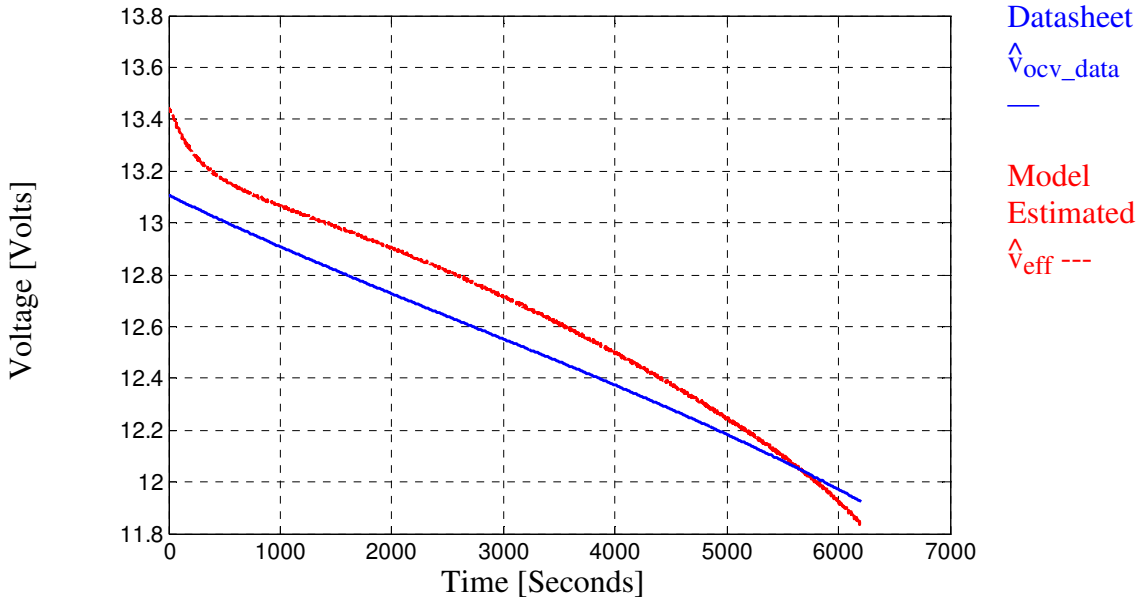

Fig. 2-16 Datasheet-based $\hat{v}_{ocv\_data}$ vs. Model Estimated $\hat{v}_{eff}$ for a Square Wave Discharge

The tracking performance as measured by the average error per sample is 0.1089 V, worse than the 0.0837 V in the previous EPA cycle discharge profile. This poorer performance is perhaps due to the fact that the linear parameters of the battery oscillate along with the square wave, causing a much worse convergence condition. The initial parameter estimation algorithm is perhaps not getting close enough to the ideal starting point, aggravating the convergence issue.

In Fig. 2-14, the measured voltage shows a dip and recovery in the first part of the discharge. This phenomenon is common among the lead-acid batteries and is referred to as "coup de fouet [51]." The phenomenon is definitely nonlinear and is not properly taken into account by the linear model used in the analysis. As discussed above, any under-modeled voltage in one component will appear in other parts due to the KVL constraint. This may have caused changes in the evolution of $\hat{v}_{eff}$. Indeed, it is observed

in Fig. 2-16 that $\hat{v}_{eff}$ exhibits a change in its second derivative corresponding to the nonlinear region in Fig. 2-14.

2.2.2 Internal EMF Estimation with the Diffusion Voltage and Coulomb Counting Method

The model with the diffusion voltage model as discussed in Section 2.1.1 is now compared with the coulomb counting method. The parameter values for this version of the model including the diffusion voltage are presented in Table 2-3 below.

Table 2-3 Parameter Setting for the Model with Diffusion Component

Initial R_0	0.0038 [Ohms]
Initial R_1	0.0068 [Ohms]
Initial C_1	1097 [Farads]
Initial $\hat{v}_{eff}$	v_{batt} = 13.47 [V] at t = 0
$\hat{v}_{eff}$ LPF Cut Off Frequency	0.1 [Hz]
Updater Gain c	1e-5 [/]
Forgetting Factor	$\frac{1}{0.99998}$ [per sample]
Pole Update Correction Factor	100 [/]
Rejection Factor	10% [/]
Minimum Update Threshold	2 [A]

The performance of the altered model with the diffusion voltage for the EPA driving cycle is demonstrated in the following figures, Figs. 2-17 to 2-20.

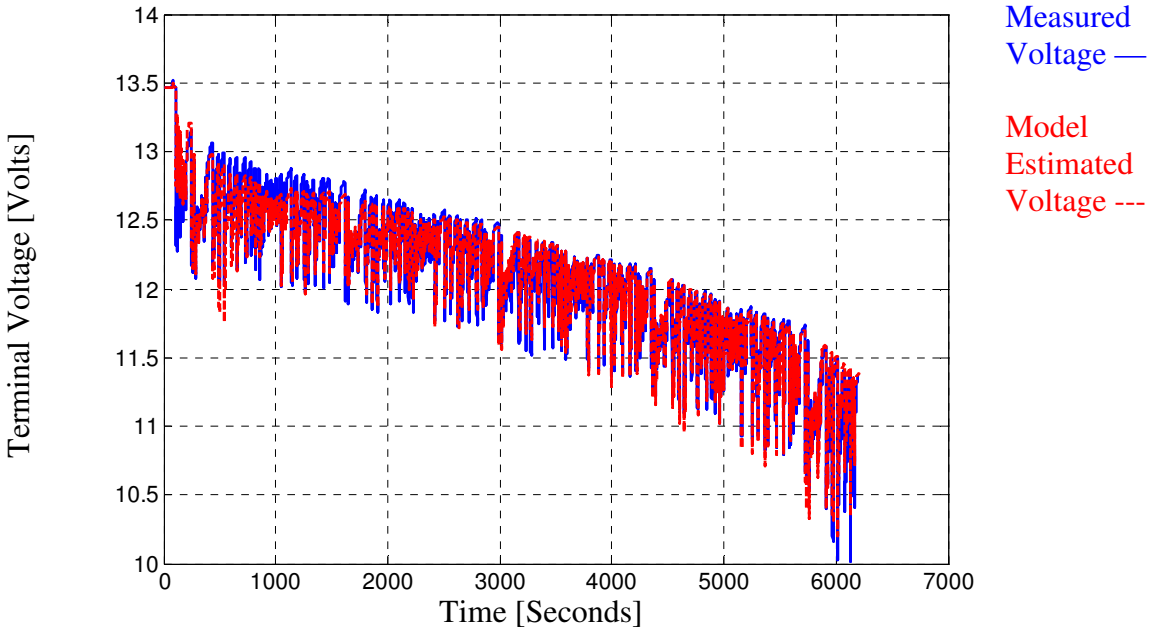

Fig. 2-17 Measured Voltage vs. Model Estimated Voltage with Diffusion Component for EPA Cycle

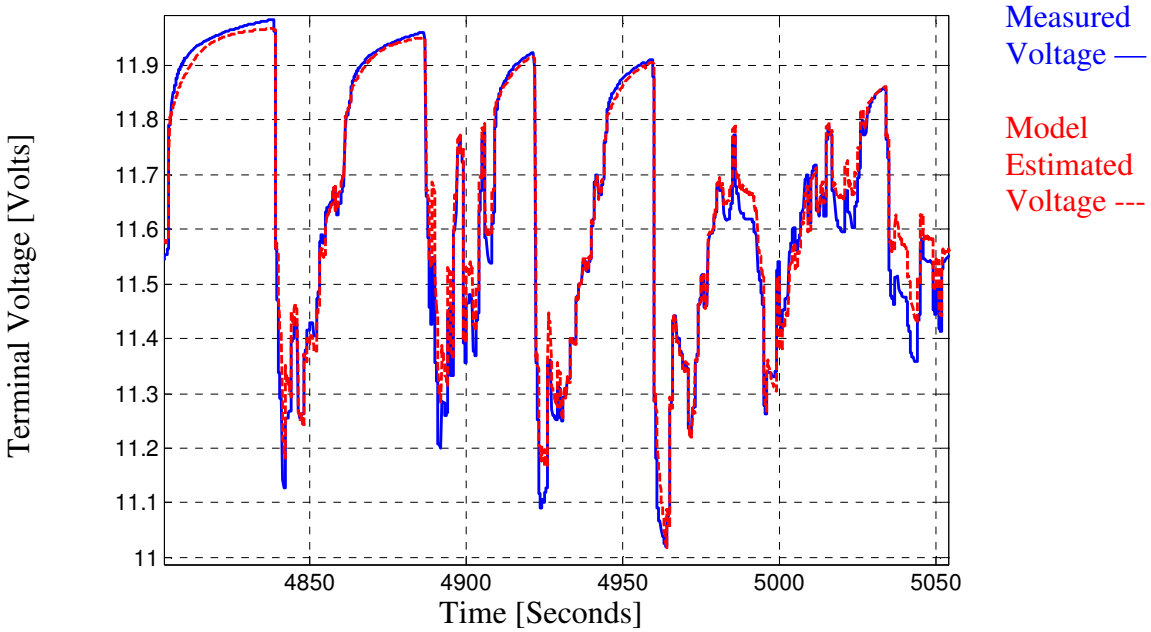

Fig. 2-18 Zoomed in Measured Voltage vs. Model Estimated Voltage with Diffusion Component for EPA Cycle

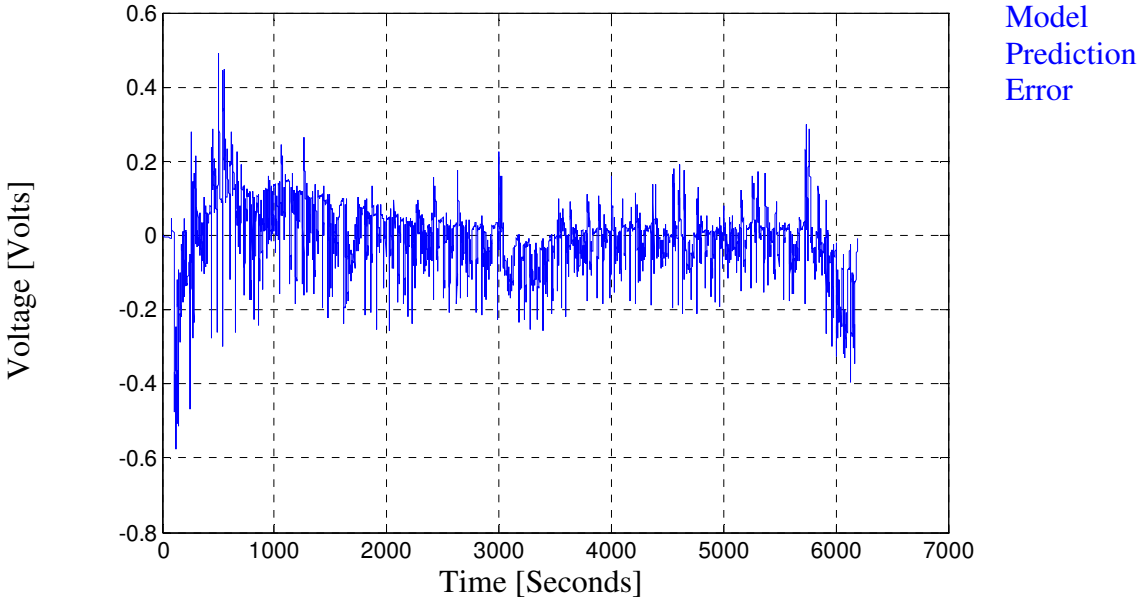

Fig. 2-19 Model Prediction Error for the Model with Diffusion Component for EPA Cycle

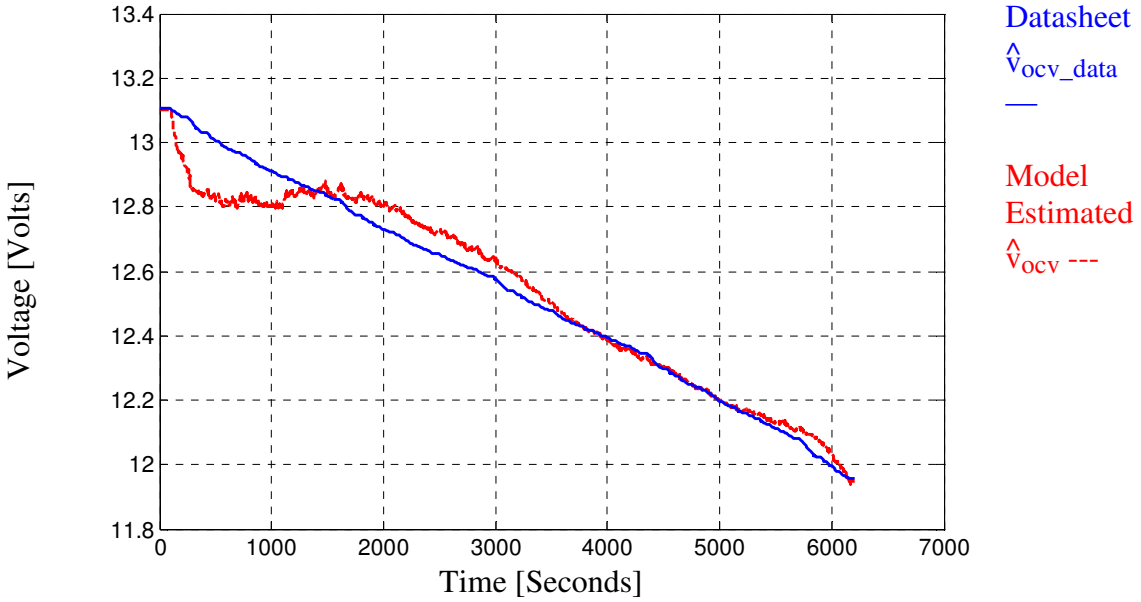

Fig. 2-20 Datasheet-based $\hat{v}_{ocv\_data}$ vs. Model Estimated $\hat{v}_{ocv}$ for EPA Cycle

As in the previous case, the model prediction error is illustrated in Fig. 2-19. While it is almost impossible to tell the difference between the performance of the two models by comparing Fig. 2-10 and Fig. 2-17, the prediction error in Fig. 2-12 and Fig. 2-19 show clear differences. Both Fig. 2-12 and Fig. 2-19 show a similar pattern of large error earlier on, narrowing in the middle, and widening again at the end of discharge.

However, the trend in the middle of Fig. 2-19 shows more curvature, an artifact from the offline diffusion model. The widening at the end is again attributed to the fast increase of R_0 at that part of the discharge.

The average error per time sample is 0.0834 V, slightly smaller than the 0.0837 V for the case with no diffusion component modeled. However, this similarity should not cause any confusion about the structural differences in the two models; they merely happened to have similar values of the least square error. The explanation for the small improvement could be that the evolution of the effective voltage in the model without diffusion voltage relies only on the low-pass-filtered KVL equation, whereas the model with diffusion voltage attempts, however inaccurately, to model the voltage evolution more closely.

With the starting estimated open-circuit voltage $\hat{v}_{ocv}$ chosen to be 13.1 volts in accordance with Fig. 2-2, it can be seen that $\hat{v}_{ocv}$ tracks relatively close to the datasheet open-circuit voltage $\hat{v}_{ocv\_data}$. In Fig. 2-20, the initial part of the operation shows the movement of $\hat{v}_{ocv}$ as it initial diverges from the datasheet open-circuit voltage before eventually converging after approx. 1000 seconds. The explanations can be many, including an error in the initial value for $\hat{v}_{ocv}$, RC circuit model error, and the time dependent $\hat{v}_{dif\_charge}$ being modeled poorly. In addition, the nonlinear coup de fouet phenomenon in this region could have also had some effect on the modeling accuracy.

In Fig. 2-20, $\hat{v}_{ocv}$ and $\hat{v}_{ocv\_data}$ converge quite closely near the end of the discharge cycle. This result is obviously desirable. We could argue that, at least for this particular current profile, the internal EMF estimation method has a performance close to

the coulomb counting method, with the important understanding that the proposed method is less susceptible to the lack of reset point. The proposed method with diffusion modeled offline thus appears to offer a promising way to determine SOC online. The fact that the variation of $\hat{v}_{ocv}$ is not monotonic near the beginning of the discharge cycle represents a topic for future investigation since close convergence is desired throughout the discharge cycle.

2.3 Summary

This chapter has discussed all of the major components of the Randles equivalent circuit model. Two variants of the equivalent circuit, with diffusion and without diffusion, are compared in performance. The diffusion voltage, being a highly nonlinear phenomenon, is modeled as two components $\hat{v}_{dif\_charge}(t)$ and $\hat{v}_{dif\_discharge}(Ah)$ based on the likely operating conditions that an EV application would encounter. It is found that the performance of the proposed model for estimating SOC based on the estimated effective source/open-circuit voltage can be desirable compared with the coulomb counting method. In particular, the estimated effective source/open-circuit voltage method has the advantage of using the terminal voltage information, making it less prone to integrated current sensor error. The accuracy of model tracking voltage for both variants has been checked with actual measured terminal voltage data.

Chapter 3

Model-Based Battery Power Capability Prediction

In this chapter, the use of the developed model for short-term power capability prediction will be discussed. In the discussion on the developed model's suitability for short-term power capability, another modeling approach based on frequency spectral separation utilized in [9] will be compared with the developed model. The focus will then shift to the performance of the developed model in terms of short-term power capability prediction. The prospect of using the developed model for long-term power capability prediction is also considered in the chapter.

3.1 System Identification in the Developed Model

Here modeling and system identification discussed in Section 1.6 will be formulated for the developed model. The battery equivalent circuit model in Fig. 2-3 is shown again here in Fig. 3-1 for easy reference during this discussion.

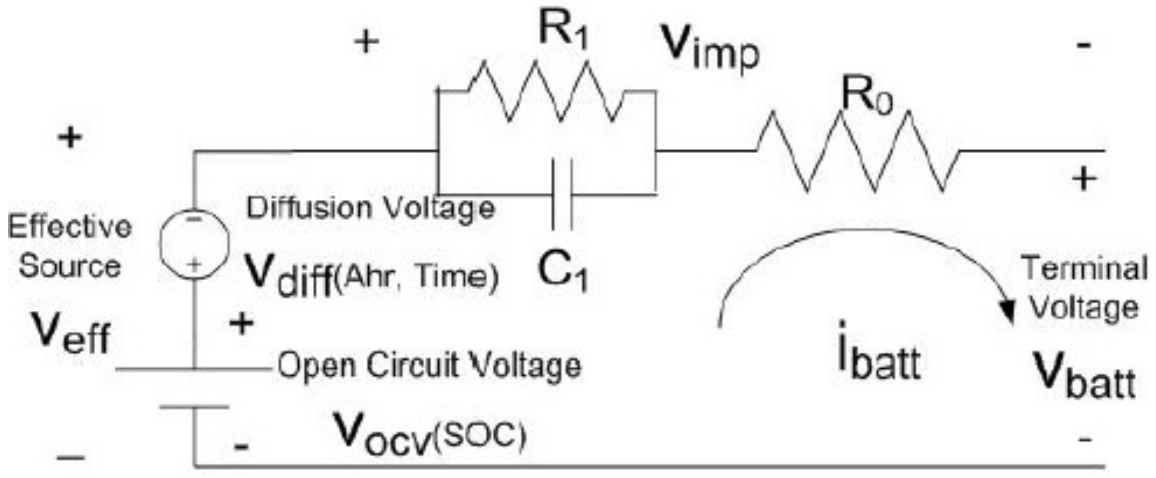

Fig. 3-1 Randles Equivalent Circuit with Diffusion Modeled as a Dependent Voltage Source

Reexamining the RC structure in the model, one can see that the impedance structure is assumed to be a first-order system. By the forward method discussed in Section 1.6.2, the parameters in the z-domain transfer function are expressed in terms of R_0, R_1, and C_1 using the following relationships in Table 3-1. The variable T is the sampled time.

Table 3-1 Z-Domain Parameters as a Function of Time-Domain Parameters for the R-RC Model Structure

Z-Domain Parameters	Time-Domain Composition
b_0	R_0
b_1	$-R_0 + \frac{T(R_0+R_1)}{R_1C_1}$
a_1	$-1 + \frac{T}{R_1C_1}$

Likewise, the time domain parameters can be expressed in terms of the z-domain parameters as shown in Table 3-2.

Table 3-2 Time-Domain Parameters as a Function of Z-Domain Parameters for the R-RC Model Structure

Time-Domain Parameters	Z-Domain Composition
R_0	b_0
R_1	$\frac{-(-b_1 + b_0 a_1)}{a_1 + 1}$
C_1	$\frac{-T}{(-b_1 + b_0 a_1)}$

Examining Table 3-1 and Table 3-2, it is clear that the Z-domain parameters, with the exception of b_0, have no simple linear relationships with the time domain parameters. The complicated transformation laws can cause issues for the developed model if the user's goal is to keep track of the time domain parameters at all times. Specifically, since system identification is merely a numerical technique, it is conceivable that at some time instants, the discrete parameters might transform into unrealistic time domain parameters, such as a negative resistance. From the discussion in Section 1.6.1 and adapted for the first-order system in the model, the z-domain parameter updater relationship is shown here.

$$\begin{bmatrix} b_0(k) \\ b_1(k) \\ a_1(k) \end{bmatrix} = \begin{bmatrix} b_0(k-1) \\ b_1(k-1) \\ a_1(k-1) \end{bmatrix} + \begin{bmatrix} c & 0 & 0 \\ 0 & c & 0 \\ 0 & 0 & c \end{bmatrix} \phi^{T}(k)[V_{out}(k) - \hat{V}_{out}(k)] \tag{3.1}$$

Notice that the updater's diagonal matrix in (3.1) is actually a Jacobian matrix of derivatives. Ideally, the iterative solving techniques such as the Newton-Raphson method will have access to the physics-based Jacobian matrix as the updater. However, as no linear relationships with the time domain quantities exist for the z-domain parameters, the updater matrix is just a diagonal matrix. This lack of physics-based Jacobian matrix inevitably slows down the convergence; it also increases the possibility

of the updated z-domain parameters being detached from physical reality when transformed back to the time domain. Specifically, for the EPA driving cycle, Fig. 3-2 shows the evolution of R_1 value in blue for the model without the diffusion component.

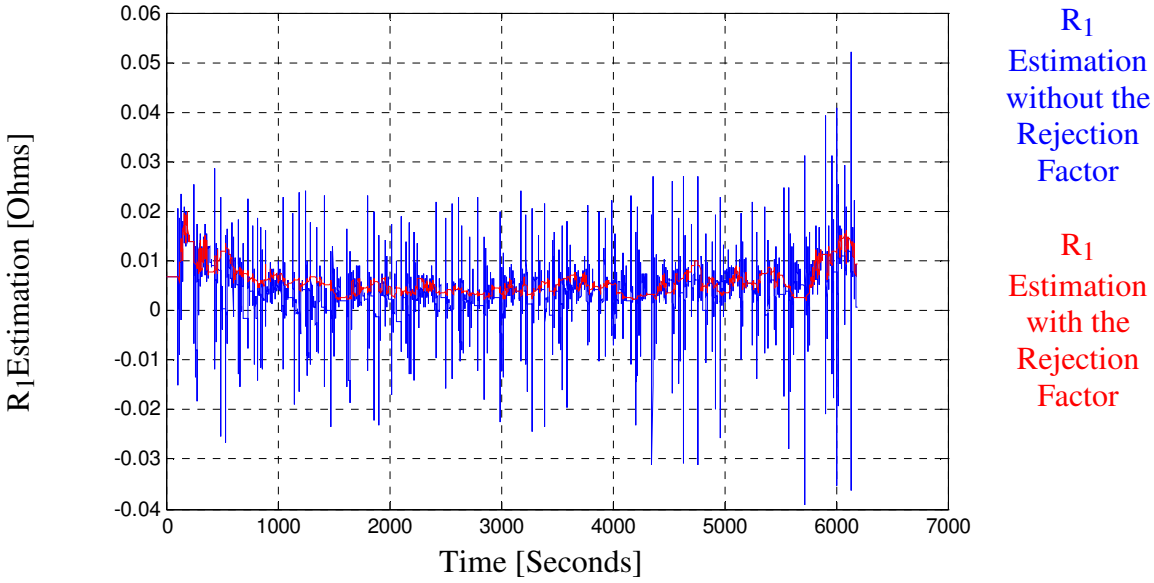

Fig. 3-2 R_1 Estimation without and with the Rejection Factor for the EPA Driving Cycle

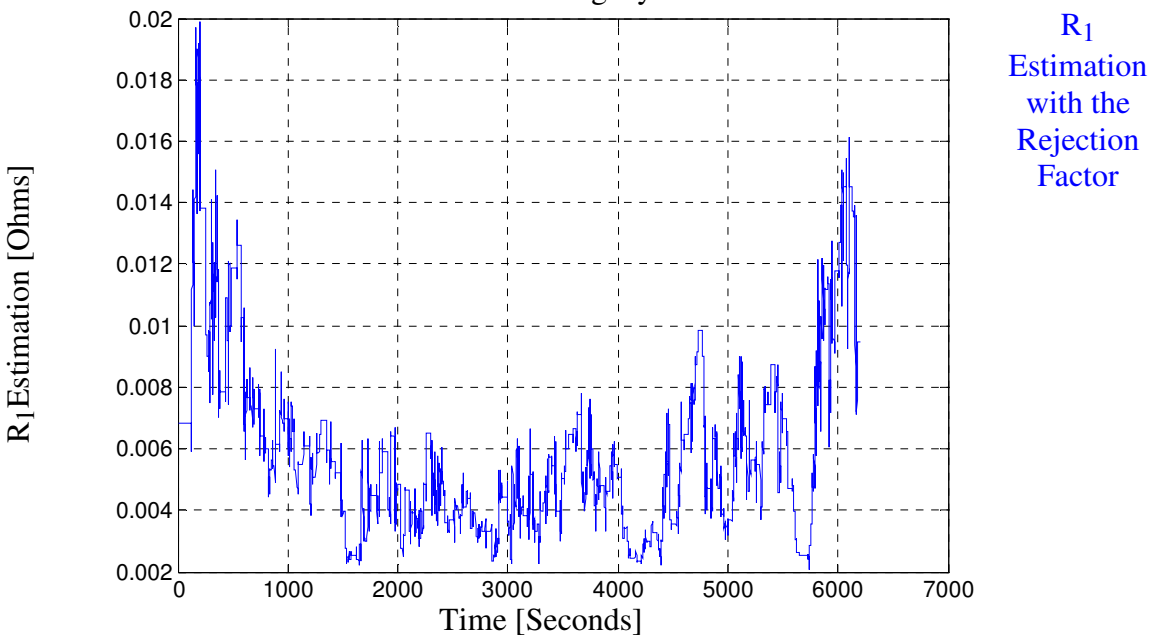

Fig. 3-3 R_1 Estimation with the Rejection Factor for the EPA Driving Cycle

The rejection factor discussed in Section 2.2.1 is tuned to zero (i.e. turned off) to demonstrate the blue curve in Fig. 3-2, while the red curve is for comparison when the rejection factor is tuned at 10%. Fig. 3-3 zooms in for the case for the rejection factor at 10%.

As can be seen in Fig. 3-2, without the rejection factor, the estimated value of R_1 does not stay in the range where we would expect it to be, i.e. above zero. It is also interesting to note that the average model prediction error per sample with the rejection factor turned on is 0.0837 V which is greater than the model with the rejection factor turned off, 0.0672 V. The numerical method attempts to minimize the least square error without paying attention to the physical reality, while the penalty for applying reality constraints is the sacrifice of the least square error value.

In addition to the effect of the lack of physics-based Jacobian matrix, the transformation laws listed in Table 3-1 and Table 3-2 are also informative in pointing out another reason for the wild oscillation in R_1 estimation.

The typical value for the first-order time constant for the OPTIMA battery is in the range of seconds, e.g 5 seconds. This means the time constant R_1C_1 is much greater than the sampled time, 0.1 seconds in this case. The formula for b_1 in Table 3-1will then typically yield a value negative in sign but slightly smaller in magnitude than b_0. In the updating process, it is very conceivable that the magnitude of b_1 can actually exceed that of b_0 at some time instants and cause the time domain parameters to behave wildly.

Four potential remedies have been considered. One is to decrease the sampling frequency so that b_1 does not easily overtake b_0 in magnitude. However, the decrease in sampling frequency can only be implemented to a limited extent before the steps required

for convergence become inadequate. There is also the issue of requiring a sampling frequency that is fast enough to model the fast dynamic reaction.

The second remedy modifies the regressor in (3.1) and replaces the coefficients with more physically connected values. In (3.1), the regressor is based on the discrete difference equation, so that the update of the parameters is also following the gradient of the difference equation. A possibility is to find the gradient of change in R_0, R_1, and C_1 with respect to the output in the transfer function. These gradient relationships can then be converted into the discrete time domain to find a regressor more aligned with the physical reality. The drawback of this method is that it will be more computationally intensive for online application; depending on the processor speed, it could pose an implementation issue.

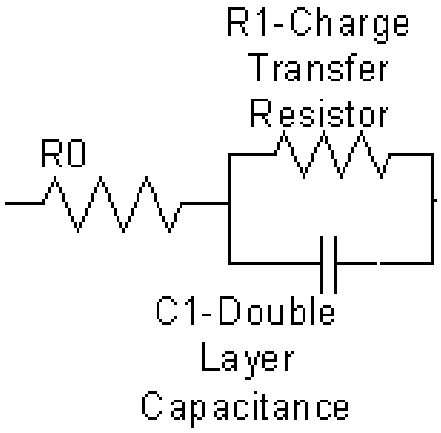

Fig. 3-4 R-RC Impedance Network Model for the Battery Dynamic Components

Equations (3.2) and (3.3) state the continuous time differential equation model of the impedance network in Fig. 3-4.

$$\frac{dv_{c1}}{dt} = \frac{-v_{c1}}{R_1 C_1} + \frac{i}{C_1} \tag{3.2}$$

$$v_{out} = v_{c1} + R_0 i \tag{3.3}$$

Reformulate (3.2) and (3.3) in the traditional state space model ABCD form as follows:

$$\frac{dv_{c1}}{dt} = Av_{c1} + Bi \Rightarrow v_{c1} S = Av_{c1} + Bi \tag{3.4}$$

$$v_{out} = Cv_{c1} + Di \tag{3.5}$$

where $A = \frac{-1}{R_1 C_1}$, $B = \frac{1}{C_1}$, $C = 1$, $D = R_0$, and the parameter set $\theta = \begin{Bmatrix} R_0 \\ R_1 \\ C_1 \end{Bmatrix}$. The partial derivatives of the state space model terms with respect to physical parameters are then listed.

Table 3-3 List of Partial Derivatives for State Space Model Terms Relative to Parameters

$\frac{dA}{dR_0} = 0$	$\frac{dB}{dR_0} = 0$	$\frac{dC}{dR_0} = 0$	$\frac{dD}{dR_0} = 1$
$\frac{dA}{dR_1} = \frac{1}{R_1^2 C_1}$	$\frac{dB}{dR_1} = 0$	$\frac{dC}{dR_1} = 0$	$\frac{dD}{dR_0} = 0$
$\frac{dA}{dC_1} = \frac{1}{R_1 C_1^2}$	$\frac{dB}{dC_1} = \frac{-1}{C_1^2}$	$\frac{dC}{dC_1} = 0$	$\frac{dD}{dC_1} = 0$

Now the state v_{c1} partial derivatives $Z_{R_0} = \frac{dv_{c1}}{dR_0}$, $Z_{R_1} = \frac{dv_{c1}}{dR_0}$, and $Z_{C_1} = \frac{dv_{c1}}{dR_0}$ with respect to physical parameters will be derived as a function of each physical parameter R_0, R_1, and C_1. Take the integral of (3.4) and manipulate the expressions to get (3.6), where k is an integer 0, 1, 2 and $\theta_0 = R_0$, $\theta_1 = R_1$, and $\theta_2 = C_1$.

$$v_{c1} = \int_{-\infty}^{t} Av_{c1} + Bi \, d\tau \Rightarrow \frac{dv_{c1}}{d\theta_k} = \int_{-\infty}^{t} A\frac{dv_{c1}}{d\theta_k} + \frac{dA}{d\theta_k} + \frac{dB}{d\theta_k} i \, d\tau \tag{3.6}$$

$$\frac{dZ\theta_k}{dt} = AZ\theta_k + \frac{dA}{d\theta_k} + \frac{dB}{d\theta_k} i \tag{3.7}$$

Based on (3.7) and Table 3-3, $\frac{dZ_{R_0}}{dt}$, $\frac{dZ_{R_1}}{dt}$, and $\frac{dZ_{C_1}}{dt}$ can be found as follows:

$$\frac{dZ_{R_0}}{dt} = \frac{-1}{R_1C_1} Z_{R_0} \tag{3.8}$$

$$\frac{dZ_{R_1}}{dt} = \frac{-1}{R_1C_1} Z_{R_1} + \frac{1}{R_1^2C_1} v_{c1} \tag{3.9}$$

$$\frac{dZ_{C_1}}{dt} = \frac{-1}{R_1C_1} Z_{C_1} + \frac{1}{R_1^2C_1} v_{c1} + \frac{-1}{C_1^2} i \tag{3.10}$$

Let the output voltage v_{out}'s partial derivatives with respect to physical parameters be φ_{θ_k}'s. These can be found from (3.5) with both $\frac{dv_c}{d\theta_k}$, or equivalently Z_{θ_k}'s, and Table 3-3.

$$\varphi_{R_0} = Z_{R_0} + i \tag{3.11}$$

$$\varphi_{R_1} = Z_{R_1} \tag{3.12}$$

$$\varphi_{C_1} = Z_{C_1} \tag{3.13}$$

Notice that (3.8) and (3.11) can be paired as a state space model with φ_{θ_k}'s as outputs, Z_{θ_k}'s as states, and i as input; so do (3.9) ,(3.12) and (3.10) ,(3.13) with the relationship between v_{c1} and i from (3.2) plugged into (3.9) and (3.10). The resulting transfer functions, with the Laplace operator S replacing the derivative, are listed below:

$$\frac{\varphi_{R_0}}{I} = 1 \tag{3.14}$$

$$\frac{\varphi_{R_1}}{I} = \frac{1}{(R_1C_1S+1)^2} \tag{3.15}$$

$$\frac{\varphi_{C_1}}{I} = \frac{-R^2{}_1S}{(R_1C_1S+1)^2} \tag{3.16}$$

By the forward method, (3.14), (3.15), and (3.16) can all be mapped into the discrete domain, deriving $\varphi_{\theta_k}(z)$'s, where z is the discrete delay operator. The purpose for obtaining $\varphi_{\theta_k}(z)$'s is to have a direct access to all of the gradients of the output voltage v_{out} with the physical parameters R_0, R_1, and C_1 and to set up the discrete parameter updater accordingly. The last step is to find the matrix based on Table 3-2 that transforms $\varphi_{R_0}(z)$, $\varphi_{R_1}(z)$, and $\varphi_{C_1}(z)$ into $\varphi_{b_0}(z)$, $\varphi_{b_1}(z)$, and $\varphi_{a_1}(z)$. (3.17) is then the final updater form.

$$\begin{bmatrix} b_0(k) \\ b_1(k) \\ a_1(k) \end{bmatrix} = \begin{bmatrix} b_0(k-1) \\ b_1(k-1) \\ a_1(k-1) \end{bmatrix} + c[V_{out}(k) - \hat{V}_{out}(k)] \begin{bmatrix} \varphi_{b0}(k) \\ \varphi_{b1}(k) \\ \varphi_{b1}(k) \end{bmatrix} \tag{3.17}$$

While the derivation of $\varphi_{b_0}(k)$, $\varphi_{b_1}(k)$, and $\varphi_{a_1}(k)$ is lengthy, it only has to be performed once for a particular impedance structure. The derived $\varphi_{b_0}(k)$, $\varphi_{b_1}(k)$, and $\varphi_{a_1}(k)$ expressions, however, can be lengthy and demanding on the computational power for an online application; depending on the processor speed, this may be an implementation issue.

The third potential remedy is to separate the R-RC structure further into an R and an RC structure with the help of spectral separation. The separation should encourage convergence within each circuit element segment. The next section is devoted to a discussion of the merits and potential drawbacks of this additional spectral separation, proposed by Wiegman in [9].

The fourth remedy is to set up clear criteria for whether to accept the estimated parameter values. The particular criterion implemented in the code is to no allow the R_1 estimated value to vary more than 10% between consecutive samples. If the criterion is violated, the original discrete parameters b_0, b_1, and a_1, along with their transformed estimated physical parameters R_0, R_1, and C_1, are replaced with the values from the last sample. This method is adopted in the thesis.

3.2 Spectral Separation Method for System Identification

In this section, the spectral separation method is compared with the identification technique used in the proposed method, combined estimation, in an R-RC simulation model constructed in Simulink. The results are not meant to be representative of general cases, but merely serve as an example for the potential issues associated with the spectral separation method.

3.2.1 Simulated R-RC Model and the Built in Assumptions

The model is a simple R in series with RC. However, to simulate the increasing impedance of a lead-acid battery throughout discharge, the fast dynamic element R_0 is given as a function that increases with time. The following tables have the details of the simulation.

Table 3-4 Simulation Conditions

R_0	$0.17 + \frac{0.04t^4}{1340^4}$ [Ohms]
R_1	1 [Ohms]
C_1	100 [Farads]
Time	1340 [Seconds]
Sampling Frequency	4 [Hz]
Peak Current	20 [A]
Voltage Measurement White Noise Power Spectrum Density	0.00005 [V]
Anti-Aliasing Filter	0.8 [Hz]
Anti-Aliasing Filter Order	1 [/]

Table 3-5 Parameter Setting for Combined Estimation Method

Initial R_0	0.175 [Ohms]
Initial R_1	1.11 [Ohms]
Initial C_1	90 [Farads]
Updater Gain c	0.002 [/]
Forgetting Factor	None
Pole Update Correction Factor	10 [/]
Rejection Factor	10% [/]
Minimum Update Threshold	0 [A]

Table 3-6 Parameter Setting for Spectral Separation Method

Initial R_0	0.175 [Ohms]
Initial R_1	1.11 [Ohms]
Initial C_1	90 [Farads]
Updater Gain c	0.002 [/]
Forgetting Factor	None
Pole Update Correction Factor	None [/]
Spectral Filter Order	1 [/]
R_0 Estimation Info Spectrum	Above 0.01 [Hz]
R_1C_1 Estimation Info Spectrum	Below 0.01 [Hz]
R_0 Estimation Minimum Update Threshold	2 [A]
R_0 Evolution Filter	0.1 [Hz]

The current excitation used in this simulation is also the EPA driving cycle scaled such that the maximum current is 20 Amps. Additional white noise is added at voltage measurement to simulate the measurement error. Table 3-5 is similar to Table 2-2 and Table 2-3 in terms of the items listed and records the simulation settings for the combined estimation method.

The spectral separation method's properties are listed in Table 3-6. The frequency spectral separation takes in the measured voltage and current data and divides each into a high-frequency and low-frequency component at above 0.01 Hz and below 0.01 Hz, respectively. Using KVL, the voltage and current across R_0 and R_1C_1 are isolated from each other. The voltage and current across R_0 are then high-pass-filtered at 0.01 Hz, while voltage and current across R_1C_1 are low-pass-filtered at 0.01 Hz.

The raw R_0 estimate at every time sample is found by dividing the high-frequency voltage obtained through KVL by the high-frequency current, as shown in (3.18) below. V and I are the measured terminal voltage and current, respectively. Θ is the parameter set for the R_1C_1 structure discussed in 1.6.1.

$$R_{0\_unfiltered}(k) = \frac{HPF\{V(k)-\hat{V}_{rc}(I(k),\theta(k-1))\}}{HPF\{I(k)\}} \tag{3.18}$$

$$R_0(k) = LPF\{R_{0\_unfiltered}\}(k) \tag{3.19}$$

To stabilize the estimation process, the R_0 estimate signal is also low-pass-filtered at 0.1 Hz. This low-pass filter ensures that there are no sudden changes in the R_0 estimate from sample to sample. The "R_0 Estimation Minimum Update Threshold" allows R_0 to update only when sufficient excitation exists.

The estimation technique for R_1 and C_1 is the same as discussed in Section 1.6.1 with an updater gain c, except that the input current and output voltage are low-pass-filtered at 0.01 Hz and the output voltage term subtracts the R_0 voltage component as shown below:

$$V_{rc}(k) = \text{LPF}\{ V(k) - R_0(k)\, I(k) \}(k) \tag{3.20}$$

3.2.2 Simulation Results

The simulation results are presented in this subsection. The voltage tracking performances are first compared in Fig. 3-5 and Fig. 3-6. The average error per sample for the spectral separation method case is 0.0068 Volts, while the combined estimation method yields an average error of 0.1142 volts. A clear advantage in convergence can be observed for the spectral separation method. The evolution of error in the voltage tracking for both cases is shown in Fig. 3-7 and Fig. 3-8.

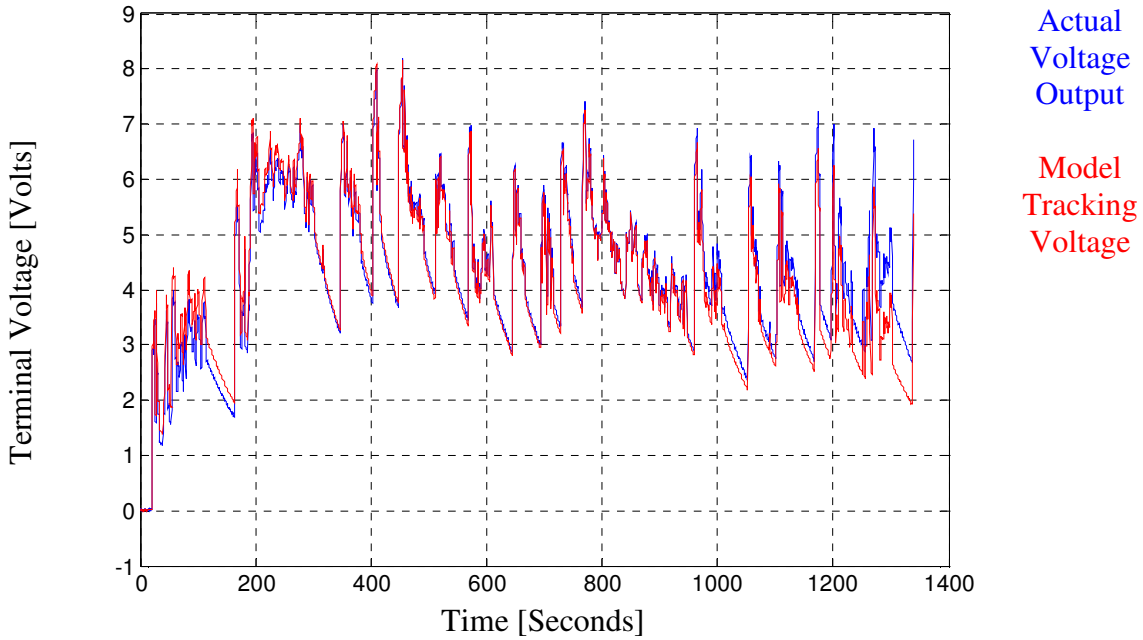

Fig. 3-5 Voltage Tracking Performance for Combined Estimation Method

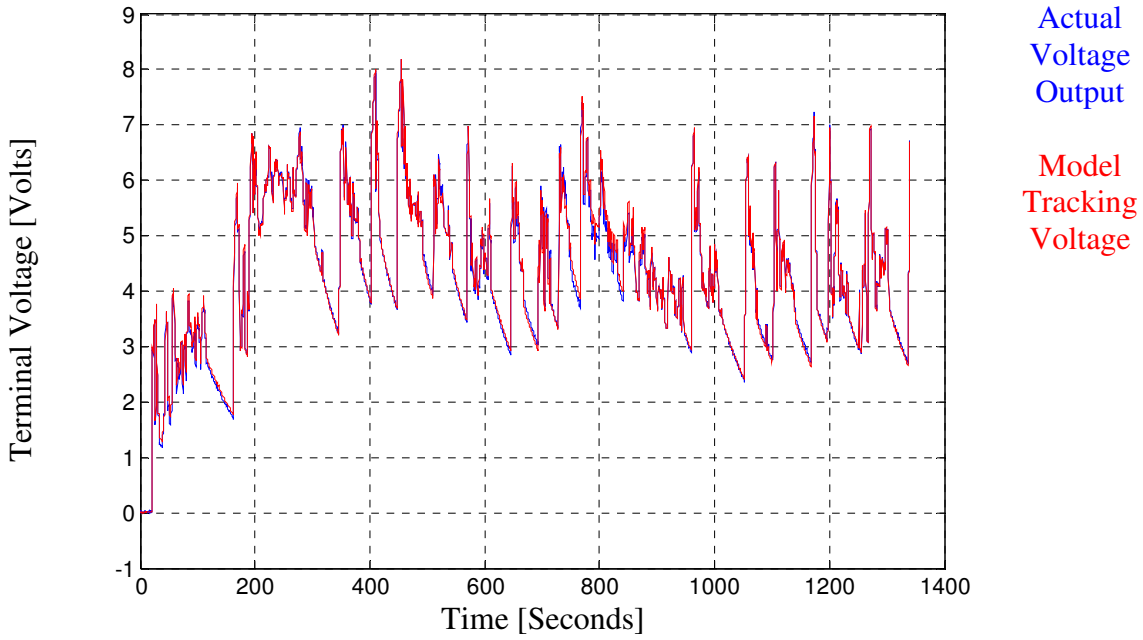

Fig. 3-6 Voltage Tracking Performance for Spectral Separation Method

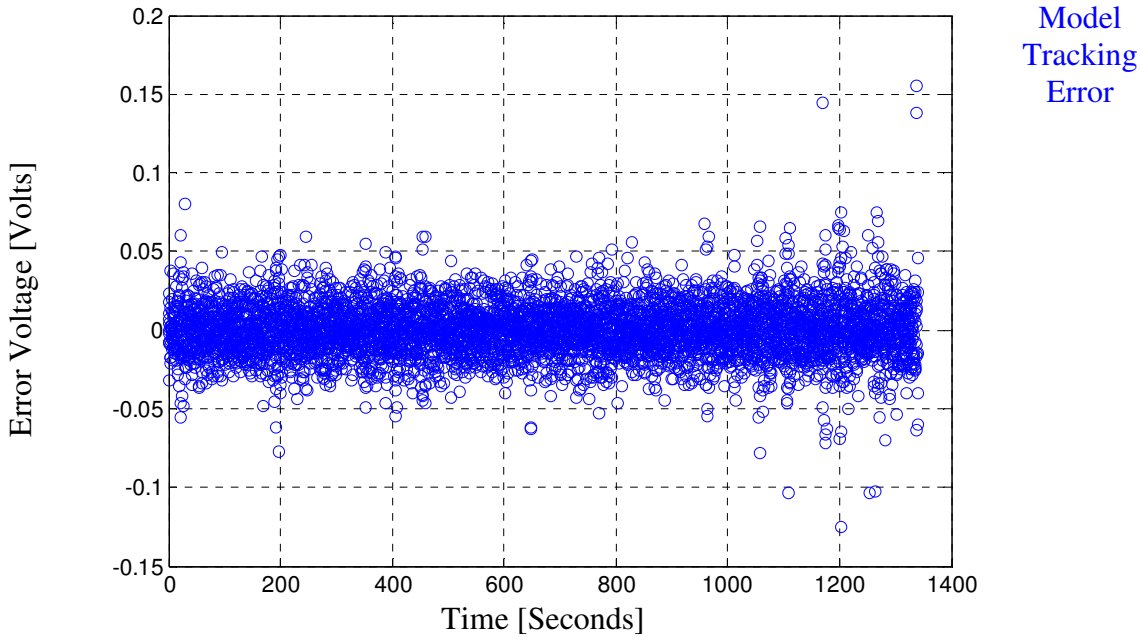

Fig. 3-7 Voltage Tracking Error for Combined Estimation Method

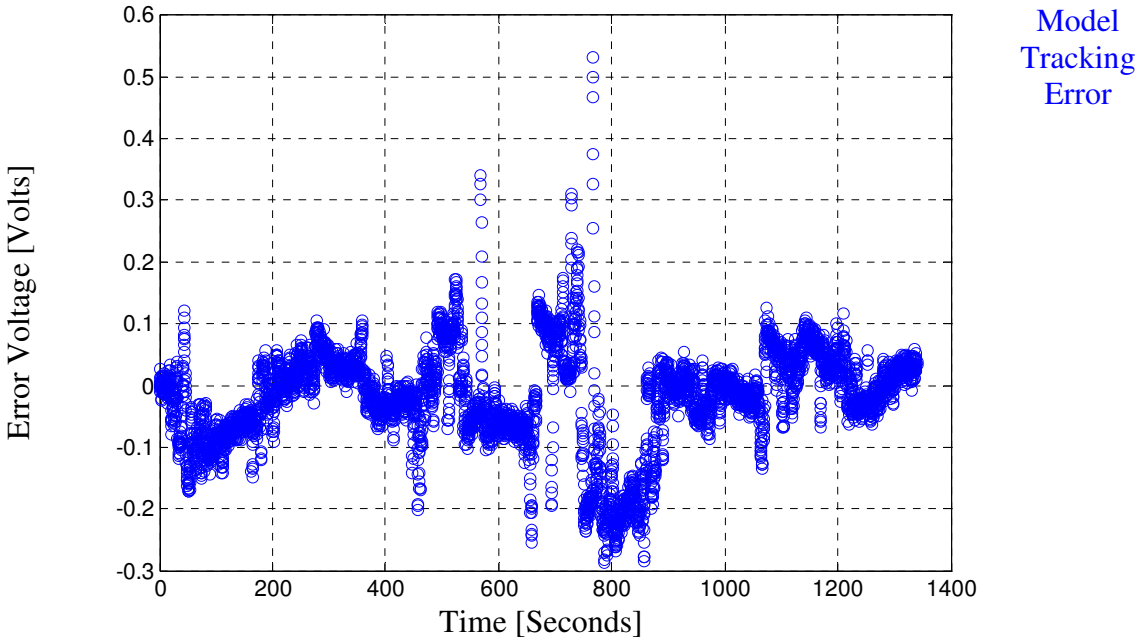

Fig. 3-8 Voltage Tracking Error for Spectral Separation Method

From Fig. 3-7 and Fig. 3-8, the errors in both cases demonstrate the respective models' limitations. The combined estimation method performs a bit worse at the end when the value of R_0 increases quickly and the convergence speed becomes inadequate. The spectral separation method, on the other hand, suffers from oscillation between the separated components, and thus exhibits an error that swings up and down throughout the simulation. Notice that even though, on average, the spectral separation method has a smaller error, it suffers greater error magnitude for the worst-case scenario.

The evolution of estimated R_0 is shown next, and it will serve to demonstrate the oscillation of the spectral separation method. As far as the convergence speed for the direct method is concerned, it was found in simulation that the anti-aliasing filter reduces the convergence speed significantly. This observation is thought to be due to the high frequency attenuation brought by the filter. Since the anti-aliasing filter is required for all measurements in practice, the simulation still retains this feature.

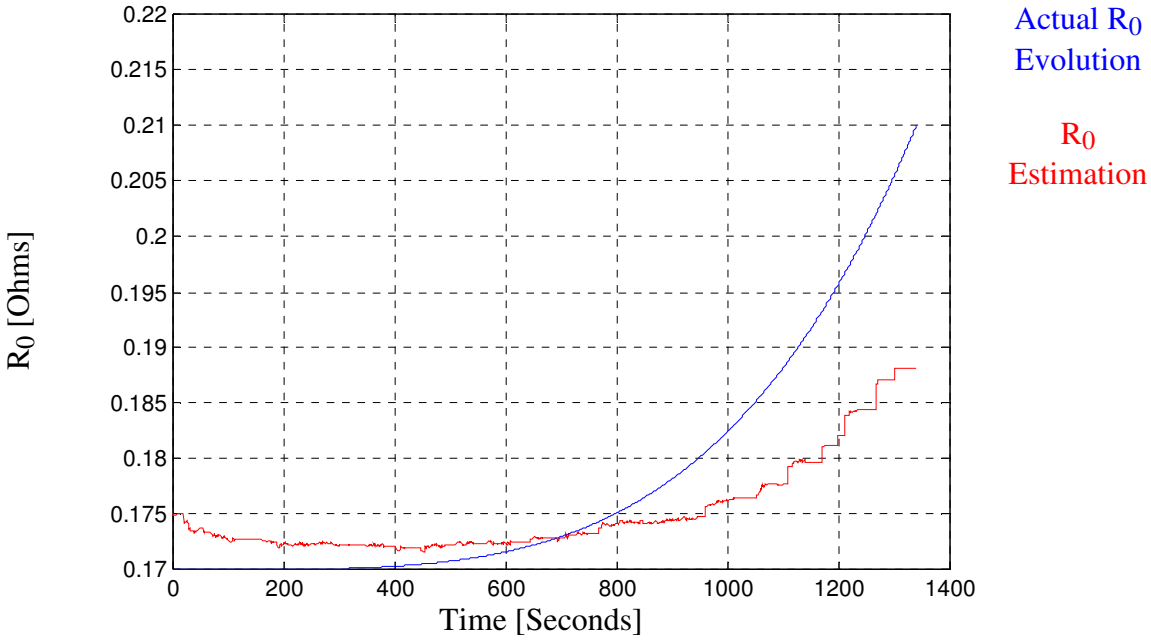

Fig. 3-9 R_0 Estimation Performance for Combined Estimation Method

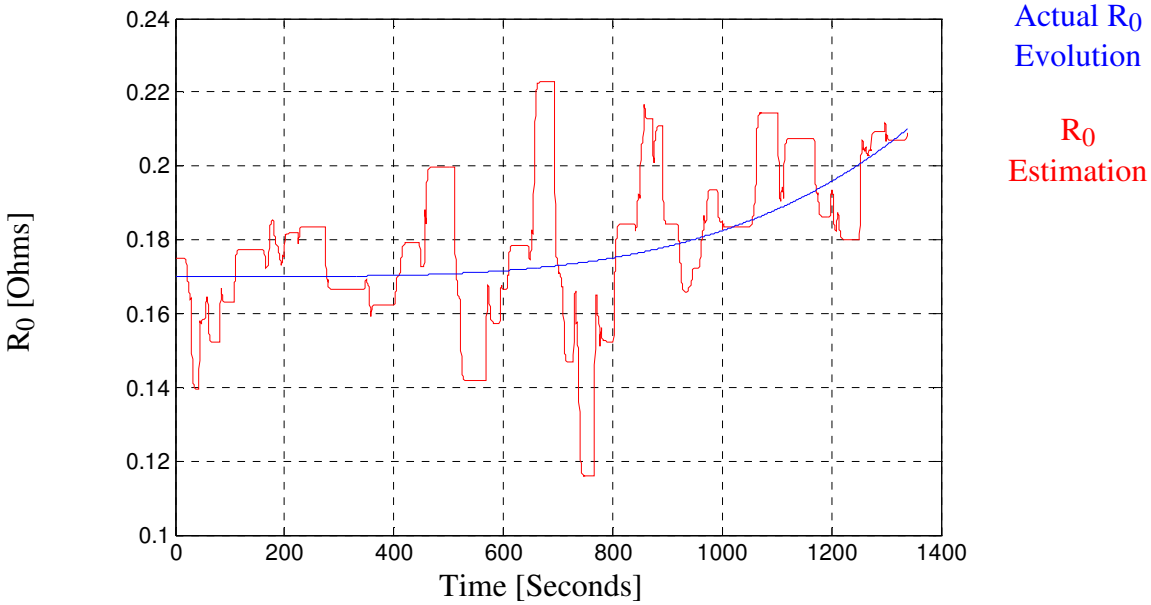

Fig. 3-10 R_0 Estimation Performance for Spectral Separation Method

Fig. 3-9 and Fig. 3-10 show the major rationale for including the simulation in the discussion. Although the least square error estimation performance of the spectral separation method is superior on average (in this particular simulation), it shows an

oscillation in the estimated R_0. The reason for the oscillation is simple. There is an interaction between the updating dynamics of R_0 and R_1,C_1. The oscillation could be potentially troublesome if one were to use the trend of the impedance evolution for diagnostic purposes, such at power capability prediction or aging comparison between two batteries. In short, if a consistent trend is what the estimation technique is seeking, then the spectral separation technique clearly suffers a significant disadvantage.

Another point that needs to be made is that the simulation condition is more "estimation friendly" compared with the Optima lead-acid battery estimation in this document. The sampling frequency is slower. The time constant of the R_1, C_1 pair is also longer. From the equations in Table 3-1, these two conditions would make b_0 and b_1 differ more in magnitude, reducing the chance of having estimation detached from physical reality.

The longer time constant also makes it easier to have enough room to perform spectral separation. In addition, in the proposed model for the battery, there is an low-pass filter on the value of $\hat{v}_{eff}$. The cut-off frequency of that low-pass filter places a lower limit on where the spectral frequency separation can be set. In real applications, the sampling rate might not be able to increase enough so that the spectral separation has room to avoid the interaction between the updating dynamics.

In addition, the time constant R_1, C_1 pair in the real battery might also be close to the frequency of the low-pass filter for $\hat{v}_{eff}$. In that case, the only way to maintain the spectral separation is to lower the frequency of the low-pass filter for $\hat{v}_{eff}$, causing a sluggish response of the $\hat{v}_{eff}$ estimation.

Furthermore, the estimation technique is always dependent on the frequency contents of the input current. While it is not easy to show mathematically, it is possible to imagine the spectral separation method is less tolerable to an input with frequency content concentrated only in a small part of the spectrum, e.g., excitation of only high frequency that makes the separate estimation of R_1, C_1 pair difficult. Additional safeguards on stability would be required, complicating the system further.

The proposed combined estimation method, on the other hand, has the advantage of being simpler to implement and exhibits a clear trend in the estimate of the fast dynamic element R_0.

To complete this simulation discussion, the results for the estimation of R_1 and C_1 with the two techniques are presented here in Figs. 3-11 to 3-14. Here the parameter rejection factor is implemented, resulting in physical parameters staying within reasonable bounds for the combined estimation method. Clearly, the estimator performance for R_1 and C_1 is better for the spectral separation method, which is why it was considered. With the reservations in mind on the practicality of the spectral separation method for all potential applications, this thesis has adopted the combined estimation method for all analysis.

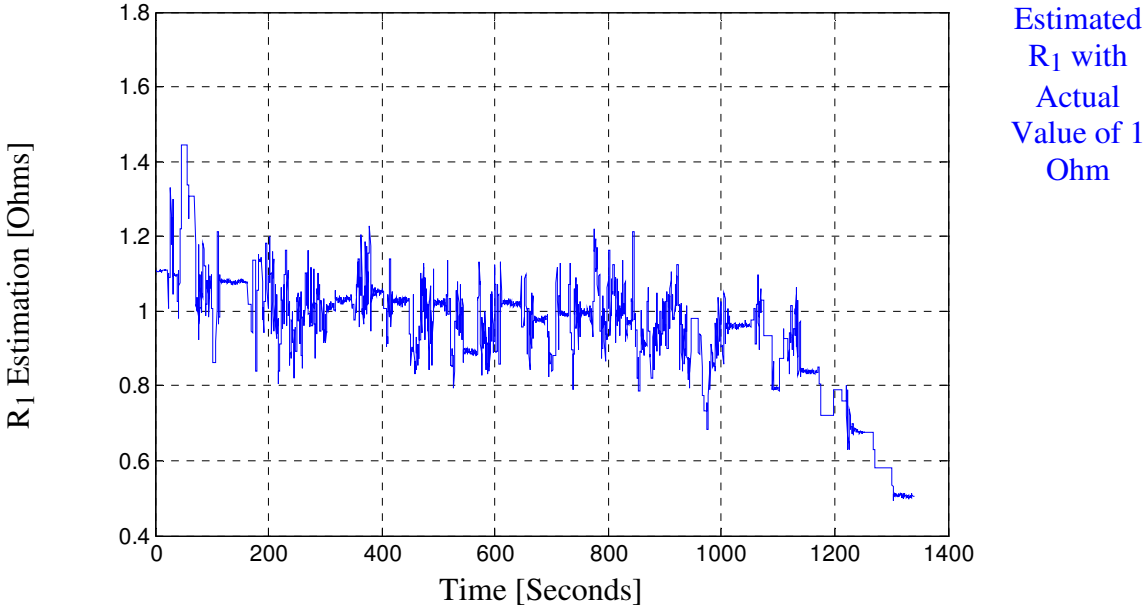

Fig. 3-11 R_1 Estimation for Combined Estimation Method

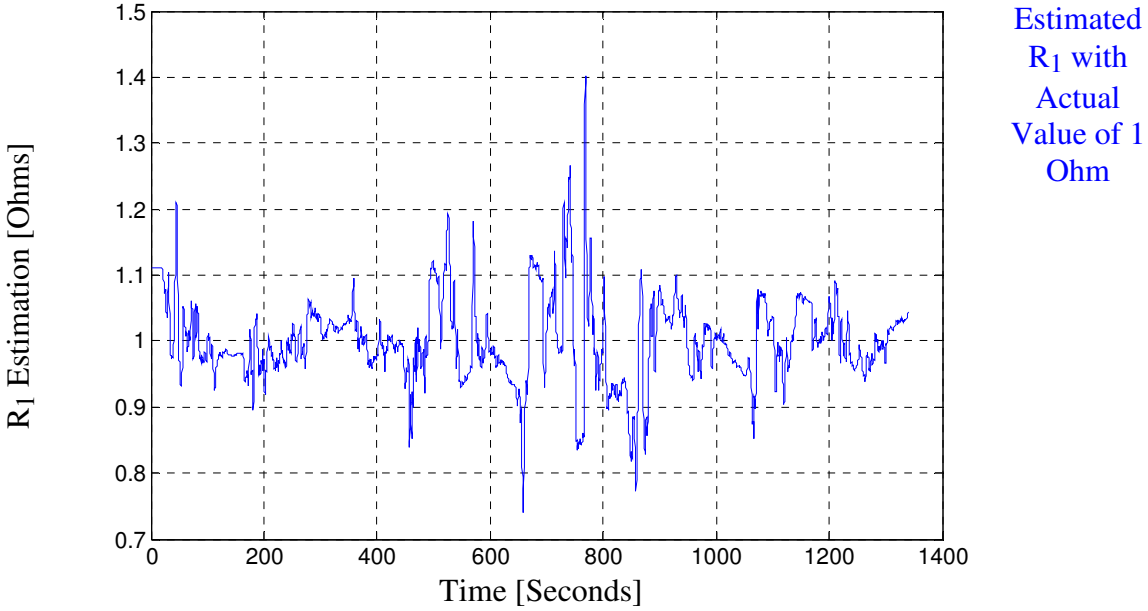

Fig. 3-12 R_1 Estimation for Spectral Separation Method

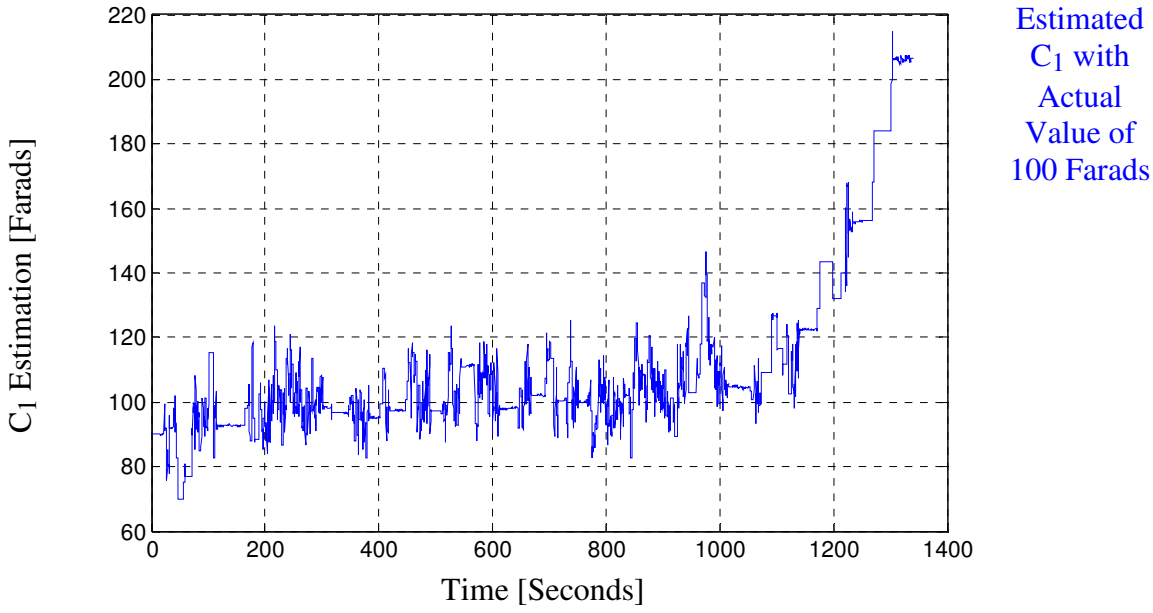

Fig. 3-13 C_1 Estimation for Combined Estimation Method

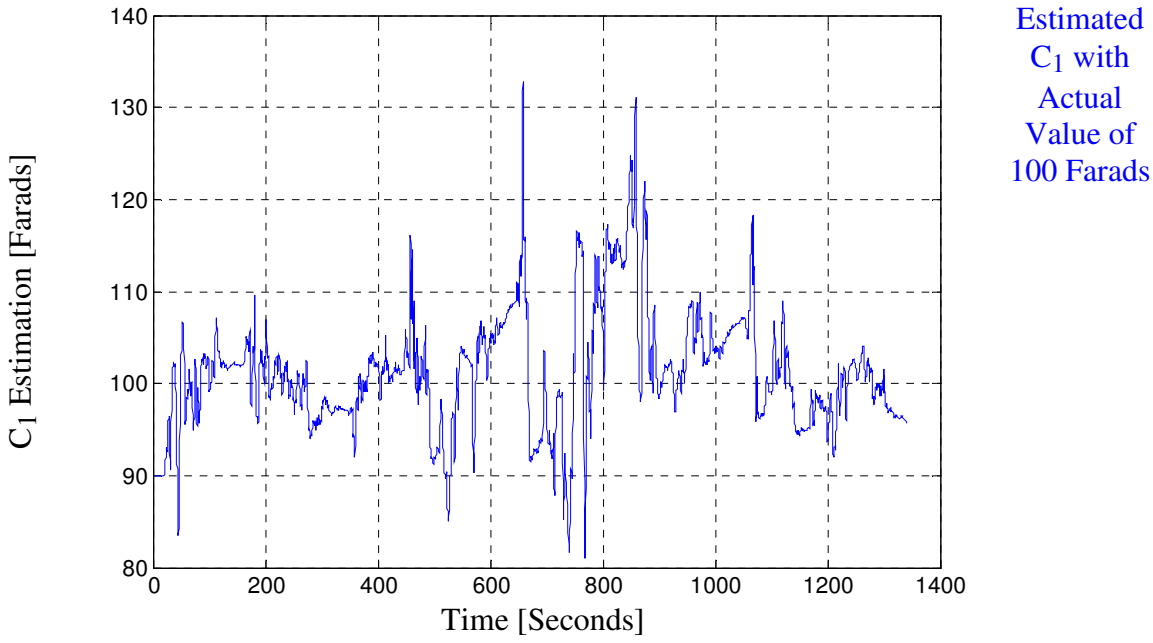

Fig. 3-14 C_1 Estimation for Spectral Separation Method

3.3 Short Term Power Capability Prediction

With the developed model that updates continuously during the battery operation, a natural application for the model is to predict the future terminal voltage for a specified

current profile. The verification of the model is also easy to perform by comparing the actual measured voltage with the prediction.

The power capability prediction is very similar in concept with the cranking capability prediction (SOF) discussed in the state-of-the-art review in Chapter One [9], [45]. By being able to predict the terminal voltage for a given current profile, the system has the opportunity to identify the battery's inability to perform the task before the actual load is applied.

3.3.1 Evolution of R_0 during Discharge

Due to the nonlinear nature of the double-layer capacitance and charge transfer resistance discussed previously, the estimation of R_0 is the only reliably traceable time domain impedance parameter for the proposed methodology within a driving cycle. Fig. 3-15 and Fig. 3-16 show the evolution of estimated R_0 during an EPA driving cycle as a function of discharged Amp-hours for both the model with and without the diffusion component.

The two modeling approaches, one with $\hat{v}_{eff}$ LPF estimation and the other with diffusion offline model, yield virtually identical results. This result is expected since R_0 estimation depends mostly on the high-frequency content that is spectrally remote from where the main difference between the two modeling approaches takes place. It is also worth noting that the rated impedance of the D34M battery is 3 mΩ according to the datasheet.

The estimation results are also consistent with the observations in the literature that the impedance of the battery increases as the discharge continues. The slight initial drop in R_0 estimation can be attributed to either inaccurate initial parameter guesses, or

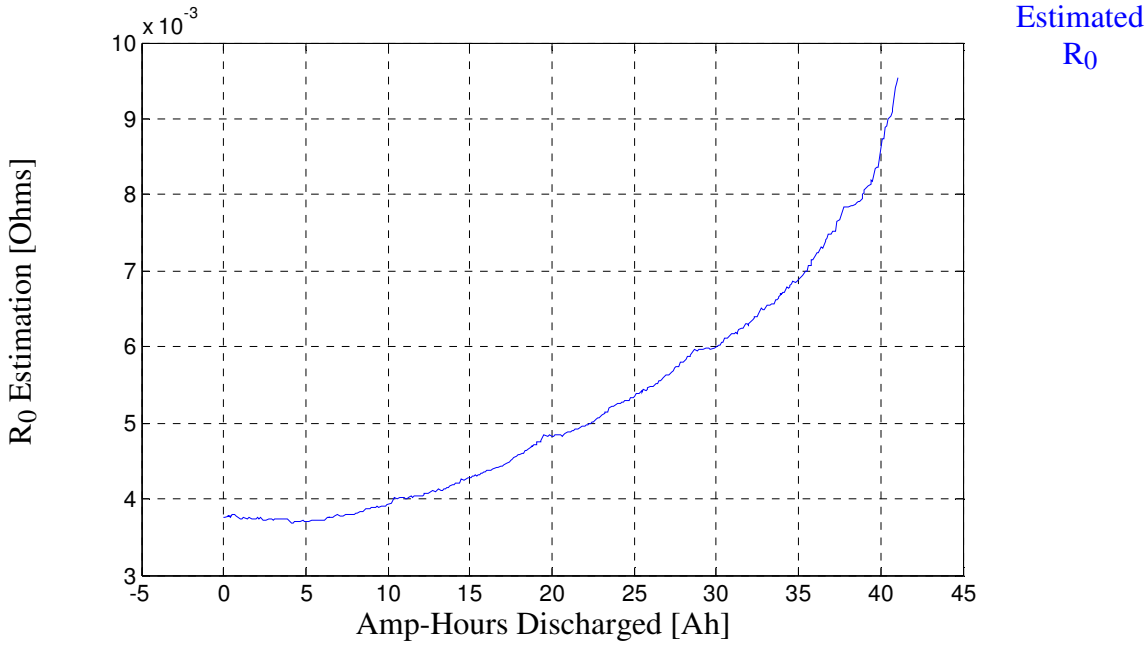

Fig. 3-15 R_0 Estimation for the Model without Diffusion Component for EPA Driving Cycle

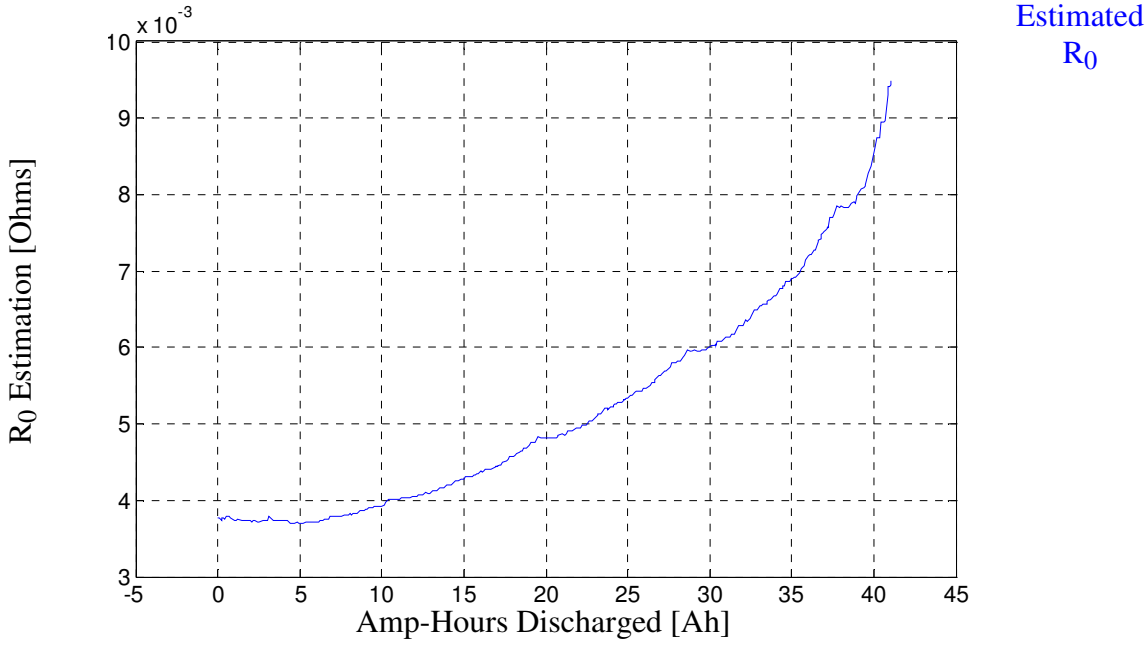

Fig. 3-16 R_0 Estimation for the Model with Diffusion Component for EPA Driving Cycle

the diffusion effect that is dissipating itself while the discharge is under way. For the square wave discharge cycle, the R_0 estimation results are shown in the following graphs in Fig. 3-17 and Fig. 3-18.

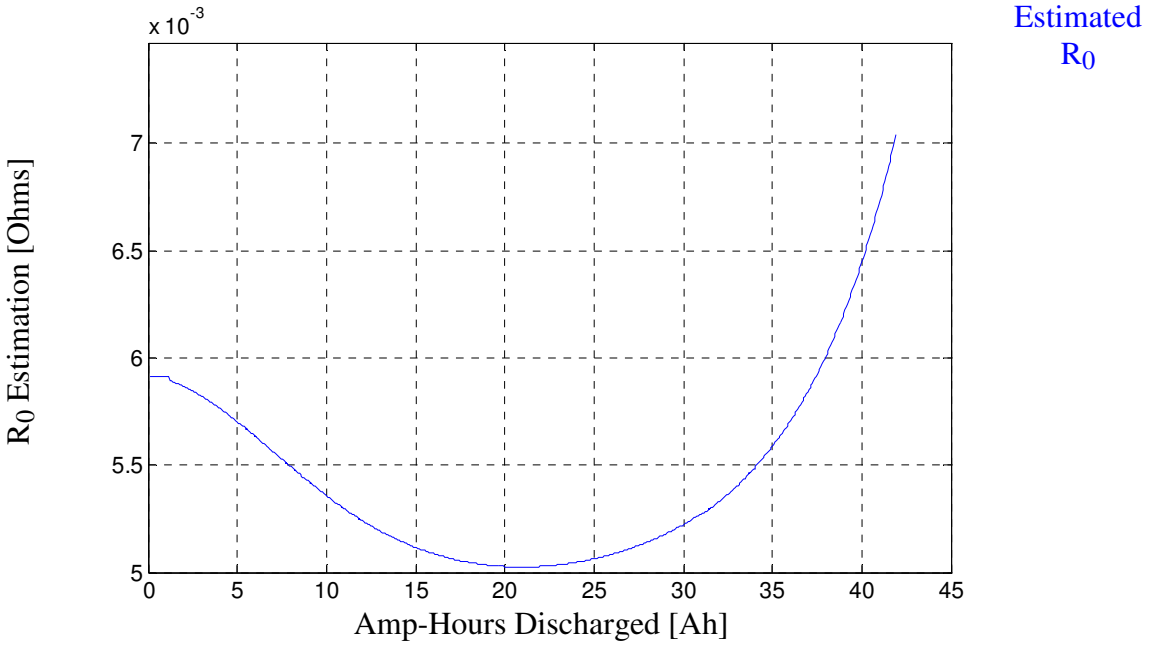

Fig. 3-17 R_0 Estimation for the Model without Diffusion Component for Square Wave Driving Cycle

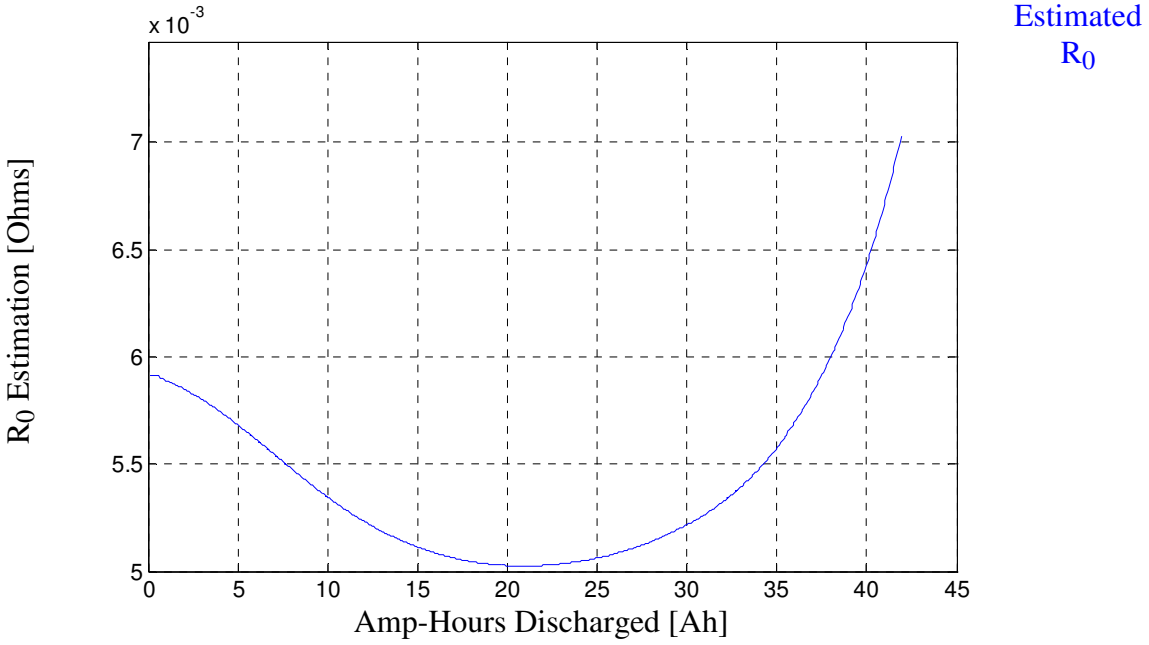

Fig. 3-18 R_0 Estimation for the Model with Diffusion Component for Square Wave Driving Cycle

Fig. 3-17 and Fig. 3-18 show that for this particular driving cycle, the battery appears to have decreasing series resistance during the beginning of the discharge while the end of the discharge exhibits the familiar feature of rising R_0 resistance. The initial

decrease in impedance is possibly due to both the diffusion effect and the square waveform properties. When the charge diffusion effect is still present, the continuously falling voltage could add to the impedance estimates. In addition, the battery impedance has different impedance values for discharging and relaxing modes.

The periodic nature of the square-wave cycle in alternating between the two modes could make the updater run less smoothly, slowing down the convergence speed. This slowdown could explain why the end-of-discharge resistance value in Fig. 3-15 and Fig. 3-16 is higher than Fig. 3-17 and Fig. 3-18.

With respect to the estimated R_0 value before the end-of-discharge region, the increase in R_0 estimation could also indicate aging effect, or the battery has simply broken in and stabilized. The experiment for Fig. 3-17 and Fig. 3-18 was performed about three weeks later than the experiment for Fig. 3-15 and Fig. 3-16.

3.3.2 Short Term Power Capability Prediction Experiment Results

In the EPA driving cycles, there are prolonged periods when the current is idle at zero for an extended period of time. These periods are ideal for testing the model's capability to predict SOF, or cranking capability. That is, the impedance circuit model updated at that time instant can be applied along with an effective voltage source to predict the terminal voltage.

Making use of the parameter rejection factor on R_1, the parameters used in these analyses are the most recently estimated values that are physically sensible. The method for selecting the starting voltage before the load current is applied is to pick the terminal voltage value immediately before the cranking current load is applied. The predicted

voltage response can be plotted with the current profile, together with the measured battery response when the cranking load is subsequently applied.

The short-term power capability prediction for the adopted modeling approach using no diffusion voltage is shown together with measured battery response in Fig. 3-19, Fig. 3-20, Fig. 3-21, and Fig. 3-22. Fig. 3-23 is the current profile used in Fig. 3-19.

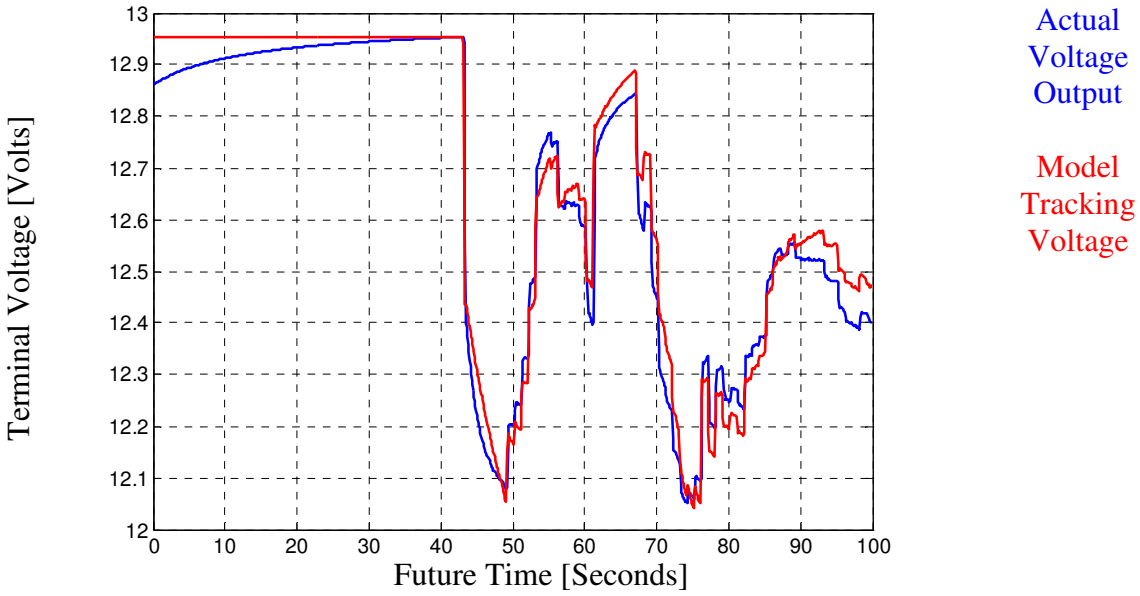

Fig. 3-19 Model-Based Future Voltage Estimation vs. Actual Measurement with $\hat{R}_0 + \hat{R}_1 = 0.0097$ [Ohms]

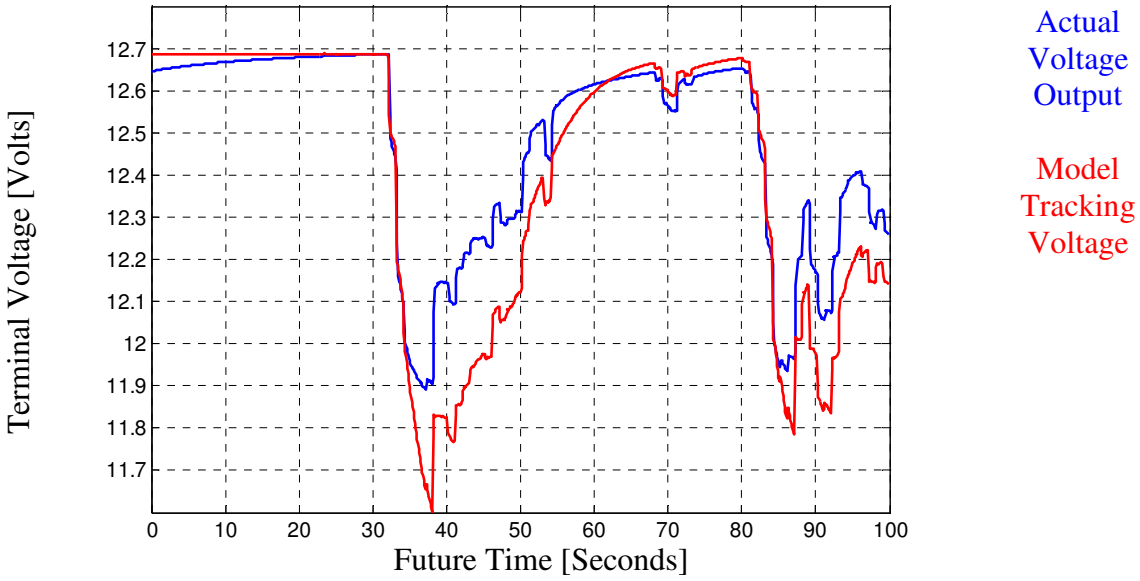

Fig. 3-20 Model-Based Future Voltage Estimation vs. Actual Measurement with $\hat{R}_0 + \hat{R}_1 = 0.0142$ [Ohms]

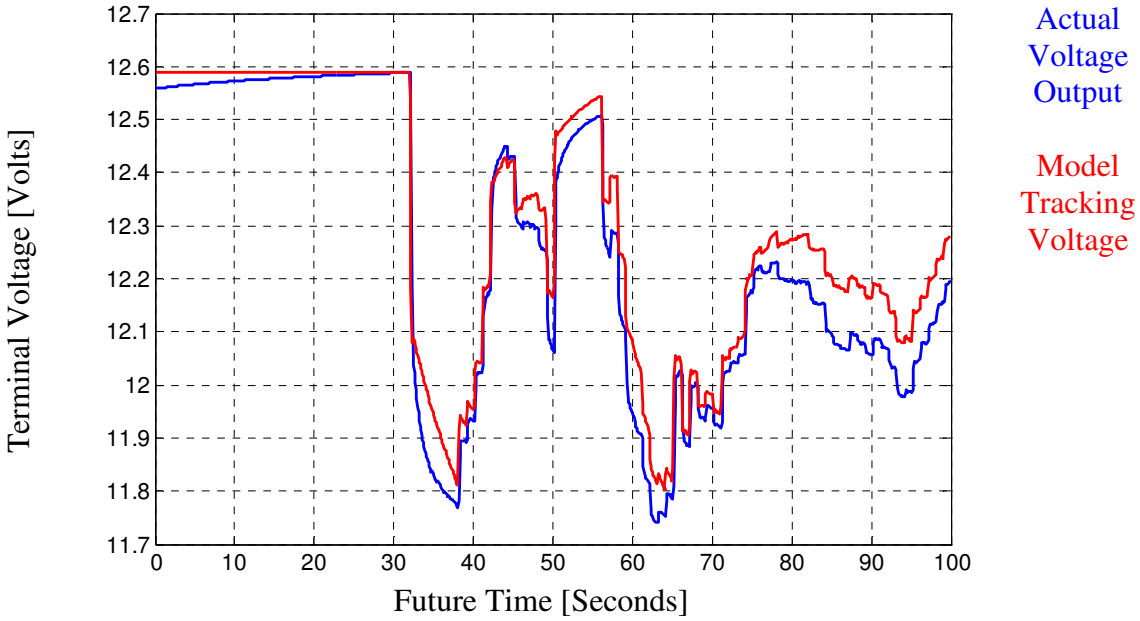

Fig. 3-21 Model-Based Future Voltage Estimation vs. Actual Measurement with $\hat{R}_0 + \hat{R}_1 = 0.0081$ [Ohms]

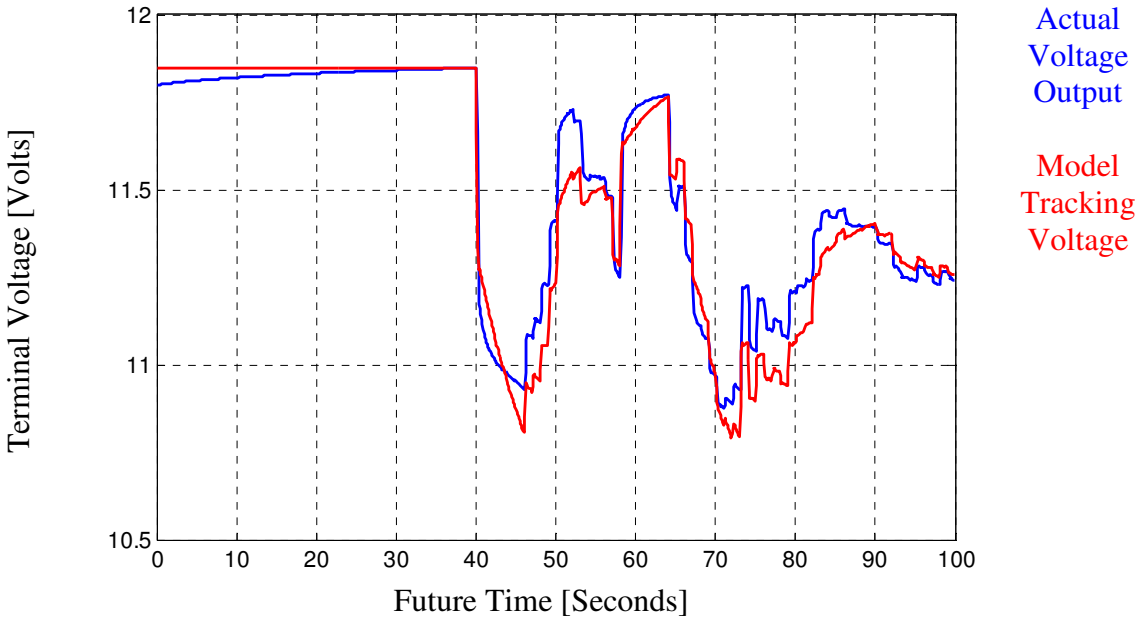

Fig. 3-22 Model-Based Future Voltage Estimation vs. Actual Measurement with $\hat{R}_0 + \hat{R}_1 = 0.0115$ [Ohms]

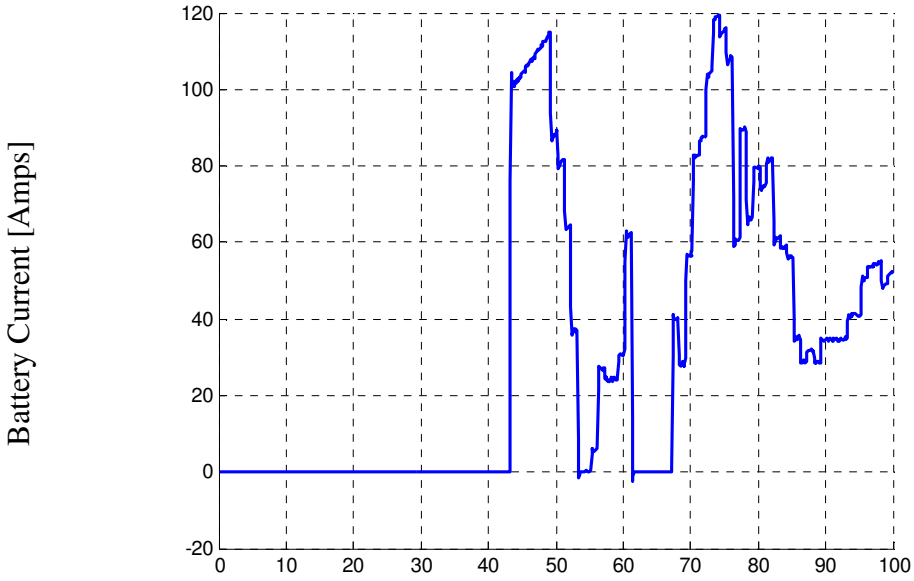

Current Profile used in Fig. 3-19

Fig. 3-23 The Current Profile Used for Fig. 3-19

Since the errors are accumulative, the comparison of errors in the first peak load provides some insight that the average/accumulative prediction error might not do. Table 3-7 lists the voltage error right after the first peak load current is applied for each figure.

Table 3-7 Voltage Prediction Errors at First Peak for Short Term Power Prediction

Periods	Prediction Error at First Peak
Fig. 3-19	0.02 [Volts]
Fig. 3-20	0.30 [Volts]
Fig. 3-21	0.04 [Volts]
Fig. 3-22	0.13 [Volts]

For completeness, Table 3-8 and Table 3-9 provide the average and maximum errors for the four cases, respectively.

Table 3-8 Average Voltage Prediction Errors for Short Term Power Prediction

Periods	Prediction Average Error
Fig. 3-19	0.05 [Volts]
Fig. 3-20	0.13 [Volts]
Fig. 3-21	0.07 [Volts]
Fig. 3-22	0.08 [Volts]

Table 3-9 Maximum Voltage Prediction Errors for Short Term Power Prediction

Periods	Prediction Maximum Error
Fig. 3-19	0.36 [Volts]
Fig. 3-20	0.35 [Volts]
Fig. 3-21	0.36 [Volts]
Fig. 3-22	0.33 [Volts]

While the maximum voltage prediction errors are similarly large for all four periods, the average voltage prediction errors show that certain previous history can cause much worse prediction performance than normal, e.g. Fig. 3-20. Certainly the fact that the diffusion voltage is not included in this short-term model could cause some uncertainty in the prediction capability. Many other variables and sources of nonlinearity can also influence the prediction performance. The dynamics of the updater as well as the state of the battery determine the performance of the prediction at any operating point.

From Fig. 3-19, Fig. 3-20, Fig. 3-21, and Fig. 3-22 above, the prospect of using the system for SOF prediction seems promising. While it is true the model does not incorporate all of the dynamics in the battery during short-term discharge, the model predicted waveforms show similar characteristics to that of the measured voltage response. Conceptually speaking, the benefit of an equivalent circuit approach is that electrical behavior of the system can be predicted. If one were to set a hard cut-off for low voltage limit during cranking to determine SOF, the information provided by the model allows the BMS to have a reference for the decision.

Although the equivalent circuit doe not perfectly predict the terminal voltage during the application of a load current, the impedance model serves as a mechanism to

estimate the battery's ability to deliver a specified load current profile based on the battery's present status.

3.4 The Prospect of Long Term Power Capability Prediction

Assuming the battery always undergoes similar discharge cycles determined by its application and that the battery is always at the same full charge state when the discharge begins, it is conceivable to incorporate measurement data and estimated parameters from previous cycles to predict the power capability of the battery significantly before the battery is discharged to the power capability of interest.

As discussed in Chapter One, the amount of energy stored in the battery is not the sole determining factor for the power capability. The impedance of the battery plays an equally important role along with the effective voltage source, v_{eff}. The benefit of being able to predict the long-term power capability would be to provide the BMS or the user a warning of the degradation of power capability, in addition to the depletion of charge stored.

An imaginary scenario can be the following. The BMS has determined that the vehicle battery has enough SOC to deliver the vehicle to the destination based on the average load current, its SOC estimation, and the trip distance. However, additional information arrives indicating that the last part of the trip is a mountainous ramp. This particular information needs to be factored into the calculations before the final determination of whether the battery can deliver the vehicle to its destination can be made, i.e., combining SOC and impedance information to obtain an estimate of the actual available energy.

By retaining information about the impedance evolution and the drop of effective voltage, v_{eff}, from the previous cycle, the BMS has an opportunity to develop a crude estimate of the power capability of the battery throughout the *whole* current trip, assuming consistent battery performance. Techniques for combining the impedance and effective voltage, v_{eff}, based on the developed battery model are considered here.

Batteries are generally limited at every instant by a minimum voltage, v_{low}, that they can deliver during discharge based on their current status. Thus, the power that the battery is delivering when its terminal voltage reaches v_{low} is the battery's theoretical maximum discharge power. Based on the equivalent circuit in Fig. 3-1, the steady-state impedance can be considered as:

$$R_{discharge} = R_0 + R_1 \tag{3.21}$$

Using the information on $R_{discharge}$, the estimated effective voltage $\hat{v}_{eff}$, and the pre-set lower terminal voltage v_{low}, the theoretical maximum discharge power P_{max} can be found by:

$$P_{max} = \frac{\hat{v}_{eff} - v_{low}}{R_{discharge}} v_{low} \tag{3.22}$$

Setting v_{low} to be 10.5 Volts for the Optima D34M battery, the evolution of P_{max} for the EPA driving cycle is shown in Fig. 3-24.

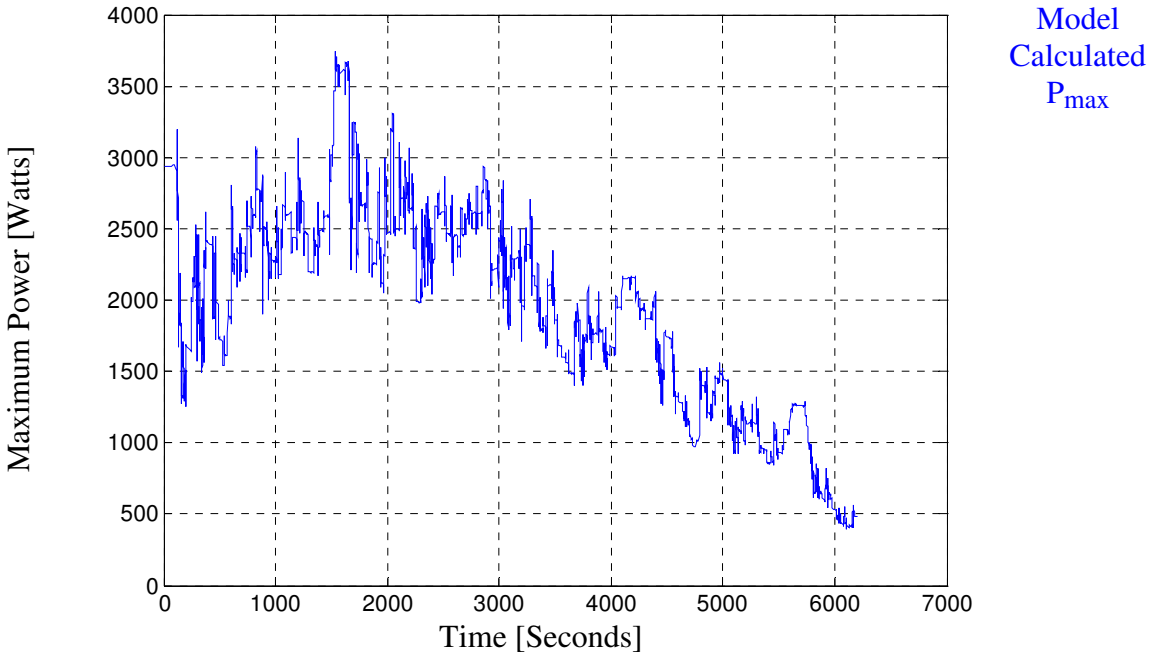

Fig. 3-24 Model Calculated P_{max} for the EPA Driving Cycle

Fig. 3-24 shows a general increase in power capability at the beginning of discharge, which is likely due to the diffusion effect that corresponds to a large initial R_1 value shown in Fig. 3-3. Given the diffusion effect on the R_1 estimated value, it is possible that the initial P_{max} is underestimated. Although $\hat{v}_{eff}$ would have been estimated erroneously upward by at most 0.5 Volts, the influence of a larger R_1, given its magnitude shown in Fig. 3-3, is likely to have dominated.

If, on the other hand, a maximum current demanded by the system, i_{max}, is specified by the connected load, the lowest possible battery terminal voltage, v_{low}, can also be found by:

$$v_{low} = \hat{v}_{eff} - i_{max} R_{discharge} \tag{3.23}$$

Based on the scaling of the EPA cycle performed in these experiments, i_{max} is 120 Amps. Equation (3.23) can also serve as a reality check on the performance of the

model. The calculated lower limiting voltage v_{low} is shown against the measured voltage in Fig. 3-25. If the model is performing correctly, the calculated low voltage v_{low} will be near the lower bound of the measured terminal voltage.

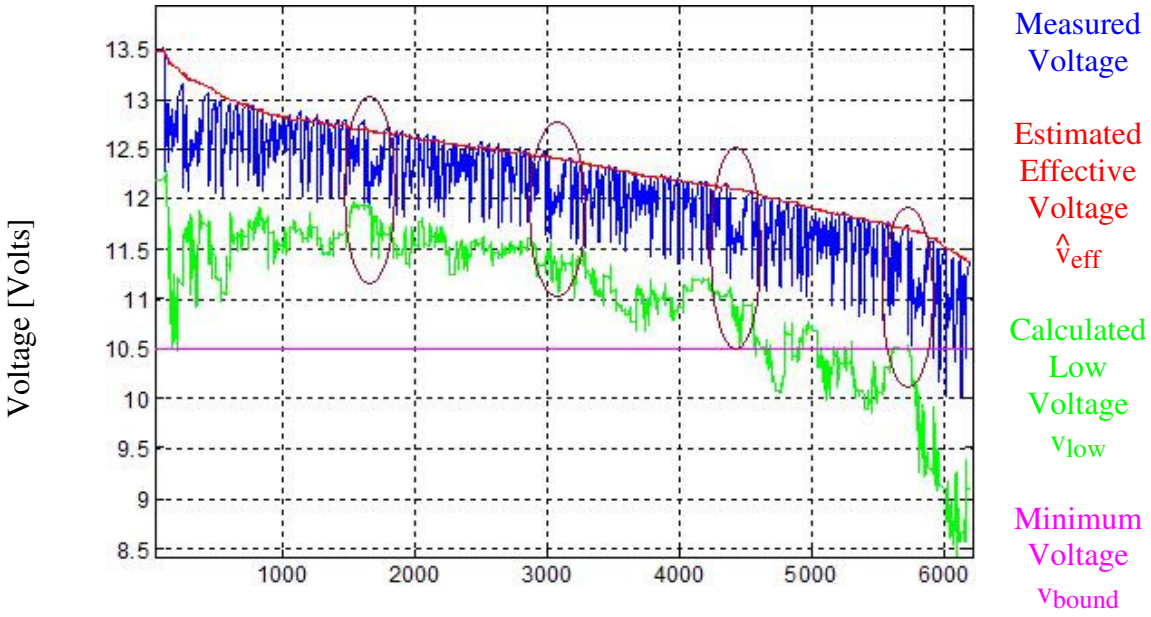

Fig. 3-25 Calculated Low Voltage v_{low} vs. the Measured Voltage

Based on (1.4) and (1.5), the relationship between the battery current and electrode overpotential is nonlinear, with a saturation of the electrode voltage under high battery current. In other words, a unit of increase in current in the high-current region corresponds to only a small increase in electrode voltage, i.e. the operating point value of R_1 in the high-current region should be small.

The system identification approach used here will naturally tend to converge to a large extent to the average operating condition, i.e. 25 Amps of average current for the EPA driving cycle. Certainly the ability to update at every time sample is a way to compensate against the nonlinear nature of the underlying system. But the updater gain

is a function of many variables and it cannot be too high before the estimator becomes oscillatory.

In Fig. 3-25, the calculated low voltage v_{low} is in general too conservative (i.e., too low) compared with the measured minimum battery voltage. If the system were to predict the end of discharge using v_{low} for this particular driving cycle, it would be in error by approx. 1000 seconds. That is approx. 20% too early for the discharge's completion. The system does not seem to update quickly enough to ensure good estimation in the high-current region. It can be further pointed out that the four best points (encircled) where the calculated low voltage v_{low} and the measured minimum battery voltage line up closest are periodic. The driving cycle repeats itself after 1340 seconds, and the best points are located at exactly the same position in their respective cycles.

Since the estimated value of R_1 is known to be too high for the extreme region of current, it can be concluded that the results from Fig. 3-24 are most likely quite conservative.

From the discussion above, the system's ability to calculate the battery's behavior in the high-load region is limited. It needs to be pointed out that this failure is common among all linear circuit-based battery state estimators. The updater is, in fact, compensating some of the nonlinear dynamics, while the linear Kalman filter-based methods simply treats any error as noise, thus exposing themselves to the same nonlinearity issue. In addition, when the updater actually converges for the lower current region, the nonlinearity causes the system to have a wrong voltage prediction under a subsequent maximum current condition.

The use of the proposed system for long-term power capability has been considered. This section highlights the concern about the model's ability to compensate for the nonlinearity of the system and, thus, its ability to serve as a reliable power indicator. The concept of utilizing the model parameters from the previous cycles to help predict the model's power capability in the current cycle is therefore not feasible for the proposed system because of the model's limitations. However, by correcting for the nonlinear nature of the battery dynamics, a model can potentially succeed in long-term power capability prediction.

A special discharge cycle has been performed to gain an understanding on the electrode voltage drop vs. the current magnitude relationship for the Optima D34M. Fig. 3-26 shows the battery pulse discharge profile for assessing the electrode voltage

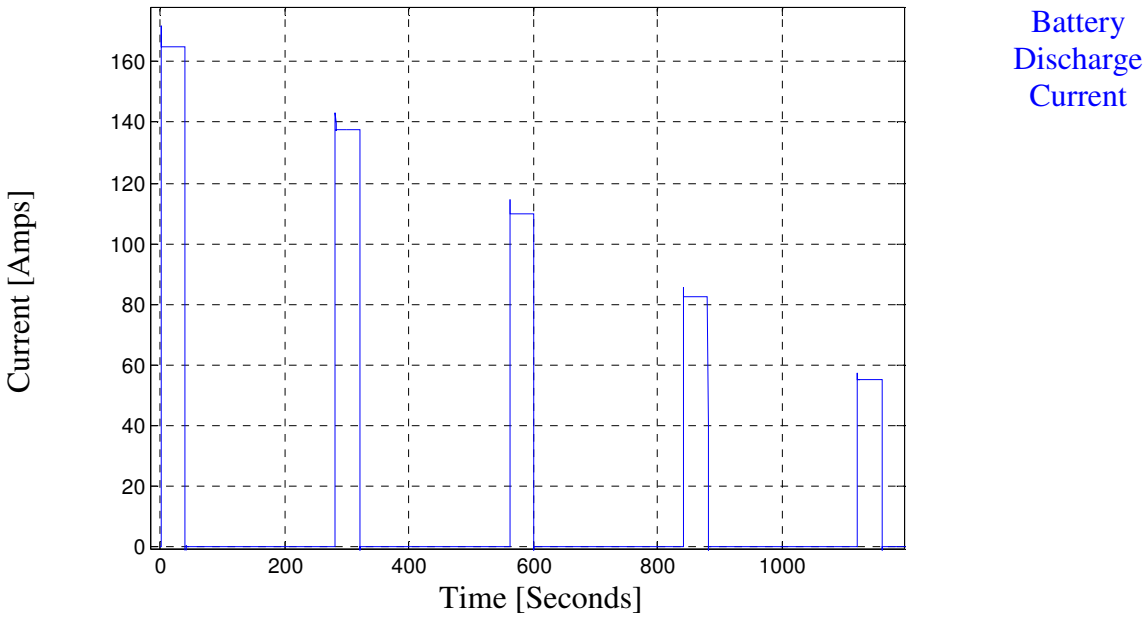

Fig. 3-26 Battery Pulse Discharge Profile

drop vs. current relationship. The current magnitudes are 1 C, 1.5 C, 2 C, 2.5 C, and 3 C. Recall that the battery rated capacity is 55 Amp-hours. The measured battery voltage

response for a current pulse is shown in Fig. 3-27 and the responses attributed to R_0 and R_1 are identified in red and green circles, respectively.

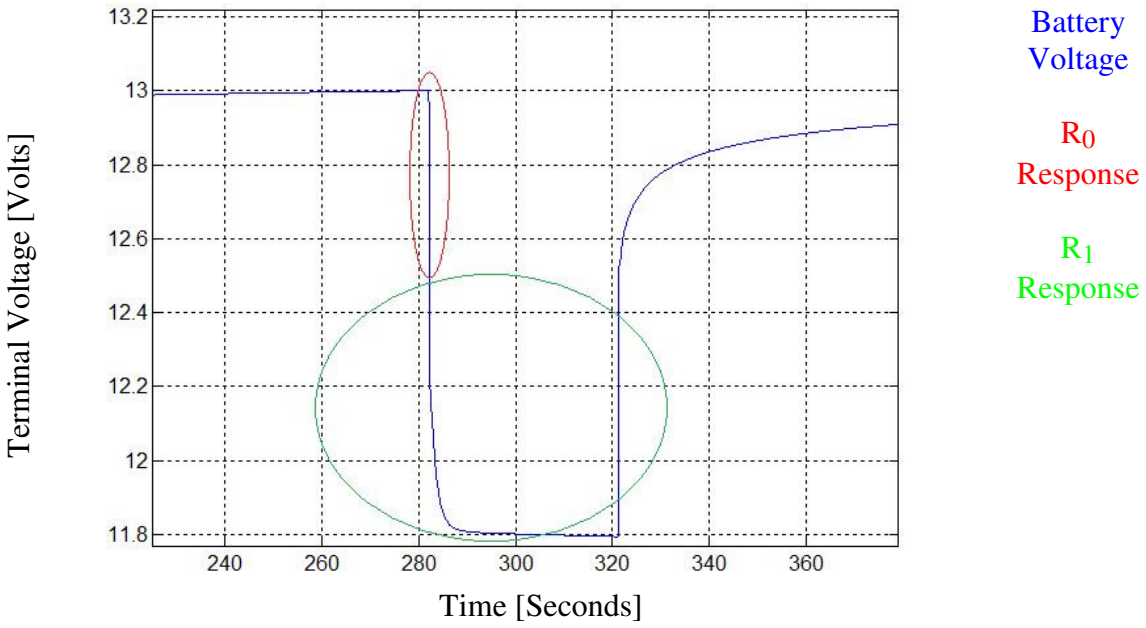

Fig. 3-27 Battery Pulse Discharge Voltage Response

The segmentation of the voltage response attributed to R_0 and R_1 is based on the fact that R_0 represents instantaneous change to voltage upon a current change. With the current quantity known and the voltage response attributed to R_1 identified, the value of R_1 can be estimated.

$$R_1 = \frac{\hat{v}_{R1}}{I} \tag{3.24}$$

The resulting estimated R_1 for the various current magnitudes are shown in Fig. 3-28.

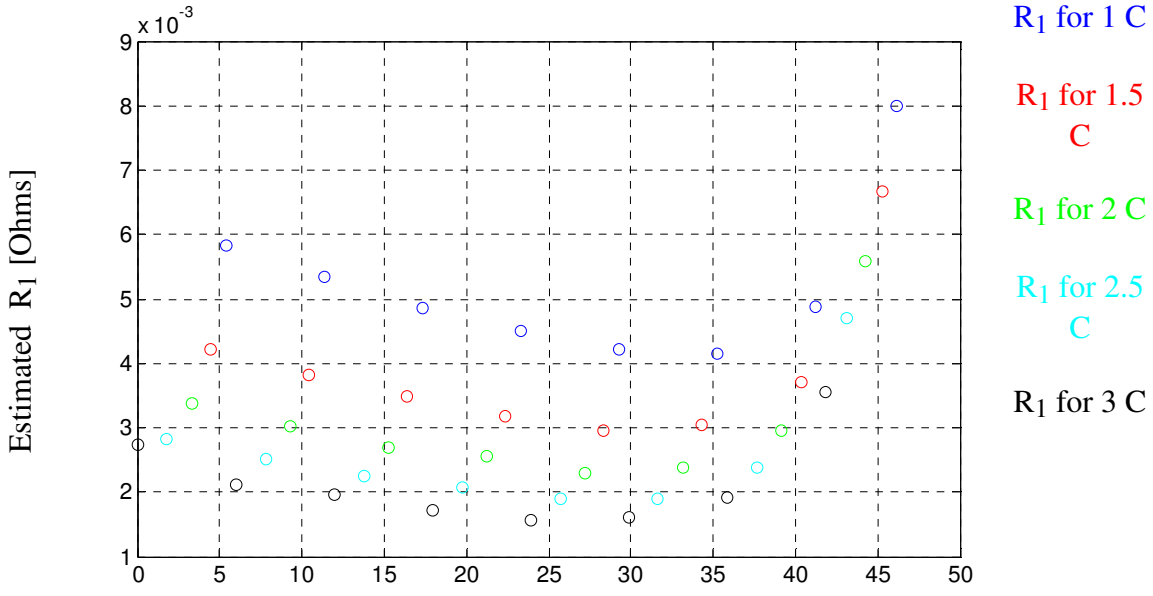

Fig. 3-28 Estimated R_1 from the Pulse Current Profile

For the 2 C (i.e. 110 Amps) current pulses, the average estimated R_1 is found to be 0.0031 Ohms. This current is close to the 120 Amps of interest for the maximum current in the EPA driving cycle. Now, it is possible to redraw Fig. 3-25 with the model-estimated R_1 replaced with the average estimated R_1 from the 2 C current pulses using the measured battery response to large current pulses.

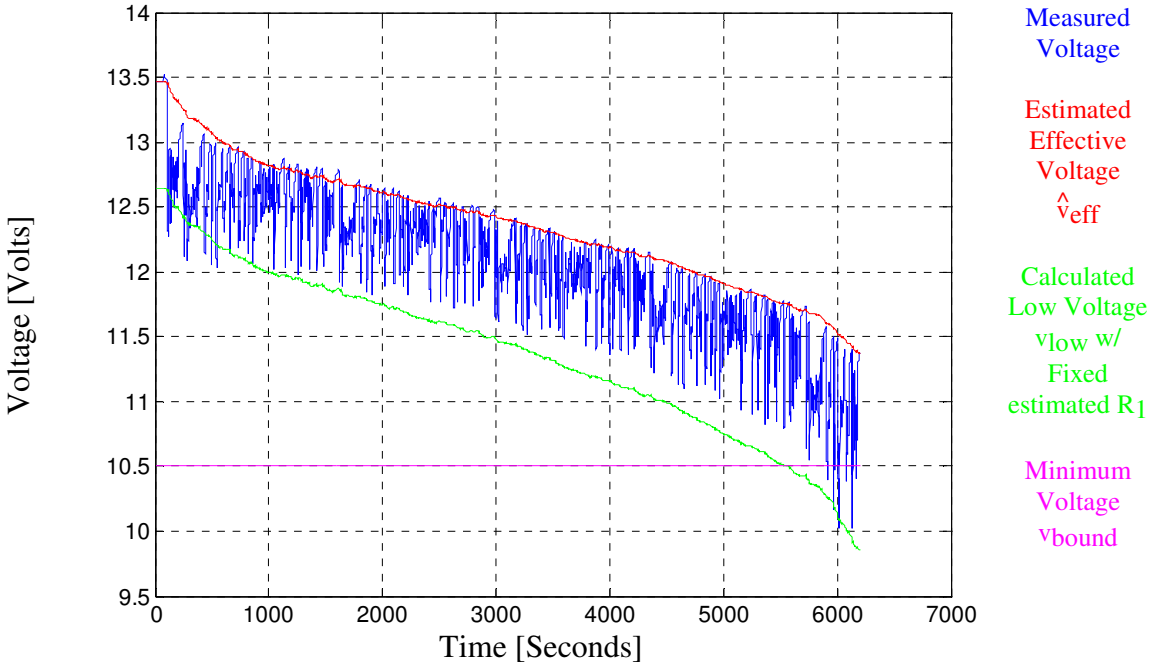

Fig. 3-29 Modified Calculated Low Voltage v_{low} vs. the Measured Voltage

Fig. 3-29 shows a much better performance for long-term power capability prediction than Fig. 3-25. This result is promising in that a method that incorporates the nonlinear nature of the battery in the model along with the ability to constantly update the parameters will be very instrumental for providing battery prognostics on power and available energy.

3.5 The Case Study of the Relative SOH for Batteries onboard the WEMPEC Corbin Sparrow

While the detection of SOH requires a controlled experiment environment such that the lengths of discharge before the cut-off voltage is reached can be compared, the relative health can still be observed based on the impedance. The reasoning should be intuitive since higher impedance translates into an early end of discharge for the same discharge current and cut-off voltage.

The WEMPEC Corbin Sparrow vehicle utilizes thirteen OPTIMA D34M batteries in series. Every two batteries in the bank are balanced by a commercial equalizer unit with respect to their terminal voltages. Despite the external balancing and the batteries being the same product, the performance of each battery still varies due to manufacturing variability, potentially different manufacture dates, and different local environments for each battery onboard the electric vehicle.

Since the batteries onboard the vehicle are arranged in a series configuration and the terminal voltages are being monitored for each of the batteries, the weakest of all the batteries in the bank becomes the limiting unit for the whole bank's performance. Thus, detection of the health of the batteries in series and the use of the information as a reference for replacement would serve to maintain the battery bank performance.

Fig. 3-30 shows the estimated R_0's using the proposed model for several batteries in the Corbin Sparrow battery bank. The estimates clearly show that Battery #5 is the weakest unit on a relative basis.

As indicated by Fig. 3-30, it will be natural to suspect that Battery #5 also has the highest drop in terminal voltage during the trip. The estimated R_0 values decrease slightly during the first 15 Amp-hours of discharge due to model convergence issues and diffusion effects. However, Battery #5 clearly exhibits a higher R_0 estimate than the other batteries throughout most of the trip, with the deviation increases near the end of the test. Fig. 3-31 shows the voltages for these batteries during a segment of the road trip and clearly confirms the suspicion on Battery #5's strength.

While the waveforms in Fig. 3-31 provide the information needed to identify Battery #5 as the weakest of the units in the bank, the system identification-based

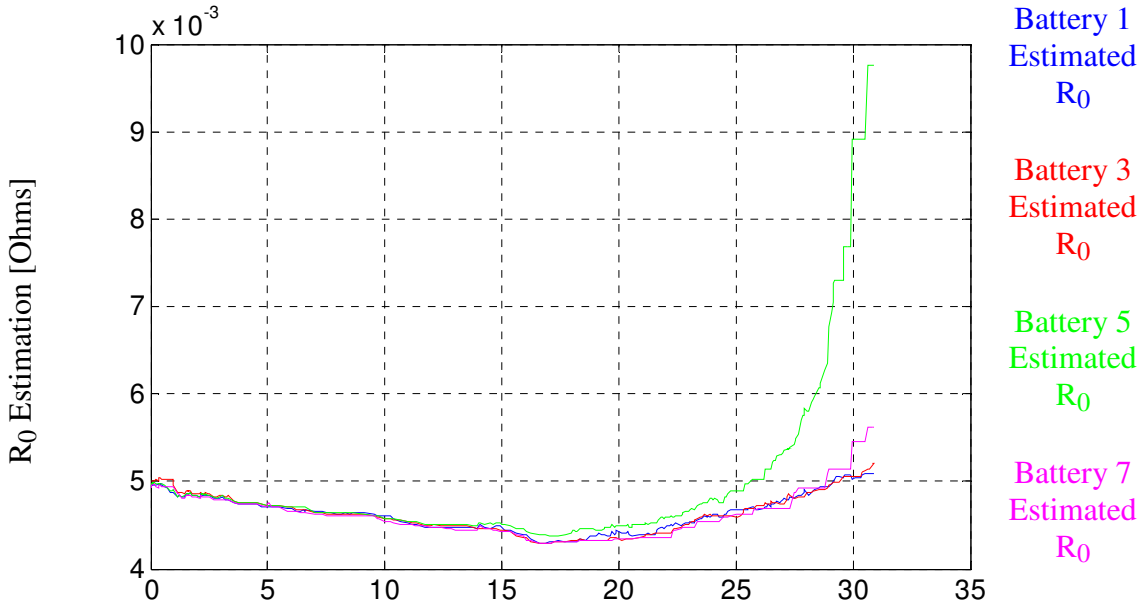

Fig. 3-30 R_0 Estimation for Four Batteries in the Corbin Sparrow Battery Pack Based on Measured Data for a Road Cycle Test

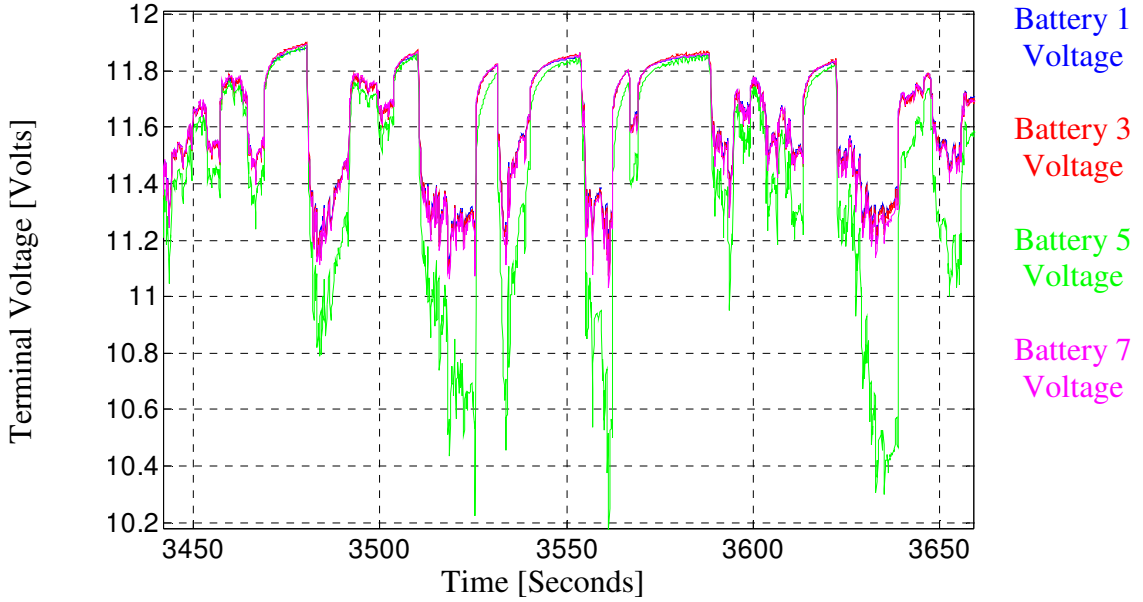

Fig. 3-31 Measured Terminal Voltages for Four Batteries in the Corbin Sparrow Battery Pack Near the End of the Road Cycle

estimation shown in Fig. 3-30 provides a useful means of quantifying this condition. The estimated R_0 value provides a promising means to diagnosing the relative SOH of each battery unit.

3.6 Summary

This chapter demonstrates the application of the developed model for SOF prediction. It also compares the pros and cons of the proposed model versus the spectral separation approach adopted in [9]. In addition, the chapter has discussed an important limitation of the system identification technique, namely that the method is a numerical algorithm that is not guaranteed to deliver battery parameters that always make physical sense. It is up to the user to make intelligent choices on which results to accept or reject.

Overall, the impedance information of the battery should be considered as part of the criteria for the evaluation of the battery capability, instead of the traditional SOC approach that completely ignores impedance and its power capability implications. This chapter serves the purpose of reminding the reader of the potential use of the impedance information in practical battery applications.

It has also been shown that the linear approach adopted by the proposed model has a significant drawback in terms of adapting to the high-current region, causing prediction errors in power capability that are too conservative. Further work remains to develop a nonlinear model that captures the battery dynamics that the system identification algorithm can use to adjust quickly to changes in battery parameters.

Chapter 4

Conclusions

This thesis presents a system identification-based battery model for BMS. The proposed method can be implemented in an EV application and provides the user information such as SOC estimation and power capability prediction. In addition, the application of the proposed method for SOH determination using the impedance estimation has been studied in this research project. The information on SOC and impedance changes over the course of multiple cycles can also be used to infer useful SOH information for an experienced battery user.

4.1 Summary of Contributions

The primary contributions of this project are summarized as follows:

1. A thorough state-of-the-art review of BMS technologies to provide SOC, SOH, and SOF information for the user has been conducted.
2. A methodology has been proposed for delivering internal battery state estimates that is based on prior art and adaptation for the EV application. The methodology has the option of utilizing a new, offline approach for estimating the diffusion voltage component to reduce the bias on the OCV and SOC estimation. The OCV/SOC prediction performance of the proposed method

has been experimentally tested and compared with the baseline coulomb counting method.

3. The thesis provides detailed discussions of the limitations of the proposed method for battery state estimation, including the effects of initial parameter guesses, sampling frequency, inconsistent charging algorithm, unrealistic parameters obtained through system identification, and the potential update dynamic oscillation for the spectral separation method used in prior art [9].
4. System identification modifications to deal with physical parameters of the R-RC circuit have been explored in this document. While the mathematics has been worked out, the computational complexity is deemed too high for the benefits that the modifications yield.
5. The proposed method's ability to identify weak battery modules has been demonstrated using road data from a experimental EV. The relative SOH of each battery module can be observed from the estimated impedance information.
6. The model's ability to perform short-term SOF has been demonstrated. With the equivalent circuit and its adapted parameters, the model can simulate the current load and determine if the minimum terminal voltage limit will be violated.
7. An approach to combining SOC estimation and long-term power capability prediction has been evaluated in this thesis. The limitations of the proposed linear circuit-based system have been identified and demonstrated, i.e., its adaptation is operating point-based. While the results indicate limited

usefulness of the proposed battery model in its current form for long-term power capability prediction, the potential effectiveness of adopting a nonlinear model has been demonstrated using a simplified offline approximation.

8. A bidirectional, full power rated, automated test stand has been constructed for automotive-purpose battery module.

4.2 Avenues for Further Research

During the project, many other possible improvements to the proposed method were considered. The major focus was to find a system identification model or technique more suitable for the online battery monitoring application. In particular, a combined estimation model without the $\hat{v}_{eff}$ component, i.e. strict equivalent RC circuit without source, was attempted, but it was found that the sampling time required to accommodate the slower dynamics is too large. The lattice filter technique for updating parameters was also attempted, and it was found that the lattice filter technique, while having a desirable stability property, does not adequately update the increase of R_0 during discharge.

A better understanding of the theory and limitations of various system identification techniques is required to improve the battery internal state estimation. Specifically, the least squared error method is known to be biased in the presence of non-Gaussian white noise. Additional modeling effort focused on the error/residuals could help the estimated parameters to be less biased.

In addition, the nonlinear nature of the charge transfer resistance demands the formulation of a nonlinear model based on the Butler-Volmer equation, (1.4) or (1.5). It was demonstrated in Chapter Three that the traditional linear circuit model takes time to adjust to the nonlinearity with respect to current magnitude, causing significant modeling

error. It would be desirable to improve the method to include this nonlinear relationship between the charge transfer voltage and current in the model, and a crude offline approximation was attempted in Chapter Three with promising results.

The double-layer capacitance is also known for its high nonlinearity, for which further advances in battery transient behavior modeling are still needed. A stretched exponential method was considered for the transient nonlinearity modeling, but it suffers from z-transform domain implementation difficulties.

The diffusion model proposed in this thesis is somewhat restricted to the EV operating cycle that has been the focus of this research program. The method makes assumptions about the charging algorithm and discharging profile features. A more universal model for diffusion could be an avenue for further research.

Implementation of the proposed battery state estimation method or other alternative methods on the WEMPEC experimental electric vehicle (a Corbin Sparrow) is needed for field testing of these techniques. Road experience would provide deep insight into the accuracy of the model and how best to integrate the information provided by the model in a user-friendly interface.

On a higher level, however, the author feels that much of the linear circuit model-based applications of BMS have already been explored in the literature. Perhaps a better understanding on the chemistry of the battery, i.e., improved knowledge leading to more suitable modeling structures, is the key to achieving further advances.

Bibliography

[1] Henk Jan Bergveld, Wanda S. Kruijt, and Peter H.L. Notten, "Battery Management Systems, Design by Modelling" Kluwer Academic Publishers, 2002.

[2] B.B. Battery, BP5-12, datasheet, as of 8/30/2009.
Website: http://www.bb-battery.com/productpages/BP/BP5-12.pdf

[3] Lead-Acid Batteries, as of 8/30/2009.
Website: http://hyperphysics.phy-astr.gsu.edu/Hbase/electric/leadacid.html#c2

[4] Corrosion Doctors, as of 8/30/2009.
Website: http://corrosion-doctors.org/Biographies/PlantelBio.htm

[5] Battery Types: Flooded vs. AGM and Gel, as of 8/30/2009.
Website: http://www.vonwentzel.net/Battery/01.Type/index.html

[6] Nickel Cells-How they work, as of 8/30/2009
Website: http://www.batterieswholesale.com/nickel_cell_how_it_works.htm

[7] Gold Peak Industries (Taiwan) Ltd, "Lithium Ion, Technical Handbook", as of 8/30/2009
Website: http://www.gpbatteries.com/html/pdf/Li-ion_handbook.pdf

[8] Doron Aurbach, "Review of selected electrode-solution interactions which determine the performance of Li and Li ion batteries", Journal of Power Sources 89 (2000) 206-218

[9] H. L. N. Wiegman, "Battery State Estimation and Control For Power Buffering Applications", 1999

[10] Sabine Piller, Marion Perrin, and Andreas Jossen, "Methods for State of Charge Determination and Their Applications", Journal of Power Sources 96 (2001) 113-120

[11] M. Coleman, C.K. Lee, W.G. Hurley, "State of Health Determination: Two Pulse Load Test for a VRLA Battery", Power Electronics Specialists Conference, 2006. PESC '06. 37th IEEE

[12] E. Karden, “Using Low-Frequency Impedance Spectroscopy for Characterization, Monitoring, and Modeling of Industrial Batteries”, February, 2001

[13] Koray Kutluay, Yigit Cadirci, Yakup S. Ozkazanc, and Isik Cadirci, “A New Online State-of-Charge Estimation and Monitoring System for Sealed Lead-Acid Batteries in Telecommunication Power Supplies,” IEEE Transactions on Industrial Electronics, October 2005.

[14] O. Caumont, P. Le Moigne, C Rombaut, X. Munerret, and P. Lenain, “Energy Gauge for Lead-Acid Batteries in Electric Vehicles,” IEEE Transactions on Energy Conversion, Vol. 15, No. 3, September 2000

[15] Takayuki Torikai, Takaaki Takesue, Yukihiro Toyota, and Kazushi Nakano, “Research and Development of the Model-Based Battery State of Charge Indicator,” IEEE, 1992

[16] Shriram Santhanagopalan, Ralph E. White, “Online Estimate of the State of Charge of a Lithium Ion Cell”, Journal of Power Sources 161 (2006) 1346-1355

[17] F. Huet, R.P. Nogueira, L. Torcheuz, P. Lailler, “Simultaneous real-time measurements of potential and high frequency resistance of a lab cell”, Journal of Power Sources 113 (2003) 414-421

[18] H. Blanke, O Bohlen, S Buller, R W. De Doncker, B. Fricke, A. Hammouche, D. Linzen, M. Thele, and D. U. Sauer, “Impedance measurements of lead-acid batteries for state-of-charge, state-of-health and cranking capability prognosis in electric and hybrid electric vehicles” Journal of Power Sources 144 (2005) 418-425.

[19] A. Hammouche, E. Karden, and R W. De Doncker, “Monitoring state-of-charge of Ni-MH and Ni-Cd batteries using impedance spectroscopy,” Journal of Power Sources 127 (2004) 105-111.

[20] M. Hughes, R.T. Barton, S.A.G.R. Karunathilaka, N. A. Hampson, and R. Leek, “The Residual Capacity Estimation of Fully Sealed 25 Ah Lead/Acid Cells,” Journal of Power Sources, 17 (1986) 305-329.

[21] F. Huet, “A review of impedance measurements for determination of the state-of-charge or state-of-health of secondary batteries,” Journal of Power Sources 70 (1998) 59-69

[22] F. Huet, R.P. Nogueira, P. Lailler, L. Torcheux, “Investigation of the high frequency resistance of a lead-acid battery”, Journal of Power Sources 158 (2006) 1012-1018.

[23] M. Coleman, C. K. Lee, C. Zhu, and W. G. Hurley, "State-of-Charge Determination from EMF Voltage Estimation: Using Impedance, Terminal Voltage, and Current for Lead-Acid and Lithium-Ion Batteries," IEEE Transactions on Industrial Electronics, Vol. 54, No. 5, October 2007.

[24] Gregory L. Plett, "Extended Kalman filtering for battery management systems of LiPB-based HEV battery packs Part 1. Backfround," Journal of Power Sources 134 (2004) 252-261.

[25] Gregory L. Plett, "Extended Kalman filtering for battery management systems of LiPB-based HEV battery packs Part 2. Modeling and identification," Journal of Power Sources 134 (2004) 262-276.

[26] Gregory L. Plett, "Extended Kalman filtering for battery management systems of LiPB-based HEV battery packs Part 3. State and parameter estimation," Journal of Power Sources 134 (2004) 277-292.

[27] B. S. Bhaugu, P. Bentley, D. A. Stone, and C. M. Bingham, "Nonlinear Observers for Predicting State-of-Charge and State-of-Health of Lead-Acid Batteries for Hybrid-Electric Vehicles," IEEE Transactions on Vehicular Technology, Vol. 54, No. 3, May 2005.

[28] Jaehyun Han, Dongchul Kim, and Myoungho Sunwoo, "State-of-charge estimation of lead-acid batteries using an adaptive extended Kalman filter," Journal of Power Sources 188 (2009) 606-612

[29] Seongjun Lee, Jonghoon Kim, Jaemoon Lee, and B.H. Cho, "State-of-charge and capacity estimation of lithium-ion battery using a new open-circuit voltage versus state-of-charge," Journal of Power Sources 185 (2008) 1367-1373.

[30] Jaemoon Lee, Oanyong Nam, and B.H. Cho, "Li-ion battery SOC estimation method based on the reduced order extended Kalman filtering," Jourla of Power Sources 174 (2007) 9-15.

[31] Jaemoon Lee, Jaeho Lee, Onyong Nam, Jonghun Kim, and B. H. Cho, "Modeling and Real Time Esimation of Lumped Equivalent Circuit Model of a Lithium Ion Battery," EPE-PEMC 2006, Portoroz, Slovenia.

[32] D. T. Lee, S. J. Shian, C. M. Lee, and Y. C. Wang, "State-of-Charge Estimation for Electric Scooters by Using Learning Mechanisms," IEEE transactions on Vehicular Technology, Vol. 56, No. 2, March 2007.

[33] C. C. Hua, T. Y. Tasi, C. W. Chuang, and W. B. Shr, "Design and Implementation of a Residual Capacity Estimator for Lead-Acid Batteries," Second IEEE Conference of Industrial Electronics and Applications, 2007.

[34] S. Drouilhet and B.L. Johnson, "A Battery Life Prediction Method for Hybrid Power Applications", website address: http://www.nrel.gov/docs/legosti/fy97/21978.pdf

[35] Kazuhiko Takeno, Masahiro Ichimura, Kazuo Takano, and Junichi Yamaki, "Influence of cycle capacity deterioration and storage capacity deterioration on Li-ion batteries used in mobile phones," Journal of Power Sources 142 (2005) 298-305.

[36] M. Wu, P. J. Chiang, "High-rate capability of lithium-ion batteries after storing at elevated temperature", Electrochimica Acta 52 (2007) 3719-3725.

[37] Jaworski, "Effects of Nonlinearity of Arrenius Equation on Predictions of Time to Failure for Batteries Exposed to Fluctuating Temperatures", 1998 IEEE

[38] U Troltzsch, O. Kanoun, and H. Trankler, "Characterizing aging effects of lithium ion batteries by impedance spectroscopy", Electrochimica Acta 51 (2006) 1664-1672

[39] M. Broussely, S. Herreyre, P. Biensan, P. Kasztejna, K. Necheb, and R. J. Staniewicz, "Aging mechanism in Li ion cells and calendar life predictions," Journal of Power Sources 97-98 (2001) 13-21.

[40] M. Wohlfahrt-Mehrens, C. Vogler, and J. Garche, "Aging mechanisms of lithium cathode materials," Journal of Power Sources 127 (2004) 58-64.

[41] T. Osaka, S. Nakade, M. Rajamaki, and T. Momma, "Influence of capacity fading on commercial lithium-ion battery impedance," Journal of Power Sources 119-121 (2003) 929-933.

[42] D. U. Sauer, Heinz Wenzl, "Comparison of different approaches for lifetime prediction of electrochemical systems-Using lead-acid batteries as example," Journal of Power Sources 176 (2008) 534-546.

[43] S. W. Eom, M. K. Kim, I. J. Kim, S. I. Moon, Y. K. Sun, and H. S. Kim, "Life prediction and reliability assessment of lithium secondary batteries," Journal of Power Sources 174 (2007) 954-958.

[44] L. Serrao, Z Chehab, Y. Guezennec, and G. Rizzoni, "An Aging Model of Ni-MH Batteries for Hybrid Electric Vehicles," IEEE 2005.

[45] P. J. van Bree, A. Veltman, W. H. A. Hendrix, and P. R. J. van den Bosch, "Prediction of Battery Behavior Subject to High-Rate Partial State of Charge," IEEE Transactions on Vehicular Technology, Vol. 58, No. 2, February 2009.

[46] Keizo Yamada, Yoshifumi Yamada, Koji Otsu, Yoshiaki Machiyama, Akihiko Emori, and Teturo Okoshi, "The intelligent automotive battery, "CYBOX"," Journal of Power Sources 185 (2008) 1478-1483.

[47] Bramwell, "Vehicle Starting Battery Cold-Cranking Amps Meter and Method," U.S. Patent 6,097,193, August, 2000.

[48] S. Buller, M. Thele, E. Karden, and R.W. De Doncker, "Impedance-based non-linear dynamic battery modeling for automotive applications," Journal of Power Sources 113 (2003) 422-430.

[49] G. F. Franklin, J. D. Powell, and M. L. Workman, "Digital Control of Dynamic Systems," 2nd edition, ISBN 0-201-11938-2, Addison-Wesley Publishing Company, 1990.

[50] Dynamometer Driver's Aid | Testing & Measuring Emissions | US EPA, as of 8/30/2009
Website: http://www.epa.gov/nvfel/testing/dynamometer.htm

[51] A. Delaille, M. Perrin, F. Huet, and L. Hernout, "Study of the 'Coup de Fouet' of lead-acid cells as a function of their state-of-charge and state-of-health" Journal of Power Sources 158 (2006) 1019-1028.

Appendix A

EPA Driving Cycle

The U.S. Environmental Protection Agency (EPA) has published multiple vehicle driving cycles. One of these is the EPA urban dynamometer driving schedule (UDDS) [50]. The following figure shows the urban driving cycle expressed in terms of speed [mph] vs. time [Seconds] .

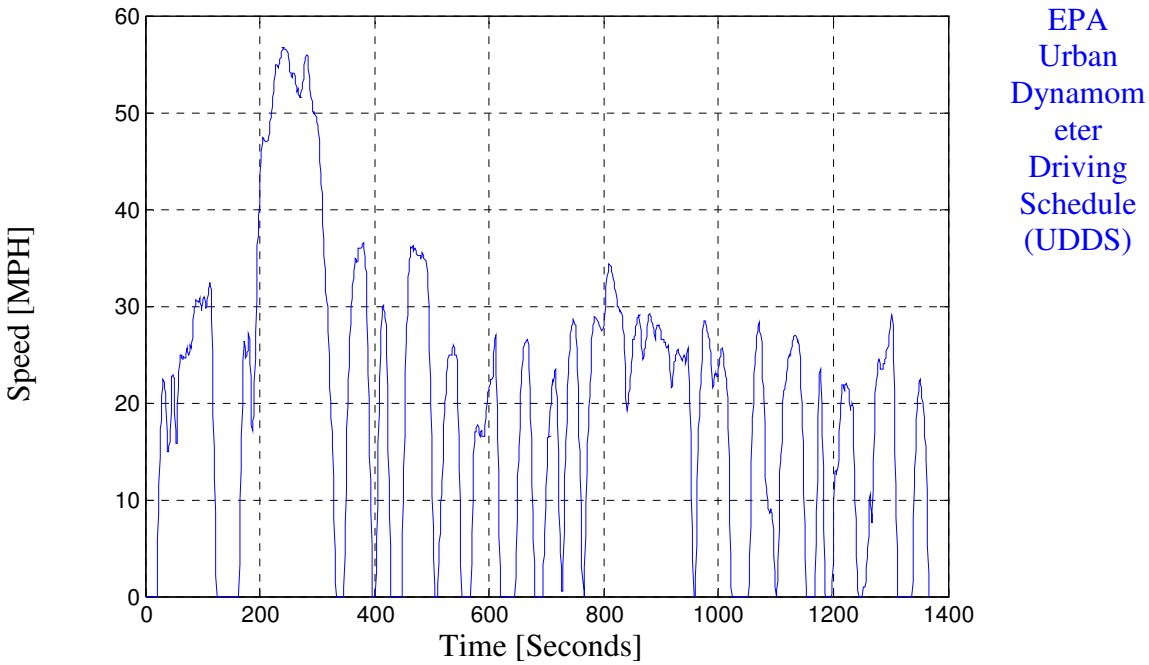

Fig. A $1R_0$ Estimation for the Model without Diffusion Component for Square Wave Driving Cycle

Since the EPA provides the data in the above figure at a 1 Hz rate, it is possible to find the acceleration of the vehicle at a 1 Hz rate by taking the slope between two samples. As the units [MPH per second] does not have direct relevance to the battery

under test, this document will normalize the peak of the acceleration as 1 per unit. Note that, in an electric vehicle, the acceleration is almost proportional to torque, which in turn is roughly proportional to battery current. Thus, the normalization of the acceleration can be seen as a normalization of battery current output. Also, since the experiments are concerned with only discharging the battery and the assumptions are that the electric vehicle has no brake regeneration capability, the negative portion of the current profile will be changed to zero.

In addition, linear approximation is used to increase the sampling rate of the normalized current waveform to 10 Hz, which will be the sampling rate at which the experiments are conducted. A one percent random noise is also superimposed to every sample in order to mimic the actual vehicle battery condition as well as to satisfy the system identification excitation frequency content requirement. The result is shown in the following figure.

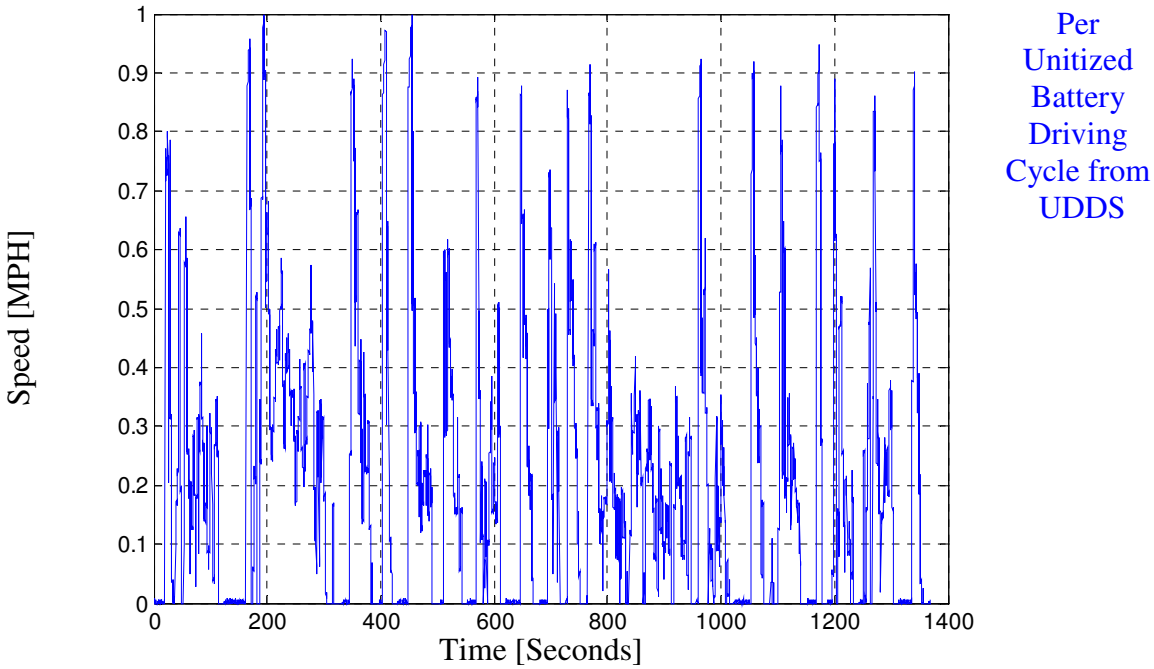

Fig. A 2 Battery Driving Cycle Scaled from the Derivative of the EPA Urban Driving Cycle

Since the battery characteristics are being measured with application to the Corbin Sparrow in mind, the final scaling of the driving cycle in Fig. A 2 is achieved by determining what base current value will yield efficiency closest to that of the Corbin Sparrow road data, i.e., to match the EPA driving cycle with the Corbin Sparrow in terms of scaling. The road data are not included here, but the base value for the current is chosen as 120 Amps. Based on the rated battery pack voltage of 156 Volts, the battery calculated efficiency is 196.3 $[\frac{\text{Wh}}{\text{Miles}}]$ close to the trip calculated 188 $[\frac{\text{Wh}}{\text{Miles}}]$ for the actual Corbin Sparrow based on collected test data.

Appendix B

Experimental Set Up

The automated battery utilizes a Chroma 63201 programmable electronic load in parallel with a Chroma 62024 programmable power supply. The important system specifications are outlined in the following table.

Table B 1 High Bandwidth, High Accuracy Battery Test System Specifications

Max battery pack voltage	40V
Max charge current/power	120A/2.4kW
Max discharge current/power	300A/2.6kW
Voltage sensing accuracy (sense lines for up to four batteries)	5mV Accuracy Guaranteed
Current sensing accuracy	about 100mA
Alias Free Bandwidth	3.5kHz

The power supply and load are controlled by a National Instruments CompactRIO Microcontroller/FPGA, which also performs the signal acquisition and data logging. Multiple relays are set up at strategic locations and are controlled by the CompactRIO. Fig. B 1is the system diagram.

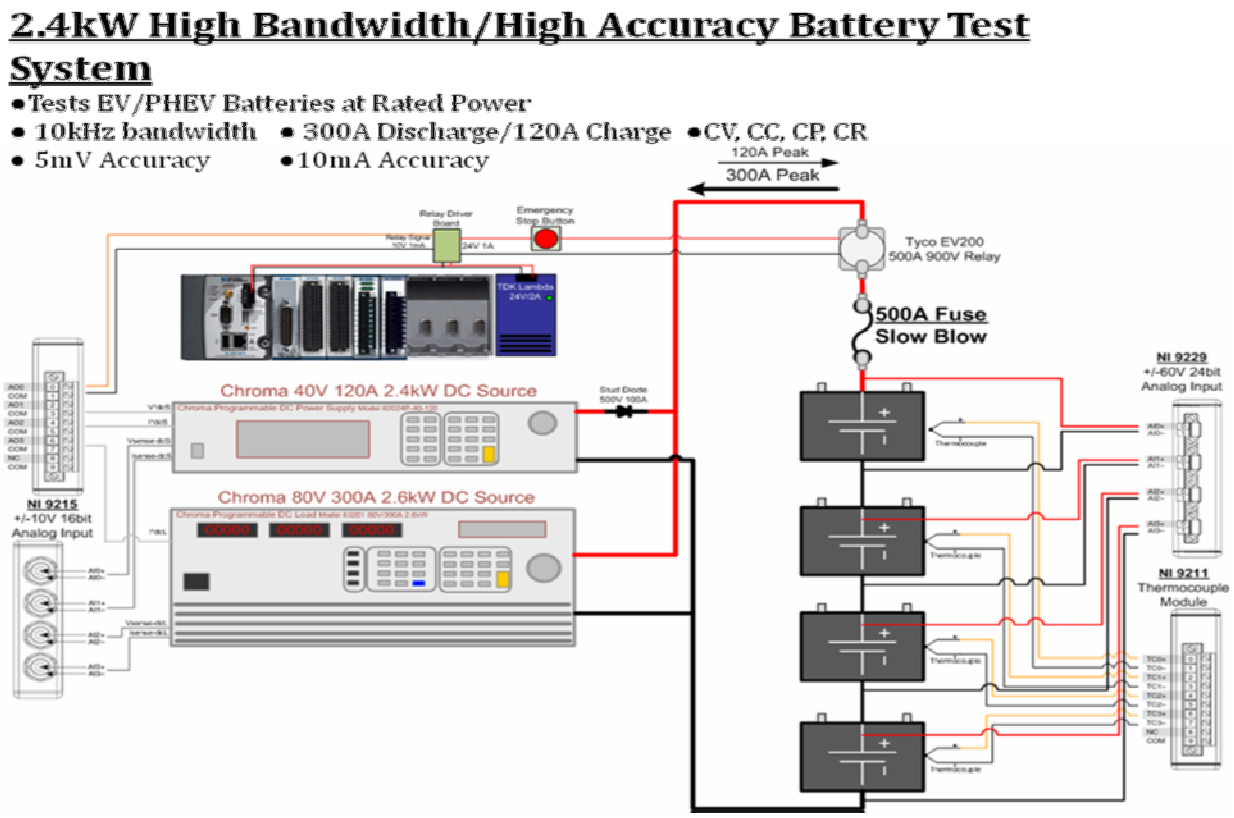

Fig. B 1 Experimental Hardware Set Up

The system control software is written in LabVIEW. Two main user interfaces exist for programming the desired battery current profile, controller and automation program interface. The controller interface provides an environment to manually set up the battery activities while providing real-time system monitoring information on a visual panel. The following diagram is a snapshot of the controller interface.

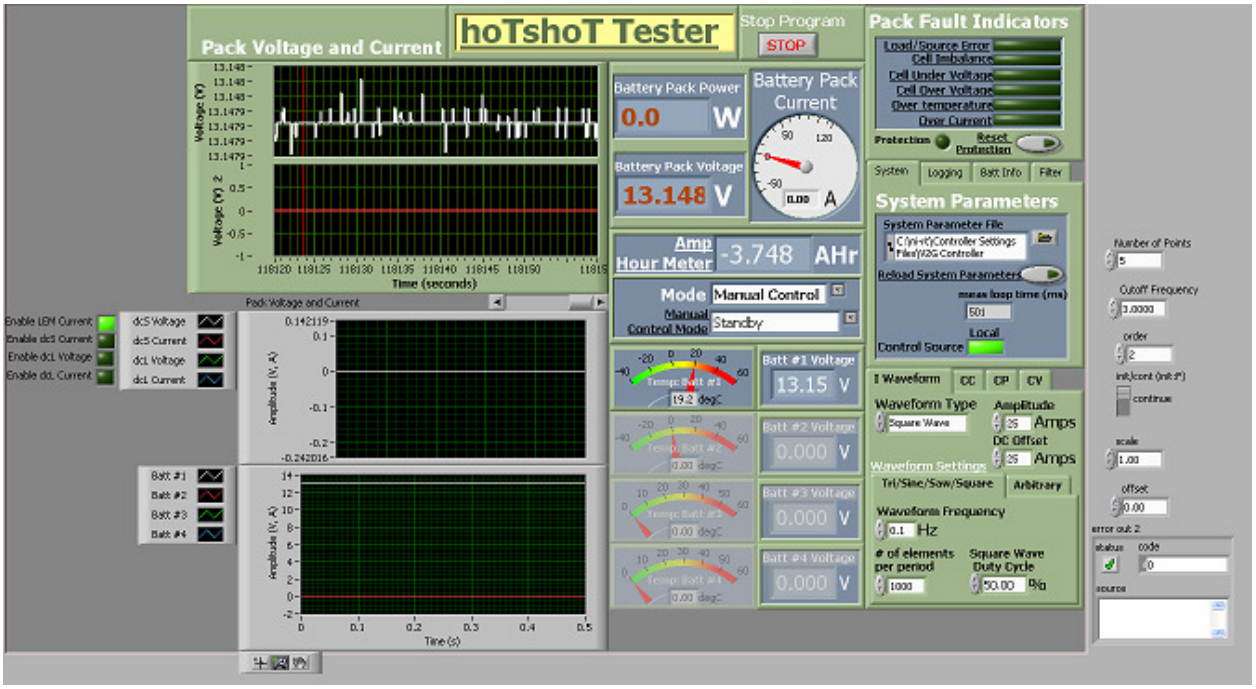

Fig. B 2 Snap Shot of System Controller Interface

As seen in Fig. B 2, the interface provides information on battery pack current, voltage, and temperature. The command modes available for the battery current are listed in Table B 2.

Table B 2 Command Modes Available in System Controller Interface

Command Mode	Description
Standby	The relays are off, including the supply/load sensor relays to prevent unintended current flow. The current sensor is zeroed to minimize offset.
Constant Current	The battery bank supplies or absorbs a fixed amount of current, as long as the voltage limits and other protection constraints are satisfied.
Constant Voltage	The power supply provides a current at a fixed voltage, so long as the current limits and other protection constraints are satisfied.
Constant Power	The load has a CP mode while the supply relies on a proportional power control written in LabVIEW.
Current Waveform	The waveform generator can produce sine, square, triangle, and sawtooth waves. In addition, the user can upload a waveform pattern for any arbitrary waveform command.

To ensure safety, the automated battery testing system actively monitors the battery bank and terminates the operation if any of the pre set conditions are met. Specifically, the following table lists the constraints that the system monitors.

Table B 3 System Monitored Error Conditions

Monitored Condition	Description
Load/Source Error	The program regularly pings the load and source to make sure they are online and functional.
Cell Under Voltage	Checks if any of the cells is below the minimally acceptable cell voltage.
Cell Over Voltage	Checks if any of the cells is above the maximum cell voltage.
Over Temperature	Checks if any of the cells is above the maximum temperature.
Over Current	Activates if the battery current is above the pre-set level.

In addition, the controller interface includes some miscellaneous settings that allow the user to provide information to the system about the battery pack, sampling frequency, etc.

Table B 4 System Controller Miscellaneous Settings

Settings	Description
System	Informs the program the location for the battery information file. Also specifies the least time the main loop will take in the program.
Logging	Specifies the data log's name and location
Battery Info	Displays the battery information from the information file.
Filter	Specifies the data logging properties, including samples per channel, decimation factor, and anti-alias filter frequency.

While the controller interface provides all the functionalities for performing battery tests, the system comes with an automation program interface for automated testing. A snap shot of the automation program interface is included here.

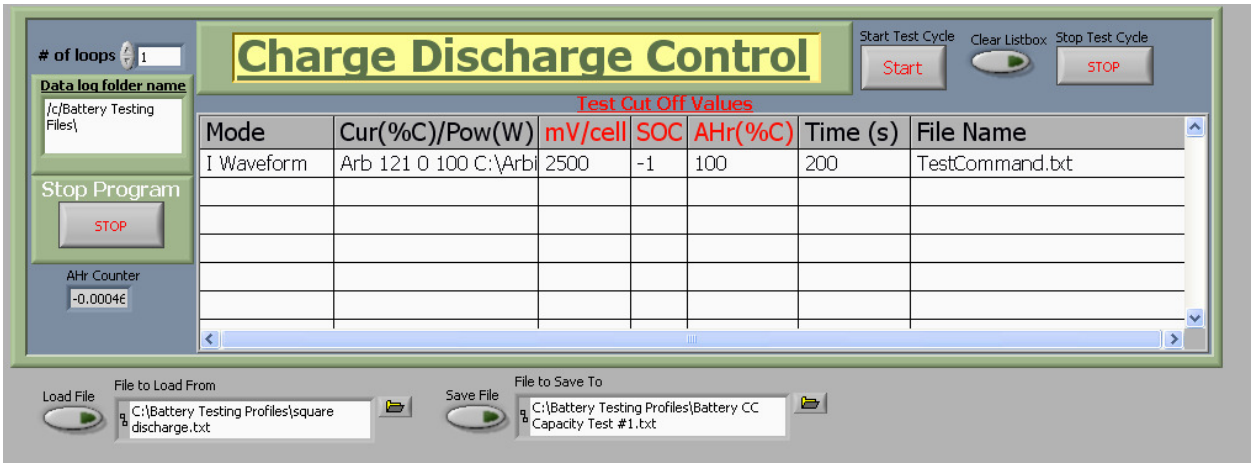

Fig. B 3 Snapshot of the Automated Testing Programming Interface

The automation program interface can load a text file written in a certain format and interpret it for commands requested by the user. Table B 5 is a guide to what values the automation program interface expects for various modes available.

Table B 5 Commands Available For Automatic Testing Programming

Mode	Cur/Pow	Cutoff Volts/cell	Cutoff SOC	Cutoff Ah	Timeout(s)	File Name
Full Charge	X	X	X	X	Max time	File Name
CC Charge	Charge Current	Max volts/cell	Max SOC	Max Ah In	Max time	File Name
CP Charge	Charge Power	Max volts/cell	Max SOC	Max Ah In	Max time	File Name
CV Charge	Charge Voltage	X	Max SOC	Max Ah In	Max time	File Name
CC Discharge	Discharge Current	Min volts/cell	Min SOC	Max Ah Out	Max time	File Name
CP Discharge	Discharge Power	Min volts/cell	Min SOC	Max Ah Out	Max time	File Name
I Waveform	Waveform Info	Max volts/cell, min volts/cell	Min SOC, Max SOC	Max Ah Out, Max Ah In	Max time	File Name
Pause	X	X	X	X	Max time	File Name
Log Once	X	X	X	X	X	File Name

The “Waveform Info” command for “I Waveform” mode is different depending on what waveforms are to be requested. Table B 6 lists the commands for each of the waveforms.

Table B 6 Available Options for Arbitrary Waveforms

Waveforms	**Commands**
Square	'Amplitude [Amps]' 'DC Offset [Amps]' 'Frequency [Hz]' 'Elements per Period' "Duty Cycle [%]"
Sine	'Amplitude [Amps]' 'DC Offset [Amps]' 'Frequency [Hz]' 'Elements per Period'
Sawtooth	'Amplitude [Amps]' 'DC Offset [Amps]' 'Frequency [Hz]' 'Elements per Period'
Triangle	'Amplitude [Amps]' 'DC Offset [Amps]' 'Frequency [Hz]' 'Elements per Period'
Arbitrary	'Amplitude [Amps]' 'DC Offset [Amps]' 'Update Frequency [Hz]' 'File path'

The battery information and default charging algorithm can be supplied to the program via an information gathering VI. Fig. B 4 is a snapshot of the battery information VI interface.

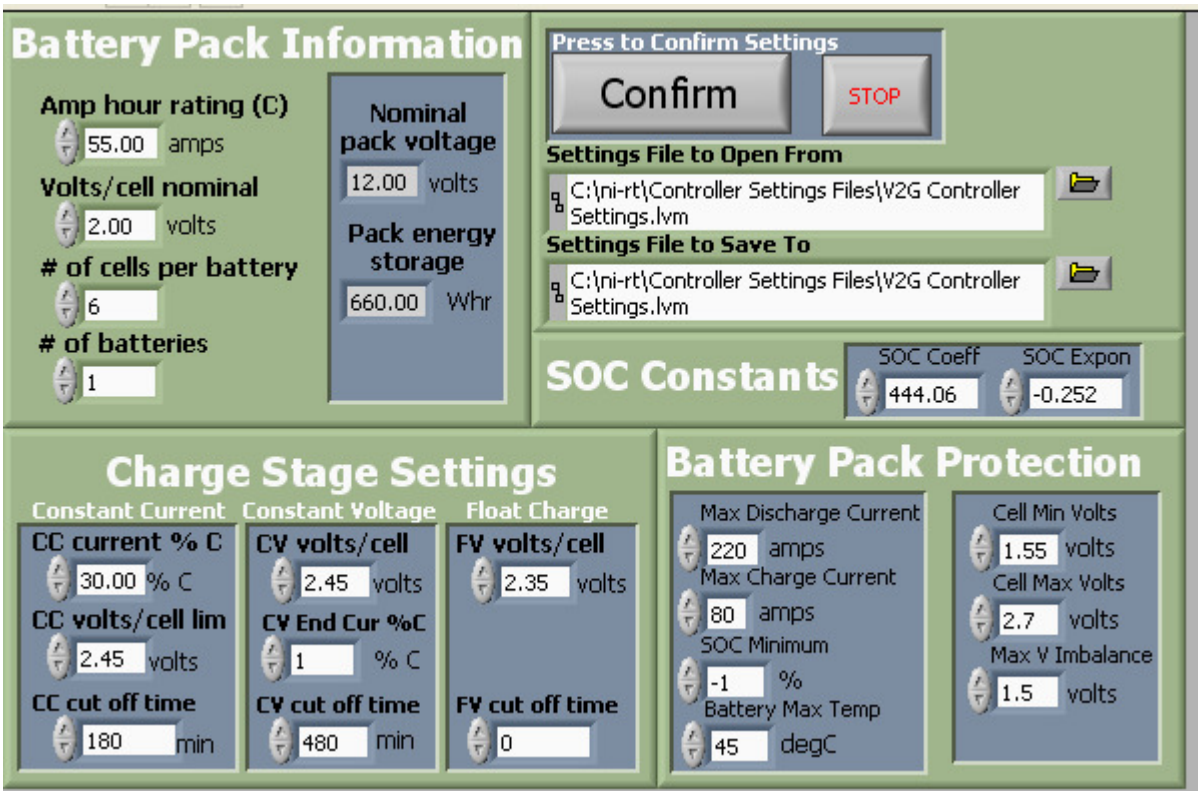

Fig. B 4 Interface of the Battery Information Gathering VI

As seen in the snapshot, the information gathered in the VI has three categories: battery pack information, charge stage settings, and battery pack protection. Table B 7 lists the detailed description of these settings.

Table B 7 Explanation of Entries in the Battery Information Gathering VI

Category	Setting	Description
Battery Pack Information	Amp Hour	The manufacturer provided rated capacity, usually at 20 hour rate
	Volt/Cell (Nominal)	The nominal rated voltage per cell in the battery module.
	# of Cells in Battery	As the name indicates.
	# of Batteries	As the name indicates.
Charge Stage Setting	Constant Current	The mode specifies the current rate in [%C], cut off maximum voltage per cell, and maximum time.
	Constant Voltage	The mode specifies the charging voltage per cell, cut off minimum current in [%C], and maximum time.
	Float Charge	The mode specifies the voltage at while the pack is connected to the supply, allowing passive balancing. The maximum time is also specified.
Battery Pack Protection	Voltage Limits	As the name indicates.
	Current Limits	As the name indicates.
	Maximum Temperature	As the name indicates.
	Maximum Voltage Inbalance	The maximum voltage difference allowed for the pack.
SOC Constants	SOC Constants	The coefficients for this specific battery's Peukert's modification power curve fit.

Appendix C

Matlab Code

The following is the example program code for the method with diffusion component modeled. The function for automatically initialize parameters called in this program is also included.

```
%*********************************************************
%This program does not incorporate the diffusion voltage
%effect. The "Vdc" is considered an effective
%voltage source that holds for a short (i.e. within tens of secs)
%period of time.  This particular version has seperated the frequency
%content of error signal for update.  This is a discrete-time based
%gradient method.  The forgetting factor on c can also be tuned.
%*********************************************************

clear all; close all; clc;

%% Initialize Data

load('Discharge')
I=data(:,3);                          %   Battery current data sampled at 10 Hz
V=data(:,2);                          %   Battery voltage data sampled at 10 Hz
T=0.1;                                %   Sampling Frequency
time=(0:T:(length(I)-1)*T)';          %   Initialize time array

%% Filter Setting

CutOff=0.1;                                %    [Hz], the frequency limit of the DC voltage
evolution
Tau=1/(CutOff);                       %   [Seconds]
W=2*(1/Tau)/(1/T);                    %   Discrete Frequency in 2*Omega
[n_ocv,d_ocv]=butter(1,W);            %   DC voltage filter set up
%[n,d]=butter(1,10*W);                %   Filter

%% Initialize Parameters

range=200/T;                          %   Sample range for auto init est.
[R0guess,R1guess,C1guess]...          %   Auto init est.
    =AutoParaInit(I,V,T,range);       %   [Farads], initial value for C1
b0=zeros(length(I),1);                      %    [], initialize the array for discrete TF
parameter
b1=zeros(length(I),1);                      %    [], initialize the array for discrete TF
parameter
f1=zeros(length(I),1);                      %    [], initialize the array for discrete TF
parameter
Vrc=zeros(length(I),1);                %    [Volts], initialize the arrary for KVL obtained
RC voltage
Vrc_hat=zeros(length(I),1);            %    [Volts], initialize the array for estimated RC
voltage
Vrc_ver=zeros(length(I),1);            %    [Volts], initialize the array for verification RC
voltage
Vrc_ver_test=zeros(length(I),1);
Vdc=zeros(length(I),1);               %   [Volts], initialize the dc voltage
Vdc_raw=zeros(length(I),1);           %   [Volts], initialize the raw dc voltage
V_ver=zeros(length(I),1);                %    [Volts], initialize the verification terminal
voltage
```

```
Vd_c=zeros(length(I),1);            %   [Volts], initialize the charge diffusion voltage
Vd_d=zeros(length(I),1);                %    [Volts], initialize the discharge diffusion
voltage
Vdc_data=zeros(length(I),1);        %   [Volts], Datasheet Vdc
error=zeros(length(I),1);           %   [Volts], RC estimation residuals
Ahr=zeros(length(I),1);             %   [Amp-Hours], initialize the ahr counter
R0est=zeros(length(I),1);           %   [Ohms], initialize the array for R0 estimation
R1est=zeros(length(I),1);           %   [Ohms], initialize the array for R1 estimation
C1est=zeros(length(I),1);           %   [Farads], initialize the array for C1 estimation

%% Parameter Value Initialization

strt=find(abs(I)>5,1,'first');      %   Start of iteration, current first appears
Vdc(1:strt)=13.1;                   %   [Volts], initial value for open circuit voltage
Vdc_raw(1:strt)=13.1;
b0(1:strt)=R0guess;                 %   [], initial value for b0, by the forward method
b1(1:strt)=-R0guess+(R0guess...
    +R1guess)*T/(R1guess*C1guess);  %   [], initial value for b1
f1(1:strt)=-1+T/(R1guess*C1guess);  %   [], initial value for f1
R1est(1:strt)=R1guess;
R0est(1:strt)=R0guess;
C1est(1:strt)=C1guess;
c=1e-5;                             %   [], updater gain
theta=[b0(1);b1(1);f1(1)];          %   The discrete model parameter array

%% Populate Diffusion Voltage Arrays

for k=2:1:length(I)
        time(k)=time(k-1)+T;        %   populate time array
        Ahr(k)=Ahr(k-1)+I(k)*T/3600;%   Ahr counting
        Vd_c(k)=-Vdc(1)-0.0405...   %   [Volts] Charge Diffusion Voltage, w/o offset
               *log(time(k)+30*60)...
               +13.785;              %    The formula gives Vd_c(time), but the data starts
30 mins after charge
        Vd_d(k)=-1.576e-6*Ahr(k)^4+...
        1.9201e-4*Ahr(k)^3-...      %   [Volts] Discharge Diffusion Voltage
        7.3715e-3*Ahr(k)^2+...
        1.0945e-1*Ahr(k);
        Vdc_data(k)=0.8703*(1-Ahr(k)/55)^3-...% [Volts] datasheet dc voltage
            1.7414*(1-Ahr(k)/55)^2+...
            2.5774*(1-Ahr(k)/55)+...
            11.4;
end
Vdc_data(1)=13.1;
Vd_c(1)=-Vdc(1)-0.0405...           %   [Volts] First ele of Charge Diff, w/o offset.
        *log(30*60)...
        +13.785;
Voffset=(V(1)-Vdc(1))/Vd_c(1);      %   [Volts] Diffusion voltage offset
Vd_c=Vd_c*Voffset;                  %   [Volts] Charge Diffusion Voltage, w/ offset

%% System Identification Iteration

for k=strt:1:length(I)              %   Iteration steps
        c=c/0.99998;                     %    Forgetting factor for increasing estimation
weight at later time
        time(k)=time(k-1)+T;        %   update time array
        Vrc(k)=Vdc(k-1)-V(k)-...    %   obtain "measured" RC voltage with V and Vdc(k-1)
        Vd_d(k)+Vd_c(k);            %   and diffusion voltages
        Vrc_ver_test(k)...             %    Find the RC model voltage given the estimated
parameters.
        =b0(k-1)*I(k)+b1(k-1)*I(k-1)-f1(k-1)*Vrc_ver_test(k-1);
        if I(k)>2                   %   Update based on the magnitude of the command
            phi=[I(k),I(k-1),-Vrc(k-1)];
            Vrc_hat(k)=phi*theta;
            error(k)=Vrc(k)-Vrc_hat(k);
            theta=theta+[c*error(k),0,0;0,c*error(k),0;0,0,c*error(k)]*transpose(phi);
        else
            phi=[I(k),I(k-1),-Vrc(k-1)];
            Vrc_hat(k)=phi*theta;
        end
        b0(k)=theta(1);             %   Update the discrete parameter
```

```
        b1(k)=theta(2);             %   Update the discrete parameter
        f1(k)=theta(3);             %   Update the discrete parameter
        Vdc_raw(k)=...
            Vrc_hat(k)+V(k)+...
            Vd_d(k)-Vd_c(k);        %   Through KVL, the open circuit voltage is updated
        Vdc(k)=Vdc_raw(k)*n_ocv(1)+Vdc_raw(k-1)*n_ocv(2)-Vdc(k-1)*d_ocv(2);
        R0est(k)=b0(k);             %   Estimated R0
        R1est(k)=...                %   Estimated R1
            -(-b1(k)+b0(k)*f1(k))/(f1(k)+1);
        C1est(k)=...                %   Estimated C1
            -T/(-b1(k)+b0(k)*f1(k));
        if R1est(k)>1.1*(R1est(k-1)) || R1est(k)<0.9*R1est(k-1)% Keep the
            R0est(k)=R0est(k-1);    % estimations from previous sample
            R1est(k)=R1est(k-1);    % if the estimation is too far off
            C1est(k)=C1est(k-1);
            b0(k)=b0(k-1);
            b1(k)=b1(k-1);
            f1(k)=f1(k-1);
        end
end
%% Verification

for k=1:1:length(I)
    if k>1
        Vrc_ver(k)...                   %    Find the RC model voltage given the estimated
parameters.
        =b0(k)*I(k)+b1(k)*I(k-1)-f1(k)*Vrc_ver(k-1);
        V_ver(k)=Vdc(k)-Vrc_ver(k)-...
        Vd_d(k)+Vd_c(k);            %   Find the terminal voltage given the estimation
    else
        V_ver(k)=Vdc(k)-Vrc_ver(k)-...
        Vd_d(k)+Vd_c(k);            %   Find the terminal voltage given the estimation
    end
end
AvgError=sqrt(sum((V-V_ver).^2)...
        /length(I))                 %   [volts^2], error voltage square per sample
figure;hold;
plot(time,V,'Color','b','LineWidth',2)
plot(time,V_ver,'Color','g','LineWidth',2)
plot(time,Vdc,'y','LineWidth',2)
plot(time,Vdc_data,'m','LineWidth',2)
legend('Output    Voltage','Model    Tracking    Voltage','Estimated    Effective    Source
Voltage','Datasheet Open Circuit Voltage')
xlabel('time [Seconds]')
ylabel('Voltage [Volts]')
figure;
plot(time,V-V_ver)
xlabel('time [Seconds]')
ylabel('Estimated Voltage Error [Volts]')

%% Ahr vs. b0

for k=1:1:length(I)/100
    AhrSub(k)=Ahr(k*100);
    b0sub(k)=b0(k*100);
end
figure
plot(AhrSub,b0sub)
xlabel('Ahr Discharged [Ahrs]')
ylabel('Estimated R0 [Ohms]')

%% Estimated Parameters

figure
plot(time,R1est)
xlabel('time [Seconds]')
ylabel('Est. R1 [Ohms]')
figure
plot(time,C1est)
xlabel('time [Seconds]')
ylabel('Est. C1 [Farads]')
```

```
%% Maximum Power

figure
plot(time,Vdc.^2./(2.*b0))
```

The auto initial parameter guesses estimation code is presented here.

```
function [R0,R1,C1] = AutoParaInit(I,V,T,range)

%   The function provides an initial estimated battery
%   R-RC impedance structure, given appropirate voltage/current
%   data, sample time, and user defined range of investigation.


strt=find(abs(I)>1,1,'first');          %locate the first sample
                                        %for meaningful current.
End=strt+range;                         %Locate the end of investigation

k=find(abs(I(strt:End))<0.1,1,'last'); %find the voltage average between
                                        %the first and last zero current
Veff=(V(k+strt)+V(strt))/2;             %voltage in the range as Veff
theta=...                               %Discrete Parameters
    Determine(Veff-V, I, strt, End);
R0=theta(2);                            %   Estimated R0
R1=...                                  %   Estimated R1
   -(-theta(3)+theta(2)*theta(1))/(theta(1)+1);
C1=...                                  %   Estimated C1
    -T/(-theta(3)+theta(2)*theta(1));
```